THESIS FOR THE DEGREE OF DOCTOR OF PHILOSOPHY

Leveraging Industrial Side-Streams and Carbonate Chemistry for Sustainable CO_2 Capture

EMMANOUELA LEVENTAKI

Department of Chemistry and Chemical Engineering

CHALMERS UNIVERSITY OF TECHNOLOGY

Gothenburg, Sweden 2026

Leveraging Industrial Side-Streams and Carbonate Chemistry for Sustainable CO_2 Capture

EMMANOUELA LEVENTAKI
ISBN 978-91-8103-422-6

Doktorsavhandlingar vid Chalmers tekniska högskola
Ny serie nr 5879
ISSN 0346-718X
https://doi.org/10.63959/chalmers.dt/xxxx

Department of Chemistry and Chemical Engineering
Chalmers University of Technology
SE-412 96 Gothenburg
Sweden
Telephone + 46 (0)31-772 1000

Cover: Imagining the industrial integration of carbon capture

Printed by Chalmers Digitaltryck

Gothenburg, Sweden 2026

Leveraging Industrial Side-Streams and Carbonate Chemistry for Sustainable CO_2 Capture

EMMANOUELA LEVENTAKI

Department of Chemistry and Chemical Engineering
CHALMERS UNIVERSITY OF TECHNOLOGY

Abstract

As environmental research seeks to accelerate the transition away from fossil-based industries, it is essential to adopt a diverse range of decarbonization strategies. One promising approach for CO_2 capture is the utilization of industrial side streams in inorganic carbonation. Inorganic carbonation is a versatile process involving the reaction of CO_2 with alkali or alkaline earth metal hydroxides, toward the formation of metal carbonates. Thus, alkaline wastes and side streams, found in abundance at industrial sites, could have potential as low-cost CO_2 absorbents. In Sweden, the two major industrial sectors –pulp and paper and metallurgy– both generate substantial amounts of alkaline by-products.

The present work focuses on the investigation of carbon capture via carbonation with 6 different absorbents: black liquor and green liquor dregs (pulp and paper residues), three steel slags (tunnel kiln slag, ladle furnace slag, and electric arc furnace slag), and NaOH-ethanol solutions. Direct aqueous carbonation experiments were conducted with mixtures of 15 or 30% CO_2 balanced with N_2 in the case of the side-stream materials, while the NaOH-ethanol solutions were investigated in direct air capture. Experiments were conducted at ambient pressure and the uptake of CO_2 by each absorbent system was monitored. Key operating parameters, such as reactor configuration, particle size, and temperature were investigated.

Black liquor contains dissolved NaOH, which reacts with CO_2 to form soluble Na_2CO_3 and $NaHCO_3$. Black liquor samples prepared from soda-pulping presented absorption capacity similar to that of a 3 wt% pure NaOH solution. The other materials derive their alkalinity primarily from Ca-based compounds, such as hydroxides and silicates, which react with CO_2 towards the precipitation of $CaCO_3$. The accessibility of Ca-bearing phases and solubility of Ca^{2+} significantly affect the carbonation performance. Thus, reducing particle size by crushing or stirring and decreasing the solid-to-liquid ratio had a positive impact on the yield of carbonation. In the case of NaOH-ethanol solutions their performance in direct air capture is primarily mass-transport controlled. The use of a stirred reactor led to nearly complete removal of the CO_2 in the air passing through the reactor.

Overall, this thesis demonstrates the versatility and simplicity of inorganic carbonation as a carbon capture strategy, highlighting several promising pathways. Further research is required to develop a complete process tailored to each individual system and to enable their successful industrial scale-up.

Keywords: Carbon capture, Inorganic carbonation, Alkaline side-streams

List of Publications

The thesis is based on the following appended papers:

Paper I: In-Line Monitoring of CO_2 Capture with NaOH in a Customized 3D-Printed Reactor without Forced Mixing

Emmanouela Leventaki, Francisco M. Baena Moreno, Gaetano Sardina, Henrik Ström, Ebrahim Ghahramani, Shirin Naserifar, Phuoc Hoang Ho, Aleksandra M. Kozlowski, Diana Bernin

Sustainability, Volume 14, 2022. DOI: 10.3390/su141710795

Paper II: Experimental evaluation of black liquor carbonation for CO_2 capture

Emmanouela Leventaki, Francisco M. Baena Moreno, Joanna Wojtasz Mucha, Niclas Sjöstedt, Abdul Raouf Tajik, Gaetano Sardina, Henrik Ström, Diana Bernin

Journal of CO2 Utilization, Volume 72, 2023. DOI: 10.1016/j.jcou.2023.102516

Paper III: Aqueous mineral carbonation of three different industrial steel slags: Absorption capacities and product characterization

Emmanouela Leventaki, Eduarda Couto Queiroz, Shyam Krishnan Pisharody, Amit Kumar Siva Kumar, Phuoc Hoang Ho, Michael Andersson-Sarning, Björn Haase, Francisco M. Baena-Moreno, Alexandre Cuin, Diana Bernin

Environmental Research, Volume 252, 2024. DOI: 10.1016/j.envres.2024.118903

Paper IV: CO_2 Capture through Aqueous Carbonation Using Green Liquor Dregs as the Absorbent

Eduarda Couto Queiroz, **Emmanouela Leventaki**, Christian Kugge, Diana Bernin

ACS Sustainable Research & Management, Volume 2, 2024. DOI: 10.1021/acssusresmgt.4c00373

Paper V: Factors affecting the carbon capture performance of steel slag and green liquor dregs in direct aqueous carbonation

Eduarda Couto Queiroz, **Emmanouela Leventaki**, Alexandre Cuin, Björn Haase, Christian Kugge, Diana Bernin

(Accepted)

Paper VI: The performance of sodium hydroxide-ethanol solutions in direct air capture

Emmanouela Leventaki, Francisco M. Baena Moreno, Diana Bernin

(Manuscript)

Publications not included in this thesis:

Paper VII: Effluents and residues from industrial sites for CO2 capture: a review

Francisco M. Baena Moreno, **Emmanouela Leventaki**, Alexander Riddell, Joanna Wojtasz Mucha, Diana Bernin

Environmental Chemistry Letters, Volume 21, 2023. DOI: 10.1007/s10311-022-01513-x

Paper VIII: Potential of organic carbonates production for efficient CO_2 capture, transport and storage: Reaction performance with NaOH-ethanol mixtures

Francisco M. Baena Moreno, **Emmanouela Leventaki**, Phuoc Hoang Ho, Abdul Raouf Tajik, Danica Brzic, Gaetano Sardina, Henrik Strom, Diana Bernin

Heliyon, Volume 9, 2023. DOI: 10.1016/j.heliyon.2023.e14140

Paper IX: The influence of the impeller on carbonation performances in carbon capture using industrial by-products.

Abdul Raouf Tajik, **Emmanouela Leventaki**, Francisco M. Baena Moreno, Christian Kugge, Diana Bernin, Henrik Strom, Gaetano Sardina

International Journal of Thermofluids, Volume 29, 2025. DOI: 10.1016/j.ijft.2025.101385

Paper X: Green liquor dregs for carbon capture, utilization, and storage: initial LCA and economic analysis

Gulnara Shavalieva, Harald Olivegren, Henrikke Baumann, **Emmanouela Leventaki**, Eduarda Couto Queiroz, Diana Bernin

Nordic Pulp & Paper Research Journal, Volume 41, 2026. DOI: 10.1515/npprj-2024-0013

Paper XI: **Solid-Liquid Phase Transitions of Triglycerides in Griebenschmalz, Smalec, and Fedt Studied Using 13C Solid-State NMR with Dynamics-Based Spectral Filtering**

Diana Bernin, **Emmanouela Leventaki**, Daniel Topgaard

Applied Magnetic Resonance, Volume 54, 2023. DOI: 10.1007/s00723-023-01564-5

Contribution Report

The author of this thesis has made the following contributions to the appended papers:

Paper I (First author): I designed and 3D printed the reactor. I planned and performed all experiments of carbon capture together with Francisco M. Baena Moreno, while physicochemical analysis and CFD simulations were conducted by co-authors. I visualized and interpreted the data. I wrote the manuscript. I reviewed and edited the article along with the co-authors.

Paper II (First author): I planned and performed all experiments. I conducted the X-Ray diffraction analysis. I took scanning electron microscopy images together with Francisco M. Baena Moreno. Nuclear magnetic resonance analysis and computational fluid dynamics simulations were performed by co-authors. I wrote the manuscript. I reviewed and edited the article along with the co-authors.

Paper III (First author): I set up the experimental methodology, planned and performed experiments of carbon capture together with Eduarda Couto Queiroz, Shyam Krishnan Pisharody and Amit Kumar Siva. I conducted scanning electron microscopy with Energy-dispersive X-ray spectroscopy for identifications of the elements on the steel slag particles. I also did X-Ray diffraction analysis for identification of the crystal phases present before and after carbonation. I wrote the manuscript and edited it together with the co-authors. Fourier-transform infrared spectra acquisition and Rietveld analysis on the X-Ray diffractograms were carried out by co-authors.

Paper IV (Co-author): I planned and performed experiments of carbon capture in collaboration with Eduarda Couto Queiroz. We performed scanning electron microscopy with Energy-dispersive X-ray spectroscopy for identification of the elements on the green liquor dregs particles, and X-Ray diffraction analysis to identify the crystal phases. I helped with data interpretation, concept visualization and editing of the manuscript.

Paper V (Co-author): I planned and performed experiments and interpreted the results in collaboration with Eduarda Couto Queiroz. We performed scanning electron microscopy with Energy-dispersive X-ray spectroscopy for identification of the elements on the particles, and X-Ray diffraction analysis to identify the crystal phases. I carried out physisorption analysis for information on the surface of the particles. I wrote the manuscript, based on Eduarda Couto Queiroz's report. I presented physisorption data and formatted graphs. I conducted TGA, sieve analysis, statistical data treatment and text editing for the first revision of the submitted manuscript.

Paper VI (First author): I set up the experimental methodology, carried out experiments and physicochemical analysis. Diana Bernin carried out nuclear magnetic resonance measurements. I plotted and interpreted the results. I wrote the manuscript.

Acknowledgements

This work is funded by the Swedish Energy Agency and samples used for the experiments were provided by SCA and Höganäs. I would like to thank Christian Kugge and Björn Haase for providing samples and helpful input throughout the project. I am thankful to my colleagues at the Decrease project for their passion and ideas and for always striving to advance our research. Raouf Tajik and Gulnara Shavalieva are both motivated and knowledgeable researchers who taught me a lot and made a significant contribution to the project. The Chalmers Materials Analysis Laboratory (CMAL) is acknowledged for the SEM images and XRD diffractograms.

I would like to express my gratitude to my two supervisors, Diana Bernin and Francisco Baena-Moreno for their guidance and support throughout the past 5 years. Their extensive knowledge, insightful ideas, and constant encouragement have contributed greatly to my learning and development. Working under their supervision brough new enjoyable challenges and they were always ready to provide support whenever I needed it. I hope they can take pride in my development as a researcher.

I would also like to acknowledge Hugo Boccara and Oliver Nelis, who took an idea from the lab and are working tirelessly to bring it to life. Thanks to their dedication and belief in our team the company Korall was created, and we are presented with the chance to develop a large-scale climate solution. Being part of this enterprise is a great honor and an invaluable opportunity to experience the first steps of a new-found company into the industrial worlds. They have taught me a lot and I am eager to learn more as the company grows.

I am deeply grateful to all the friends I have made along the way, who helped me in more ways than they know. From brief lunchroom chats, to elaborate personal discussions at 18.30 on a Friday, all the connections I have made contributed to an amazing experience. Having moved around different divisions at the Chemistry department I got to know many amazing people, and I wish that they all know how special they are to me. My group and unit, including Leandro Cid Gomes, Jenny Bengtsson, Moa Larsson, Nicole Abdou, Smaragda Argyri and many other colleagues and friends contributed to an environment of constant learning, mutual respect, and collaboration, where it always felt safe to voice questions and ideas.

Rawipa Intakul was a great partner in teaching and despite the intensity of the course sessions it was very enjoyable working alongside her. Eduarda Couto Queiroz cared about this project as much as I did and I am happy to have gotten the chance to work with her and, in the process, make an amazing friend. I am also thankful to all the master students that I worked with for the chance to discover things alongside them and for getting the opportunity to learn from them. And I could not omit Michael Andersson-Sarning, Patrik Skansen, Andreas Schaeffer and Romain Bordes who have never failed to help me with both ideas and useful hardware.

A very special thank you goes to Lucas Kurth-Azambuja for his remarkable ability to brighten even the gloomiest of days. He was a wonderful office mate for a few months and an even better lifelong friend. Joanna Wojtasz, Feryal Guerroudj, Hanna Tiernan, and Lidya Görür are incredible friends whom I can always trust to stand by my side through both difficult and joyful times. I could not have asked for more amazing people

to share this journey with. Having friends like these can really make a new place feel like home.

I am especially thankful to my partner, Eric, who has changed my life in all the best ways. I feel incredibly fortunate to have someone as kind, loving, curious, and passionate by my side. His love and encouragement have been an immense source of support throughout the past year and made my life fuller than I knew it could be. Everything we take on together, from an evening of cooking and discussing to embarking on a new adventure, feels like an opportunity to learn and grow side by side. I wish for him to achieve everything he dreams of, and I will always do my best to support him in making that happen.

Lastly, my deepest gratitude goes to my family. My dad guided me toward science and has always been there for me. His belief in me and his encouragement in the right directions are what brought me here. My mom and sister have supported and loved me more than I could ever ask for. I am deeply grateful to my entire family. They are remarkable people, full of love and energy, and I aspire to be like them. They have shaped me into a person who pursues and achieves her dreams. Their sacrifices and efforts in raising me have brought me this far, and I can only hope to make them.

Table of contents

Chapter 1: Introduction

Background

Global industrialization has led to significant environmental and climatological changes, the impacts of which are becoming increasingly evident. Anthropogenic emissions of greenhouse gases (GHGs), including CO_2, CH_4 and NO_x, have driven a global mean temperature increase of approximately 1.22 °C over the past decade (2015–2024) relative to pre-industrial levels [1]. Among these GHGs, the dominant contributor from human activities is CO_2 with total energy-related emissions of 37.8 Gt in 2024, as reported in the 2025 Global Energy Review of the International Energy Agency (IEA) [2]. The 2024 atmospheric CO_2 concentration of 422.5 ppm was the highest recorded to date. The escalating climate impact of anthropogenic GHGs emissions coupled with the population growth and industrial expansion induce an incentive to mitigate human-related GHGs. The Intergovernmental Panel on Climate Change (IPCC) has established a limit of 2 °C of warming in the near term (2021-2040), based on which the Paris Agreement of 2016 was signed [3]. The IPCC has laid out different shared socioeconomic pathways (SSP) based on the rate of emissions in the upcoming years in assessment reports (AR). The latest report (AR 6) disclosed that an overshoot above 2 °C is likely in most SSPs [4]. Thus, there is a pressing necessity for industrial decarbonization, which can only be achieved by co-deployment of different strategies, such as transition to renewable energy (solar, hydropower, wind, biomass, etc.) and electrification of energy-intensive sectors [5,6]. Among these strategies is carbon capture, utilization, and storage (CCUS). CCUS can facilitate CO_2 removal during the energy transition, mitigate the emissions of other sectors, such as cement production, and address the excess CO_2 concentration in the case of a temperature overshoot [6,7]. Figure 1.1 illustrates a generalized scheme of the different pathways of CCUS. There are multiple routes depending on the targeted source of CO_2, capture technology and final application.

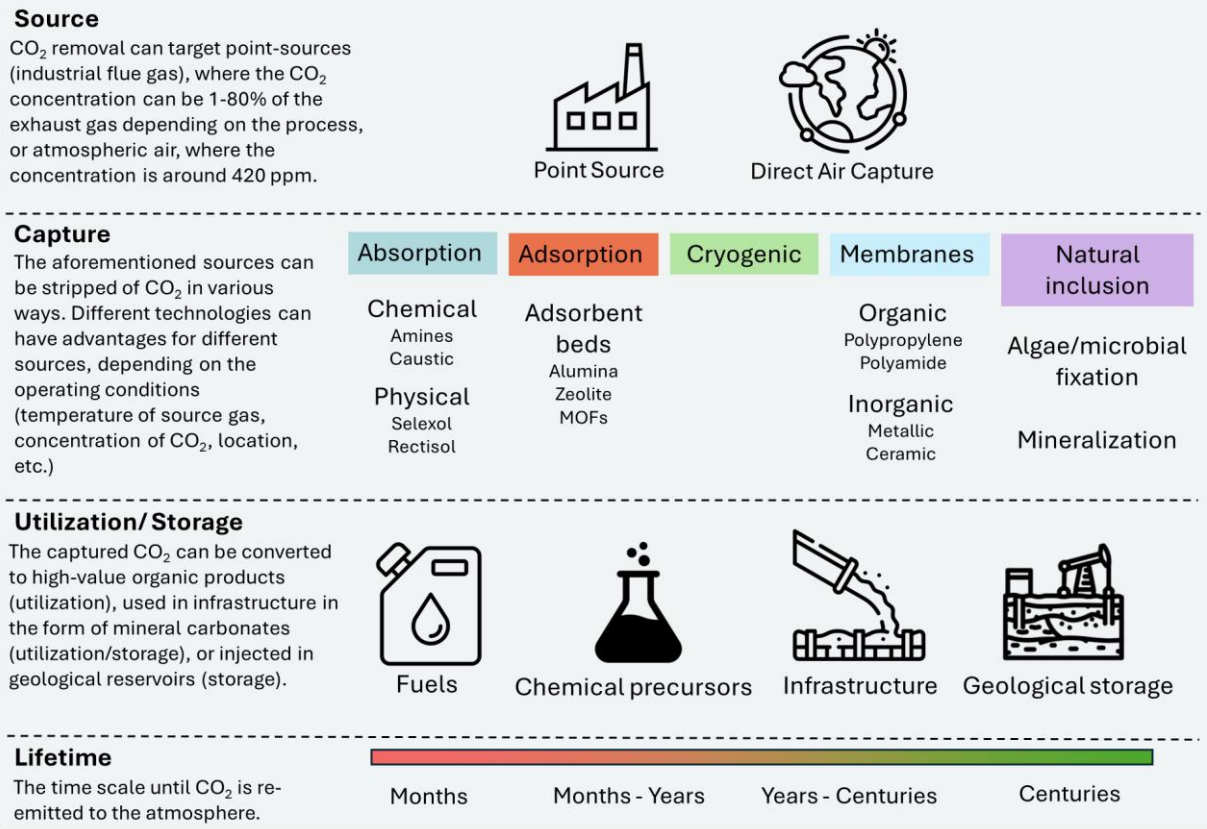

Figure 1.1. *Overall scheme of CCUS adapted from [8–10].*

Carbon capture by source of CO_2

The source of CO_2 can be industrial flue gas from power plants, or heavy industries where CO_2 is inherently generated in a process (e.g. cement kiln). The three major technologies for flue gas CC are post-combustion, pre-combustion and oxy-fuel combustion CC [9,10]. Post-combustion CC refers to the removal of CO_2 from the flue gas generated from combustion of fuel, where its concentration is 12-15%. This is a straightforward approach primarily addressed with chemical absorbents. Pre-combustion CC entails the conversion of hydrocarbon feedstock to synthesis gas by gasification and subsequent removal of CO_2. The gasification converts fuel into a mixture of H_2 and CO and the CO is then converted to CO_2 through the water-gas shift with the additional generation of H_2. The concentrated CO_2 (80-90%) can then be removed more efficiently than in post-combustion CC. In oxy-fuel combustion, fuel is burned in pure oxygen. The produced exhaust consists of CO_2 (90-95%) and water vapor, which facilitates the separation of CO_2. The bottleneck of this process is the high energy associated with generating pure O_2. The fuel in these technologies can be either fossil based, or biobased, which opens the possibility for negative emissions. Apart from power plants, there are other industrial processes which involve an inherent release of CO_2, such as aluminum production (1-2% CO_2), steel manufacture (20-27% CO_2 in the blast furnace exhaust) and cement production (14-33% CO_2) [11].

Alternatively to point-sources, CO_2 can also be captured from the air in a process called direct air capture (DAC) [12]. This option is the most thermodynamically unfavorable owing to the low concentration of CO_2 in air (0.04%). However, it is widely investigated as a pathway towards achieving negative emissions and to tackle the possibility of a temperature overshoot in the future.

Carbon capture by technology

The capture of CO_2 can be performed in various ways. The main CC systems are highlighted in Figure 1.1, while many more exist at various technology-readiness levels (TRL). Wu et al. conducted a comprehensive review of all carbon capture technologies [11]. This work concluded that the primary technologies for post-combustion CC are absorption, adsorption and membrane separation. Chemical absorption and especially amine-based solutions hold the lead in TRL for post-combustion CC. The main types of technologies will be briefly discussed here.

Absorption is the process in which CO_2 is selectively transferred into a solid or most commonly liquid phase, by chemical (chemisorption) or physical (physisorption) mechanisms. Notable chemical absorbents for CO_2 are amines, such as monoethanolamine (MEA), metal hydroxides and carbonates, ionic liquids, and ammonia. There are three physisorption processes used in large-scale applications. The rectisol process utilizes methanol, selexol utilizes polyethyleneglycol dimethylether and purisol utilizes n-methyl-2-pyrrolidone [13]. All three processes operate at low temperatures and high pressure for absorption in the solvent. In adsorption, the CO_2 attaches on a solid surface, rather than transferring into the bulk phase. Depending on the type of interactions this can again be a chemical or physical process. In chemical adsorption, solid porous materials can be functionalized with amine groups, or metal hydroxides. Examples of physical adsorbents are zeolites and carbon-based materials [13]. Cryogenic CC involves cooling a gas mixture at a temperature at which CO_2 can be selectively separated by sublimation [14]. Membrane CC is a size-selective technology. The types of membranes are polymeric, ceramic and hybrid, and these can be configured to maximize the permeability of CO_2 through the pores. Lastly, natural inclusion refers to processes that take place in the carbon cycle, such as photosynthesis and mineralization. Natural carbon sinks can be enhanced by technological means to accelerate the CO_2 uptake and harvest valuable products. Biofixation of CO_2 with microalgae and other microorganisms is explored for the production of value-added chemicals such as biofuel [15]. Mineralization is the natural weathering of ores such as serpentine and wollastonite. The alkaline earth metal oxides in these minerals can react with CO_2 to form stable metal carbonates [16]. Natural weathering is a very slow process, but alkali and alkaline earth metal oxides and hydroxides are abundant in industrial side streams. Thus, ex-situ mineralization is a topic of increasing interest and will be discussed in detail in the next chapters.

Carbonation of industrial side streams

Industrial alkaline side streams are residual streams from industrial processes with a high content of alkali and/or alkaline earth metal hydroxides (or silicates). These materials have received increasing interest over the past years for their potential to sequester CO_2 [17]. They present a largely unexploited feedstock of CO_2 sorbent chemicals, which are mostly landfilled, incinerated, and more rarely recycled or utilized in other applications [16]. Additionally, they are generally inexpensive and are commonly generated near industrial flue gas streams, which offers a logistic advantage. Such side streams are cement waste, construction and demolition debris, steel slags, coal ash, biomass ash, municipal solid waste incinerator (MSWI) ash, alkaline paper mill side streams and mine tailings [18]. The main alkali and alkaline earth metals commonly found in these are Na, K, Ca and Mg, while others like Cs, Li and Ba can only be found in trace concentrations [19,20]. Alkali metals react with CO_2 forming water soluble carbonate and bicarbonate species, while the divalent alkaline earth metals form stable carbonates which are insoluble or sparingly soluble in water [19].

Chemical reactions of inorganic carbonation

CO_2 is considered a Lewis acid and when dissolved in water it forms carbonic acid (H_2CO_3). Across the basic range of pH H_2CO_3 dissociates to bicarbonate and carbonate ions [21]. The absorption of CO_2 from the gaseous to the aqueous phase, followed by its dissociation, are expressed in equations (1.1) and (1.2).

$$CO_{2(g)} \leftrightarrow CO_{2(aq)} \tag{1.1}$$

$$CO_{2(aq)} + H_2O \leftrightarrow H_2CO_{3(aq)} \leftrightarrow HCO^-_{3(aq)} + H^+_{(aq)} \leftrightarrow CO^{2-}_{3(aq)} + 2H^+_{(aq)} \tag{1.2}$$

At pH>10.5 the equilibrium is shifted towards CO_3^{2-}, at 6.5<pH<10.5, HCO_3^- is predominant, while the main species below 6.5 is H_2CO_3.

When an alkali metal hydroxide is present it reacts with CO_2 according to the equations (1.3 – 1.6) [22]. Firstly, the metal hydroxide dissociates to the metal cation and hydroxide ion. At high concentration of hydroxide, equation (1.2) shifts to the right and metal carbonate is the main species, while as the hydroxide ions are consumed and the pH is lowered the equilibrium shifts towards the metal bicarbonate. Alkali metal hydroxides and carbonate/bicarbonate species are readily soluble in water [23]. In the following equations M denotes Na or K.

$$MOH_{(s)} \leftrightarrow MOH_{(aq)} \leftrightarrow M^+_{(aq)} + OH^-_{(aq)} \tag{1.3}$$

$$2M^{+}_{(aq)} + CO^{2-}_{3(aq)} \leftrightarrow M_2CO_{3(aq)} \quad (1.4)$$

$$M^{+}_{(aq)} + HCO^{-}_{3(aq)} \leftrightarrow MHCO_{3(aq)} \quad (1.5)$$

$$M_2CO_{3(aq)} + H_2CO_{3(aq)} \leftrightarrow 2MHCO_{3(aq)} \quad (1.6)$$

When an alkaline earth metal hydroxide is present the carbonation follows the path shown in equations (1.7) and (1.8) [24]. Here M denotes Ca or Mg.

$$M(OH)_{2(s)} \leftrightarrow M(OH)_{2(aq)} \leftrightarrow M^{2+}_{(aq)} + 2OH^{-}_{(aq)} \quad (1.7)$$

$$M^{2+}_{(aq)} + CO^{2-}_{3(aq)} \leftrightarrow MCO_{3(s)} \quad (1.8)$$

Alkaline earth metal hydroxides have very limited water solubility, thus equation (1.7) reaches equilibrium when the saturation concentration is reached. The corresponding metal carbonates are even less soluble, and they precipitate out upon formation. Thus, if there is excess of the $M(OH)_2$ the precipitation of MCO_3 drives equation (1.7) to the right. As the pH decreases the solubility of the metal carbonate increases slightly. Additionally, any dissociated MCO_3 can further react with carbonic acid to form the respective metal bicarbonate which is more soluble in water [equation (1.9)].

$$M_2CO_{3(aq)} + H_2CO_{3(aq)} \leftrightarrow M(HCO_3)_{2(aq)} \quad (1.9)$$

In many industrial side streams, as well as in natural geological formations, alkaline earth metals exist in silicate phases. Equation (1.10) represents the carbonation reaction of metal silicates [25]. The metal carbonates are energetically favored over the silicate phases, but carbonation is limited by the insignificant solubility of metal silicates in water. Thus, accelerating the carbonation process while maintaining minimum consumption of energy and raw materials is key to harvesting the CO_2 sequestration potential of industrial side streams [19].

$$M_xSi_yO_{x+2y+z}H_{2z} + xCO_2 \rightarrow xMCO_3 + ySiO_2 + zH_2O \quad (1.10)$$

The solubility constants of Ca and Mg hydroxides and carbonates at 25 °C and the molar solubility of their corresponding metal ions (Ca^{2+} and Mg^{2+}) are reported in Table 1.1. In addition, three Ca phases that can be found in steel slags are included, though Ca and Mg can be found in various other crystalline or amorphous phases with different solubilities in alkaline side streams [25].

Table 1.1. *Solubility product constant (Ksp) and molar solubility at 25 °C of $Ca(OH)_2$, $Mg(OH)_2$, their corresponding carbonates and three Ca phases that can be found in industrial alkaline waste such as steel slags and cement waste [26–28]. The last three dissolution reactions are balanced with H_2O.*

Phase	Dissolution reaction	K_{sp}	Solubility (M)
Portlandite	$Ca(OH)_2 \rightarrow Ca^{2+} + 2OH^-$	$5.0 \cdot 10^{-6}$	$1.1 \cdot 10^{-2}$
Brucite	$Mg(OH)_2 \rightarrow Mg^{2+} + 2OH^-$	$5.6 \cdot 10^{-12}$	$1.1 \cdot 10^{-4}$
Calcite	$CaCO_3 \rightarrow Ca^{2+} + CO_3^{2-}$	$3.4 \cdot 10^{-9}$	$5.8 \cdot 10^{-5}$
Magnesite	$MgCO_3 \rightarrow Mg^{2+} + CO_3^{2-}$	$6.8 \cdot 10^{-6}$	$2.6 \cdot 10^{-3}$
C_2S (dicalcium silicate)	$Ca_2SiO_4 \rightarrow 2Ca^{2+} + H_4SiO_4 + 4OH^-$	$4.3 \cdot 10^{-18}$	$5.4 \cdot 10^{-4}$
C_3S (tricalcium silicate)	$Ca_3SiO_5 \rightarrow 3Ca^{2+} + H_4SiO_4 + 6OH^-$	$9.6 \cdot 10^{-23}$	$3.6 \cdot 10^{-3}$
C_3A (tricalcium aluminate)	$3CaO \cdot Al_2O_3 \rightarrow 3Ca^{2+} + 2AlO_2^- + 4OH^-$	$1.4 \cdot 10^{-21*}$	$6.3 \cdot 10^{-3}$

* Value reported at 20 °C [28].

Pathways of ex-situ mineral carbonation

As previously mentioned, mineral carbonation can occur via the natural weathering of metal-oxide-bearing rocks, or by ex-situ reaction of CO_2 with minerals and industrial wastes. Ex-situ carbonation is accelerated by controlling factors such as humidity, temperature and pressure to enhance the reaction rate. Accelerated carbonation can be divided into three routes: direct gas-solid, direct aqueous and indirect aqueous carbonation, as displayed in Figure 1.2. Direct gas-solid (or direct dry) carbonation is the most straightforward route. Due to the slow reaction kinetics, it requires elevated temperature, high partial pressure of CO_2 and very fine particle size to yield an adequate carbonation efficiency. Thus, it is associated with high energy demands. This process has potential to be used for the carbonation of side-streams with high content of free Ca and Mg oxides and hydroxides, as they react with CO_2 more readily under sufficient humidity and the energy generated during the exothermic carbonation reaction can be harvested. However, this method is unfeasible when it comes to Ca and Mg in silicate phases. Furthermore, it requires the gaseous feed to contain pure CO_2, as the partial pressure greatly affects the efficiency of the process [19,29,30]. Direct aqueous (or direct wet) carbonation involves the reaction of CO_2 with the alkaline material in an aqueous suspension (slurry). In this process, Ca and Mg ions from oxide, hydroxide and silicate phases can leach into the water and react with the dissolved CO_2 according to the reactions discussed in the previous section. Introducing an aqueous phase allows carbonation to take place between the dissociated ions of the reactants, thus increasing the yield, without the need for intensive operating conditions. This method is considered very promising because it can achieve high carbonation efficiencies under mild conditions [31]. Indirect aqueous carbonation is a two-step process involving the extraction of alkaline earth metals in the first step and their

aqueous carbonation in the second. The extraction step entails treating the solids with an additive such as an acid, salt or alkali. In acid extraction, a weak (acetic acid, valeric acid) or strong (HCl, HNO_3 and H_2SO_4) acid is added to dissolve the metal ions. Strong acids are very effective in this, but as basicity favors carbonation, the acidic extraction is followed by an increase of pH to perform the carbonation step. Therefore, this process is known as pH swing. Ammonium salts, such as NH_4Cl and CH_3COONH_4 can also effectively enhance the leaching of Ca^{2+} and Mg^{2+} from mineral phases. Caustic soda has also been proposed as an additive to extract metal hydroxide from aluminosilicate phases. This method has been explored very little [19]. The advantage of indirect carbonation is that the end products are pure $CaCO_3$ and $MgCO_3$, which find many commercial applications [32,33]. Its key drawback is the added technoeconomic cost associated with the introduction of raw materials and additional steps for metal extraction, solvent regeneration, etc.

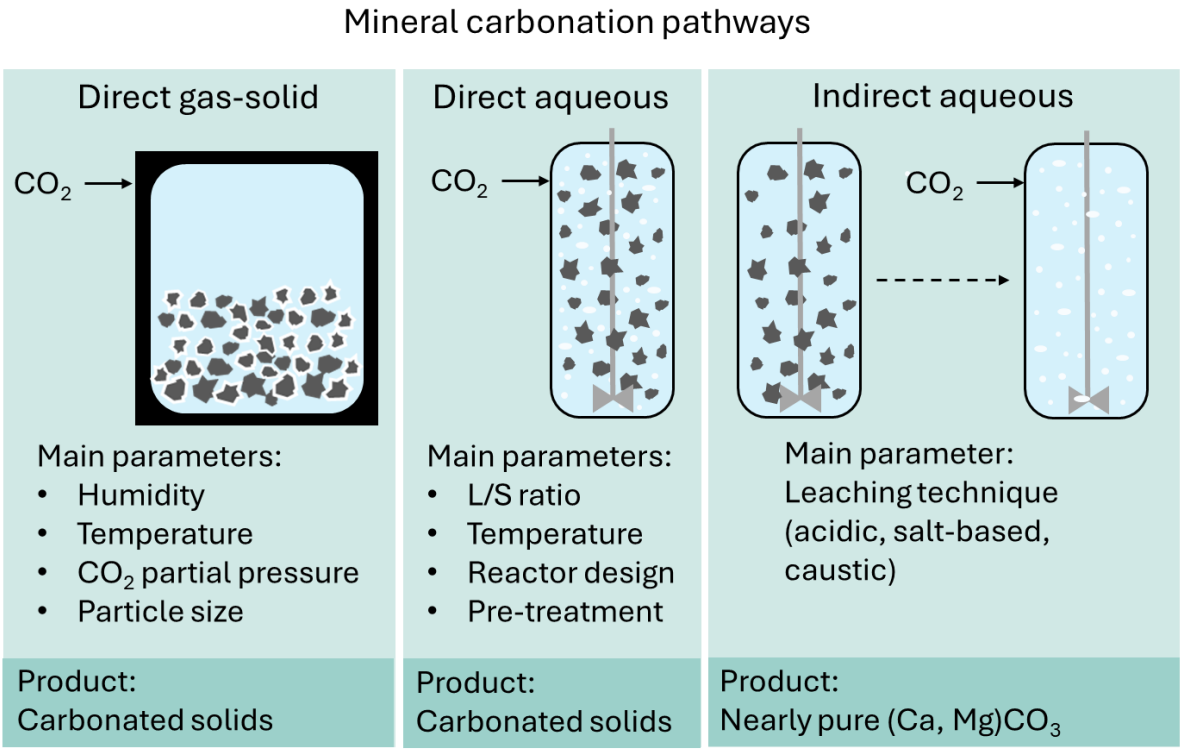

Figure 1.2. *The three mineral carbonation pathways (direct gas-solid, direct aqueous and indirect aqueous carbonation), their main parameters and obtained products. Modified after [19,34,35].*

Alkaline industrial side-streams

In **Paper VII** we conducted a literature review of industrial alkaline side streams and their potential for CO_2 removal [36]. The materials that were investigated in this study, will be discussed in detail below.

Steel slags

The steel industry produces various types of slags from different segments of the process. The steelmaking process is illustrated in Figure 1.3. Lime is added to react with the impurities in the iron, forming molten slag which is separated at each step. The four slags produced are Blast Furnace slag (BF), Basic Oxygen Furnace slag (BOF), Electric Arc Furnace slag (EAF) and Ladle Furnace slag (LF). It is estimated that 0.13 – 0.2 tons of steel slag is generated per ton of steel produced [37]. In 2023 the U.S. geological survey reported the global steel slag production to be between 190 to 290 million tons and the iron slag between 330 and 390 million tons [38]. Iron and steel slags can find application in concrete as aggregates or supplementary cementitious materials, in road construction and in soil stabilization [37,39]. The high content in Ca and Mg oxides and silicates coupled with their high global production render them very promising materials for CO_2 mineralization. Therefore, there is a lot of research focused on this topic. Steel slag carbonation has been reported to yield a CO_2 uptake in the range of 10 – 50 g of CO_2 / kg of slag with the direct gas-solid method, 200-300 g of CO_2 / kg of slag with the direct aqueous method and 100 – 250 g of CO_2 / kg of slag with indirect carbonation [40]. Key parameters affecting the carbonation efficiency are particle size, temperature, CO_2 concentration, solid-to-liquid ratio (S/L, g / L), carbonation time and additives [41]. It is generally agreed that lower particle size enhances carbonation, as it increases the accessibility of the Ca and Mg [42]. The duration of carbonation varies depending on the type of slag and carbonation route. But throughout the literature of accelerated carbonation the process showcases a similar behavior of an initial fast carbonation rate when Ca and Mg are readily available, and a subsequent slow regime where the reaction is limited by the availability of Ca and Mg. The other parameters are subject of optimization. Temperature has a positive effect on the dissolution of silicate phases [43,44], but a negative effect on the dissolution of CO_2 [41] and $Ca(OH)_2$ [24] in water. Thus, the effect of temperature can vary for different types of slag and process conditions. The S/L ratio has a positive effect on the leaching of Ca^{2+} and Mg^{2+}, but it hinders the mass transport of CO_2 from the gaseous to the liquid phase [40]. Despite the extensive body of research on the carbonation of steelmaking slags, industrial implementation remains challenging. According to Zhao et al., these challenges arise from (i) variability in slag composition depending on its origin, (ii) limitations in reaction kinetics, and (iii) high energy demand and associated economic costs [45].

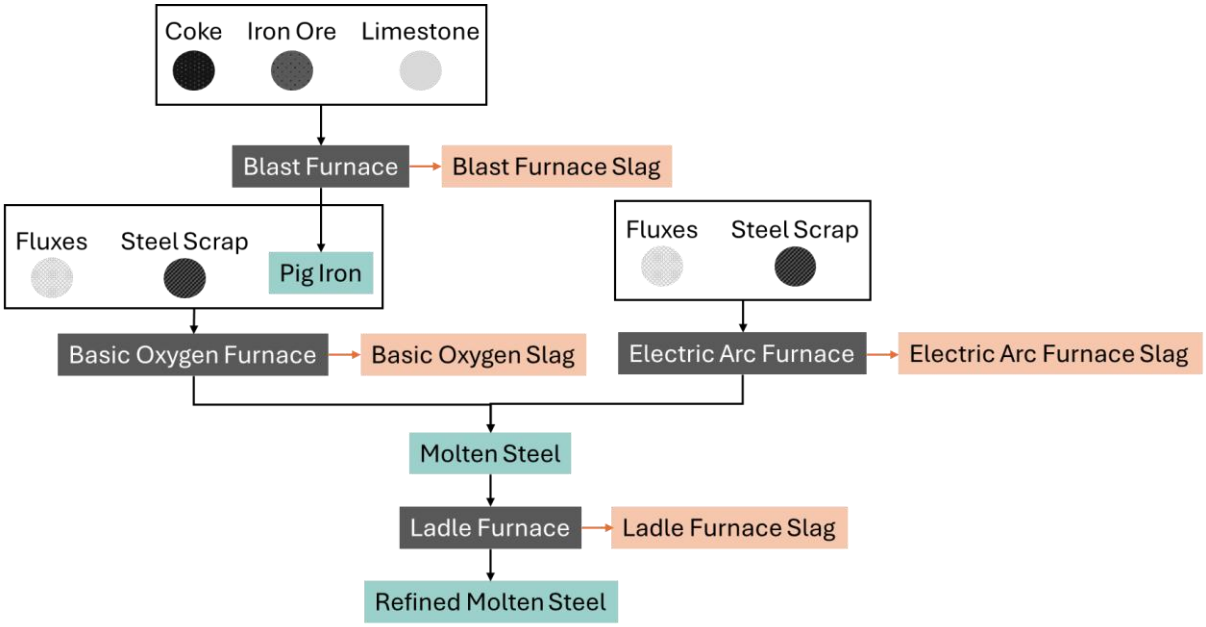

Figure 1.3. *Scheme of the conventional steelmaking process. Modified after [37,46].*

Pulp and paper side-streams

The pulp and paper industry generates alkaline side streams with high content of Ca and Na. An overview of the Kraft pulping process with focus on the generation of side streams is illustrated in Figure 1.4. Kraft cooking is the most wide-spread and established process for pulp production [47]. It entails a chemical treatment of wood chips with an aqueous solution of NaOH and Na_2S, called white liquor. This treatment separates the cellulose fibers from lignin and other organic compounds. The spent liquor from this, called black liquor is an alkaline solution of dissolved and modified lignin and hemicelluloses [48]. The black liquor is condensed and burned in a recovery boiler to generate energy and recover the cooking chemicals. In the chemical recovery cycle, the smelt produced in the recovery boiler is washed and the liquid with dissolved chemicals (green liquor) is treated with $Ca(OH)_2$ to precipitate $CaCO_3$ and recover NaOH. The recovered white liquor is used again in pulping, while the $CaCO_3$ is calcined to regenerate $Ca(OH)_2$ with the emission of CO_2. The alkaline side-streams of this process are black liquor, green liquor dregs (GLD), lime mud, slacker grids and fly ash.

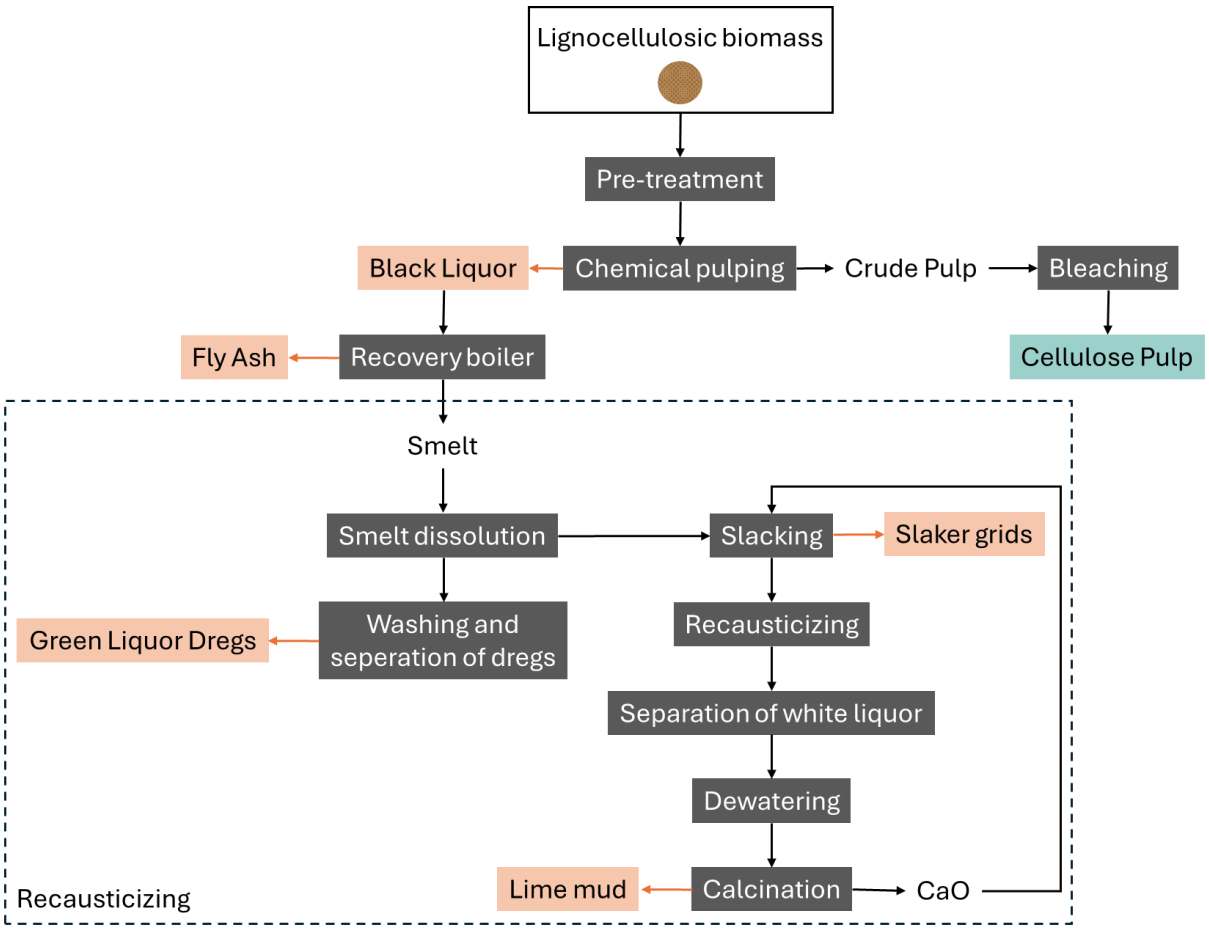

Figure 1.4. *Scheme of the Kraft process and recovery of raw chemicals. Modified after [49].*

Black liquor

Owing to its high pH (12-14), black liquor has the capacity to absorb CO_2. However, the addition of CO_2 in black liquor has only been explored in the frame of black liquor acidification to precipitate and recover lignin [50,51]. Cramstedt investigated the integration of carbon capture to a Kraft mill with the use of white liquor as a CO_2 absorbent coupled with an electric lime kiln to recover CaO and pure CO_2 [52]. In this work it was noted that the increased load to the lime kiln and release of H_2S are important bottlenecks to the implementation of this process. Another chemical treatment for pulping is soda pulping, where the white liquor is aqueous NaOH [47]. This softer process is favorable for the extraction of cellulose from non-woody biomass, which has lower pulping resistance than wood. Agricultural waste, such as wheat straw and oat husks are gaining interest as a source of cellulosic pulp and lignin by soda pulping and acidification of the black liquor [53,54]. Non-woody biomass has a higher silica content than wood, which poses difficulty to the chemical recovery and black liquor combustion. Additionally, silica in non-woody biomass is gaining interest for its potential valorization in alkali-activated concrete, where Portland cement is partially or fully replaced by waste streams such as fly ash, which are activated using waterglass

to form a hardened network [55]. Thus, silica sourced from non-woody biomass could become an increasingly valuable resource as the construction sector shifts toward cement alternatives. In black liquor, silica is dissolved in the form of Na_2SiO_3 [56]. Desilication can be achieved by lowering the pH to 8 which induces the precipitation of amorphous silica [57]. Thus, integration of post-combustion flue gas to capture CO_2 with soda pulping black liquor could be a method to separate silica. The remaining black liquor could be acidified further with recovery of CO_2 and lignin.

Recausticizing residues

The primary inorganic residues from the recausticizing process are green liquor dregs (GLD), slaker grits and lime mud (see Figure 1.4). GLD is the insoluble portion that remains after the smelt dissolution. Slaker grits form in the bottom of the lime slaker, and lime mud is a residue from the lime kiln. All three materials are alkaline owing to CaO. Pérez-López et al. investigated the direct aqueous carbonation of lime mud under varying conditions of temperature and pressure (30 – 60 °C and 10 – 40 bar) and reported a maximum sequestration capacity of 218 kg of CO_2 / ton of material [58]. Slaker grids have also been explored for indirect aqueous carbonation reaching a maximum sequestration capacity of 460 kg CO_2/ton of grits [59]. Paper mill waste has also been proposed for CC via calcium looping, a process consisting of continuous carbonation-calcination cycles [60,61]. The carbonation takes place at high temperatures (650 – 700 °C), followed by calcination under oxy-fuel combustion to generate pure CO_2. Apart from this limited collection of studies, paper mill recausticizing residues have not been researched further in CC. Other promising applications of these waste products are the neutralization of acid mine drainage and the synthesis of geopolymer mortars [62–64].

Other side streams

Construction and demolition waste is a significant potential source of Ca, mainly in the phases of calcium silicate hydrates (C-S-H) and portlandite-for CO_2 sequestration. Construction and demolition wastes are highly heterogeneous and can contain various materials, like crushed concrete, asphalt, glass, mixed demolition debris and other [65]. They are generated in large quantities worldwide, but their high porosity hinders their recyclability. Research on accelerated carbonation indicates that controlled carbonation promotes the formation of small crystals which fill the pores of the materials, improving its durability and promoting reuse as fillers and aggregates [66–68]. The direct aqueous route has gained interest, owing to the much higher carbonation yields that can be achieved in a fraction of the time required for dry carbonation [69,70]. However, its high demand in energy and water hinders it from

industrial implementation, while the direct dry route is more feasible at large scale, as is a simple and industrially mature approach. Another alkaline residue in the construction sector is cement kiln dust (CKD). CKD is a fine powder generated in a rotary kiln where limestone, silica, alumina and iron are mixed and heated together to produce cement clinker [71]. The calcination of limestone is an integral part of the cement manufacturing process. Thus, cement is a high emissions sector, with 900 kg of CO_2 released for every ton of cement produced [72], of which some is regained by carbonation that occurs during the aging of concrete [73,74]. CKD has a very high content in CaO (37 – 77%) and thus has attracted interest in accelerated carbonation [75–78]. Municipal waste incineration ashes are another example of alkaline waste that are explored for potential pathways of valorization. Two main fractions of ashes are produced during the incineration process, bottom and fly ashes. Bottom ash consists of incombustible material such as ceramic, glass, and concrete and it accounts for about 80% of the total ash byproduct, while the remaining 20% is fly ash [79]. Both materials have a high content of Ca and Si compounds, as well as Al, Fe, Na and K in smaller concentrations [80,81]. Bottom ash often finds application as an aggregate for road filling and construction materials, but fly ash is classified as a hazardous waste due to its content in toxic compounds, such as heavy metals (As, Cd, Cu, Cr, Pb, etc.) and dioxins [81,82]. Accelerated carbonation of the ashes has been proposed as a method to immobilize heavy metals and enhance their mechanical properties for utilization in construction materials [82,83]. Um et al. performed carbonation in two different ways, aqueous, with an S/L ratio of 100 and wet, with 0.3 L of water / kg of slag (or 3,333.3 S/L ratio) [84]. The results suggested that aqueous carbonation sequestered more CO_2, but wet carbonation led to the formation of a carbonated layer which effectively hindered the leaching of heavy metals.

Carbonation in alcohol-alkali solutions

Another class of absorbents that has been investigated for CO_2 capture comprises of alkali metal hydroxides dissolved in alcohols. The reaction between alkali hydroxides and alcohols, forming alkoxides that subsequently react with CO_2, was originally proposed as a route for synthesizing metal alkyl carbonates as precursors for organic synthesis [85,86]. Subsequently, the concept of employing alkali-alcohol solutions as CO_2 capture solvents was introduced in a series of studies published between 2015 and 2022 by Jung-Ho Wee and his group [87–92]. In these studies, CO_2 absorption from a gas mixture of 33% CO_2 balanced with N_2 was investigated using solutions of NaOH or KOH in ethanol or methanol, with varying water contents. The authors concluded that an increased water content favors the formation of alkali metal bicarbonates, whereas anhydrous conditions promote the formation of alkali alkyl carbonates, according to the following equations [90–92].

Dissolution of MOH in aqueous-alcohol solutions (where M=Na or K and R=CH_3, or C_2H_5):

$$ROH_{(l)} + MOH_{(s)} \rightarrow ROH_{(l)} + M^{+}_{(sln)} + OH^{+}_{(sln)} \quad (1.11)$$

Upon introduction of CO_2, the dissociated MOH reacts to form metal carbonates or bicarbonates, which may remain dissolved or precipitate depending on the water content of the system:

$$2MOH_{(sln)} + CO_{2(g)} \rightarrow M_2CO_{3(aq,s)} + H_2O_{(l)} \quad (1.12)$$

$$2MOH_{(sln)} + CO_{2(g)} \rightarrow MHCO_{3(aq,s)} \quad (1.13)$$

Under anhydrous conditions, the MOH and ROH react towards the formation of metal alkoxide, which subsequently reacts with CO_2 to form metal alkyl carbonates:

$$ROH_{(l)} + MOH_{(sln)} \rightarrow ROM_{(sln)} + H_2O_{(l)} \quad (1.14)$$

$$ROM_{(sln)} + CO_{2(g)} \rightarrow ROCOOM_{(s)} \quad (1.15)$$

The metal alkyl carbonates can also react with water if it is present in the solution and form metal bicarbonates:

$$ROCOOM_{(s)} + H_2O_{(l)} \rightarrow MHCO_{3(s)} + ROH_{(l)} \quad (1.16)$$

The precipitation of solid products offers a significant advantage over conventional aqueous alkali systems by facilitating solid-liquid separation. In another study, the absorption of CO_2 in ethanol solutions of (Na, K)OH was proposed for the formation of bicarbonate and alkyl carbonate species which were used as intermediates for the catalytic synthesis of methanol [93]. Absorbent solutions of 20 g/L NaOH in ethanol and ethylene glycol and 28.05 g/L of KOH in ethylene glycol were investigated. The absorption of CO_2 from a gas mixture of 10% CO_2 and 90% compressed air in various 1 mol/L solutions of NaOH and KOH in solvent mixtures of water with alcohols has also been studied [94]. The addition of alcohols in water was reported to enhance the capture of CO_2 by increasing the basicity and lowering the surface tension. Furthermore, the addition of ethanol lowers the boiling point of the solvent, thus facilitating its recovery by heating, as presented in the same work.

In **Paper VI**, the use of NaOH-ethanol solutions at concentrations ranging from 2 to 10 g L^{-1} was investigated for CO_2 capture in a bubble column reactor. During this work it was observed that freshly prepared NaOH-ethanol solutions readily absorbed CO_2 from ambient air, transitioning from a clear to a cloudy appearance within a few minutes. This, along with previous literature, suggests that this system might be an attractive absorbent for DAC.

Summary

Chapter 1 has introduced the concepts of CC, technologies and pathways for CO_2 removal, and inorganic carbonation. The focus of this work is on the utilization of alkali (Na, K) and alkaline earth (Ca, Mg) metals in CO_2 absorption. These metals can be found in abundance in alkaline industrial by-products, such as steel slags, GLD, MSWI ashes, etc. This presents an opportunity to utilize materials which are readily available at industrial sites in CC, thus reducing logistic costs and eliminating the requirement for energy and raw feedstocks associated with synthesizing new chemicals for CC. To this end, the primary focal point of the thesis is on the utilization of two key by-products generated in abundance in the Swedish industrial sector: steel slags and pulp and paper side-streams. Höganäs provided three steel slags, tunnel kiln (TK) slag, which is generated from the direct reduction of iron, EAF slag and LF slag, with commercial names Petrit T, Petrit E and Petrit L, respectively. GLD was provided by SCA, while black liquor was produced in the lab. The second focal point of the study is on the evaluation of DAC using NaOH solutions in ethanol. The interest in this absorbent system lies in the fast kinetics of carbonation between CO_2 and NaOH coupled with the insolubility of the products in ethanol, which drives the reaction forward, instead of reaching an equilibrium.

The following chapters are organized as follows: Chapter 2 presents the experimental setup of carbonation for each of the studies. A custom bubble column reactor was designed with the aim to induce gas-liquid phase mixing without energy requirements. The configuration, benefits and limitations of the reactor are discussed. The materials, methodology and analysis technics employed in each study are also reported in this chapter. Chapter 3 follows with the first experimental data, based on **Papers I and II**. The carbonation setup is first evaluated with aqueous NaOH solutions at a range of concentrations, and subsequently, black liquor, an aqueous NaOH-solution containing discarded biomass compounds from the pulp process, was evaluated in CO_2 absorption. Chapter 4 offers an evaluation of Ca and Mg containing side-streams in CO_2 sequestration, grounded on the work of **Papers III, IV and V**. Direct aqueous carbonation is chosen as the preferred method of carbonation to avoid intense operating conditions and multiple steps, which act as setbacks to the industrial implementation of accelerated carbonation. Thus, slurries of GLD and steel slags are investigated in CO_2 sequestration changing various parameters, such as the S/L ratio, particle size and temperature. The formation of carbonate species is examined. Chapter 5 covers the final study of the thesis on the potential of NaOH-ethanol solutions in DAC, derived from **Paper VI**. The performance of two types of reactors is evaluated and the solid Na_2CO_3 formed is characterized in terms of morphology and impurities. The work is concluded with Chapter 6, which highlights the key conclusions of the work, addresses the possibilities and limitations of upscaling each process and underlines pathways of future exploration.

Chapter 2: Experimental setup

Key elements of the setup

Reactor design

Reactor design is a key element for the scale-up of a process. In gas-liquid mixing systems, the reactor type controls the contact between the two phases, while directly affecting the energy demand of the process. In the gas-liquid carbonation systems studied here, the mass transfer of CO_2 from the gaseous to the liquid phase is a significant limiting factor for the overall reaction rate, thus the generation of sufficient mixing between the phases is critical for the efficiency of the carbonation process. With that in mind, simplicity and low energy demand are also decisive aspects when it comes to upscaling. With focus on scalability, two widely known types of reactors were used in this work, bubble columns and stirred tanks. Both were operating as semi-batch reactors, with constant flow of gas through a stationary liquid phase.

Bubble column reactor

The simplest form of bubble column is a vertical cylinder containing the liquid in which the gas enters from the bottom [95]. The upwards movement of the gas bubbles induces turbulence, which facilitates the mixing of the gas and liquid without the requirement for stirring. Lowering the gas bubble size increases the surface area between the two phases, thus porous spargers are often used to generate small bubbles that disperse homogeneously inside the column. When a solid phase is also introduced, either as a precipitated product (e.g. in an oversaturated $NaHCO_3$ solution), or as a reactant (e.g. solid particles of steel slag composed of undissolved mineral phases), the performance and maintenance of porous spargers become tedious. To solve this issue, a porous sparger was used when feasible, replaced by a glass tube for more complex systems where the sparger failed. Most of the experiments were conducted in a custom 3D printed bubble column reactor. This was designed using Fusion 360 and printed in a stereolithography (SLA) 3D printer (Formlabs, Form 3+). It can be divided into two parts, a narrow and long neck where the mixing is intense, and a wider opening that allows the insertion of probes, such as a pH probe, to track the evolution of the carbonation reactions in-line. Figure 2.1 shows the shape and dimensions of the reactor.

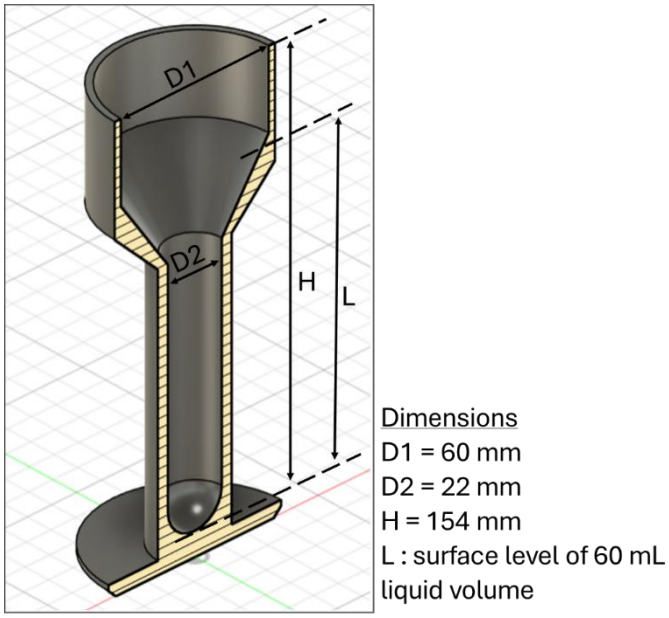

Figure 2.1. *Design and dimensions of the 3D printed bubble column reactor.*

Figure 2.2 shows a general schematic representation (A) and a picture (B) of the experimental setup with this reactor. A gas mixture of CO_2 and N_2 was flown through the gas inlet at the bottom of the reactor that was filled with the absorbent, and the spent gas escaped through the outlet at the top of the reactor. The gas flow was controlled either with an analog flow controller or with Mass Flow Controllers (MFC). In-line monitoring of the pH and/or FTIR of the absorbent was conducted near the top of the reactor. As will be seen in later chapters this reactor performs quite well when it comes to aqueous NaOH solutions, or aqueous slurries of solids (steel slags, GLD, etc.). However, the introduction of more complex behaviors such as foaming or gelling can result in reduced performance or failure of the reactor. Such behaviors were observed in black liquor and solutions of NaOH in ethanol. These cases prompted the employment of stirred reactors to suppress the effects caused by changes in viscosity and surface tension.

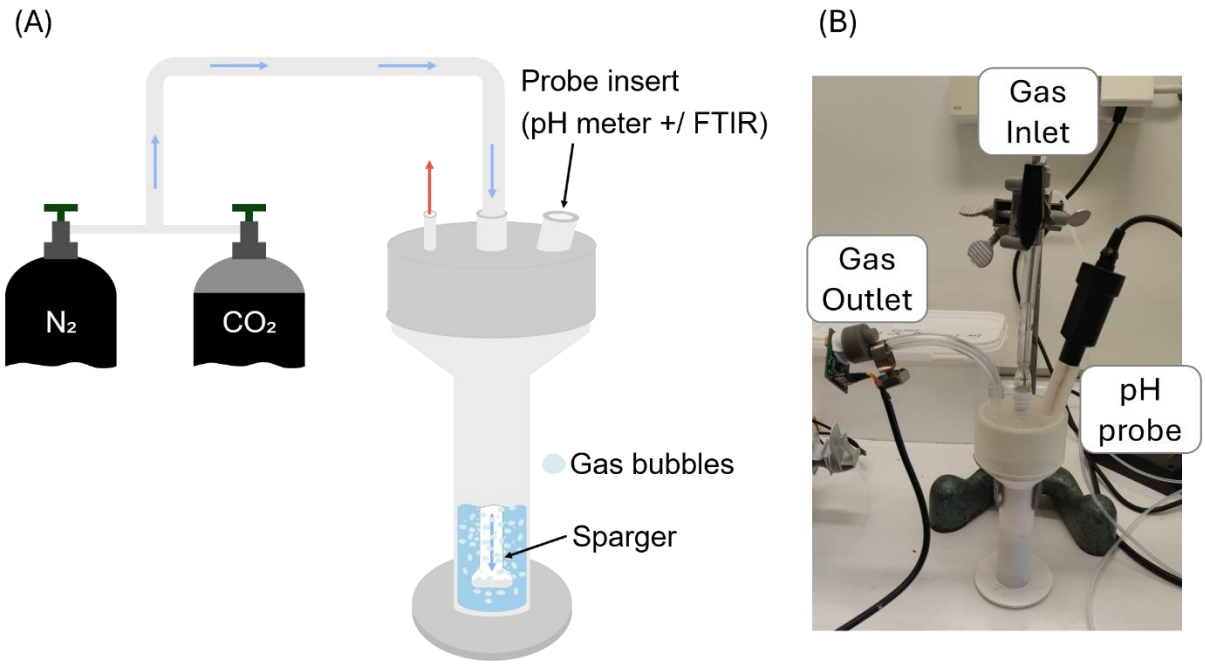

Figure 2.2. *(A) General schematic representation of the experimental setup, and (B) Picture of the reactor in the laboratory.*

The case of black liquor

Black liquor contains lignin fragments, fatty acids and other compounds which are surface active at high pH and promote the formation of stable foams [96,97]. Sparging gas through the black liquor caused continuous foaming which overflowed the reactor. An antifoaming agent was added to change the surface tension of the liquid. This somewhat reduced the foaming, but it did not completely resolve the problem, so a mechanical stirrer (IKA®, EUROSTAR Power Control-Visc Stirrer) was also used to break the remaining foam. The behavior of the black liquor in the two types of reactors is shown in Figure 2.3.

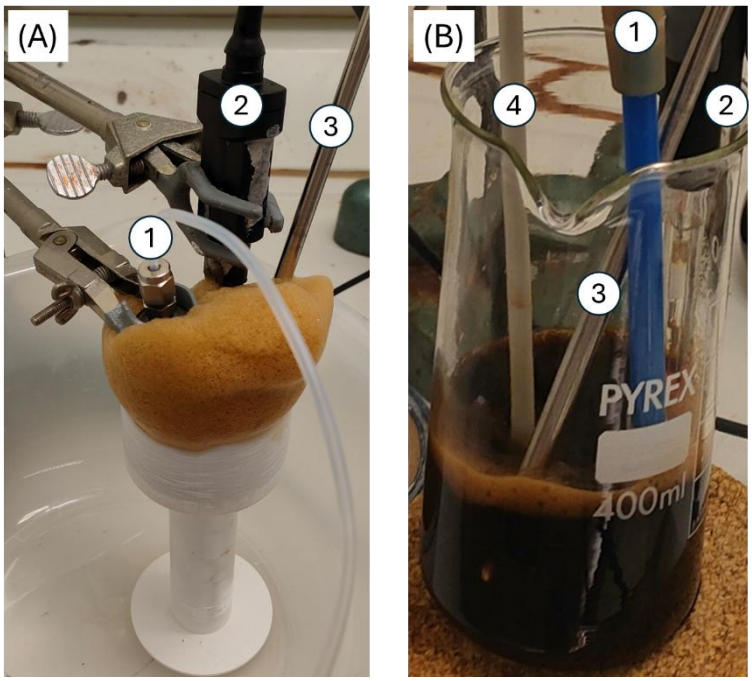

Figure 2.3. *Setup of black liquor carbonation in (A) the 3D printed reactor, and (B) in a stirred reactor. (1) Gas sparger, (2) pH meter, (3) FTIR probe, and (4) stirrer impeller.*

The case of NaOH-ethanol solutions

Absorption of CO_2 in NaOH-ethanol solutions results in the formation of a gel of solid carbonates suspended in the solvent. In **Paper VIII** Baena-Moreno et al. utilized the 3D printed reactor for carbon capture experiments in solutions of 2-10 g/L of NaOH in ethanol [98]. In this study it was reported that the obtained absorption capacity was between 81-94% of the theoretical absorption capacity. It was suggested that the motion of the bubbles was not enough to maintain good mixing, and the gel clogged part of the reactor and/or suppressed the gas-induced motion in the liquid. Therefore, for experiments of NaOH-ethanol solutions with air, two different reactors were evaluated. A glass bubble column with more height and a fritted bottom was employed to increase the gas retention time and force the bubbles to pass through the entire reactor. This was compared with a stirred glass reactor. The two reactors can be seen in Figure 2.4.

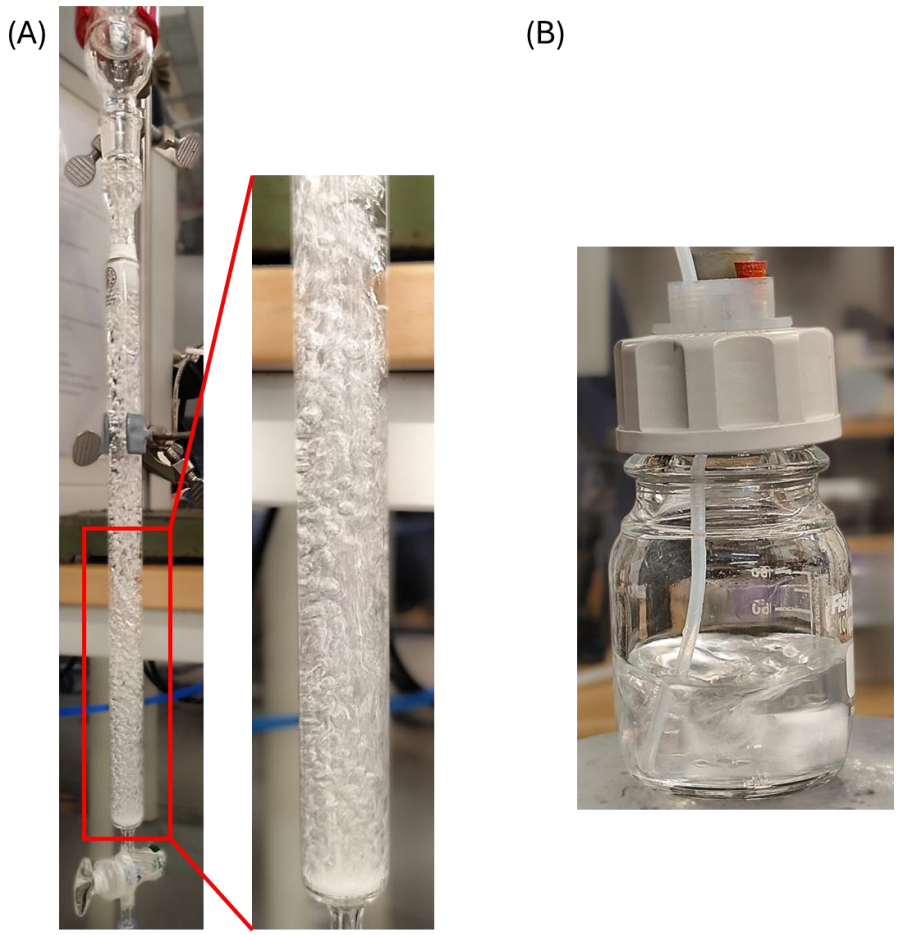

Figure 2.4. *The two reactors used in the NaOH-ethanol DAC experiments: (A) a bubble column and (B) a stirred reactor.*

Magnetic Resonance Imaging of the 3D printed reactor

To test the hypothesis mentioned in **Paper VIII** the reactor was placed in a Magnetic Resonance Imaging (MRI) machine (Bruker Avance III 300MHz with a H^1 transmit/receive probe of 66 mm diameter). 50 mL/min of gas (30% CO_2 and 70% N_2) was sparged continuously into the reactor with 60 mL of NaOH-ethanol solutions. One-shot RARE (Rapid Acquisition with Refocusing Echoes) images enabled visualization of cross sections inside the reactor in a vertical plane, providing information on the effect of the gelation. RARE is an MRI sequence widely used for fast image acquisition. In the context of gas bubbles rising through a bubble column the time scale of the bubble movement is in the range of a few milliseconds [99]. MRI is inherently not a fast technique and image acquisition within timescales that can allow the visualization of gas bubbles in movement pauses a challenge [100]. There is a balance between the spatial resolution, signal to noise ratio and duration of an image. For this study, the settings were optimized to capture the motion inside the reactor with a duration of 900 ms per image. Images were acquired continuously throughout

the experiments. Figure 2.5 shows the pulse sequence of RARE and the optimized settings used for the experiments.

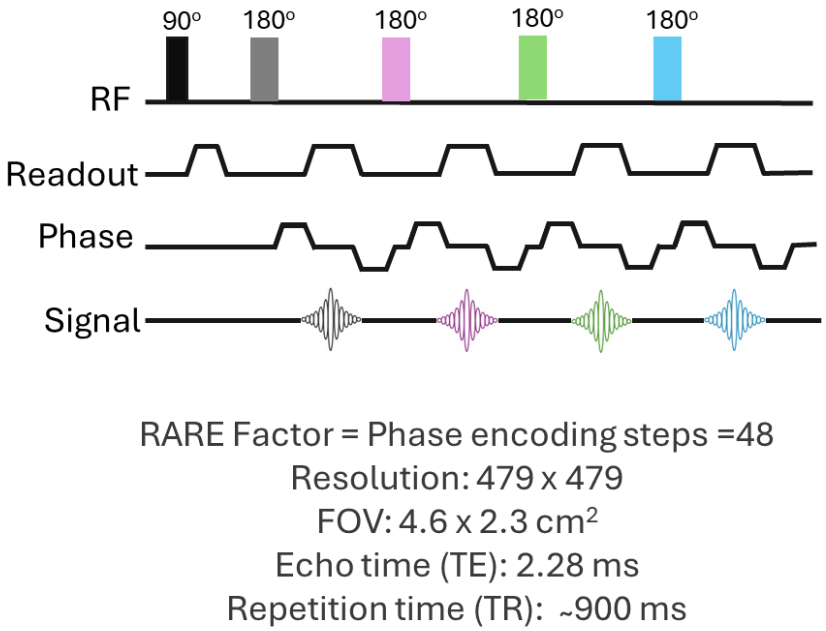

Figure 2.5. *RARE pulse sequence and settings used in the experiments.*

For each experiment a mean flow profile was generated by averaging the signal in each voxel throughout the duration of the experiment. Contours of the mean and standard deviation of the signal throughout the studied region are displayed in Figure 2.6 for 2 and 10 g/L of NaOH in ethanol. The cross section taken was 2.3 by 4.6 cm near the bottom of the reactor. The sparger was placed higher than normal to create a dead zone at the bottom, to better showcase the motion of the liquid. The MRI signal comes from the resonance of the ^{1}H in the system. High signal intensity (bright red) corresponds to the liquid, while low intensity (dark blue) corresponds to regions where the gas is creating turbulence. White colour corresponds to noise, which appears in the sparger and in zones of very intense mixing, leading to no measurable signal. The profiles of mean signal show that the gas bubbles cause significant motion around the sparger, but at the bottom of the reactor the liquid stagnates. The standard deviation reveals which zones maintained a stable signal throughout the experiment, and which zones presented a shift in signal over time. The zone on the left of the sparger had the highest motion throughout the experiments, while the zone on the right of the sparger presented high motion initially, which became lower over time, as suggested by the higher standard deviation. This is visible for both 2 and 10 g/L solutions, although it is more pronounced at the lower concentration. This showcases that the gas flow formed a preferential pathway of motion as the viscosity of the absorbent increased. The stagnation of the liquid at the bottom was more pronounced at the higher

concentration as the viscosity increased more, causing more significant resistance to motion.

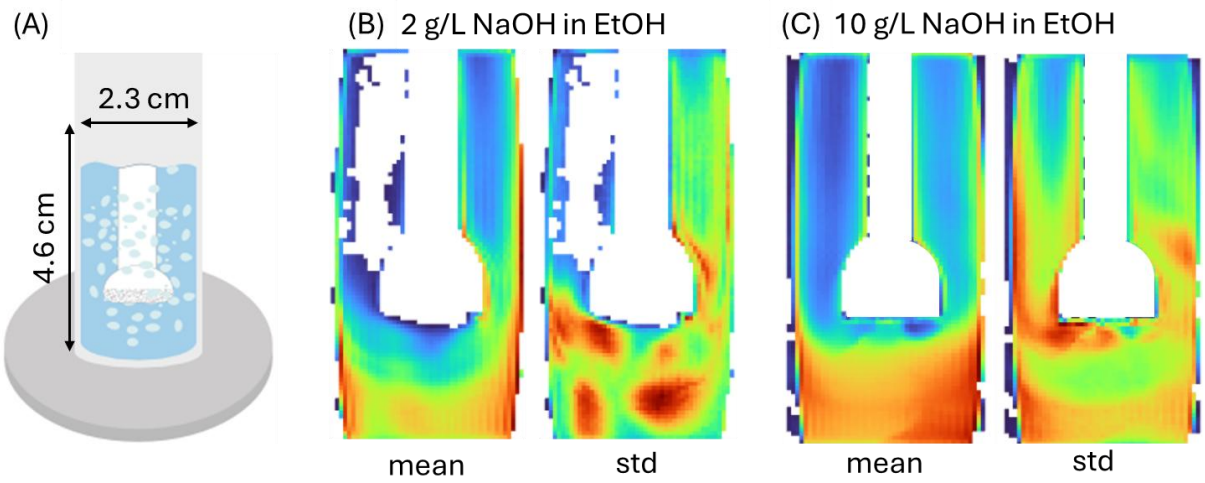

Figure 2.6. *(A) schematic representation of the cross section selected for MR imaging, and the mean signal and standard deviation over time for the (B) 2g/L NaOH-ethanol solution and (C) 10 g/L NaOH-ethanol solution.*

Evolution of the carbonation process

The evolution of the carbonation process and the absorption capacity of each absorbent system were monitored in several ways. As carbonation is an acid-base reaction, a pH meter (HQ430D, HACH) was employed in many cases to track the progression of pH with time inside the reactor. Calibration of the pH meter was performed with calibration standards at pH 4.01, 7 and 10. The initial pH was always alkaline, within the range of 10 to 14. The pH at the end of the experiment was 8 for experiments with aqueous NaOH, as at this pH H_2CO_3 starts to form. The final pH for carbonation with divalent metals (Ca, Mg) was around 7, as the metal carbonates precipitated out of solution. An Attenuated total reflectance Fourier transform infrared (ATR-FTIR) probe (ReactIR 702L, Mettler Toledo) was also used to follow the signal of CO_3^{2-} and HCO_3^-, in-line. The background for the FTIR probe was collected in air, spectra were taken in absorbance mode, at the wavelength range of 3000 to 640.8 cm^{-1} and with a resolution of 4 cm^{-1}. Both the pH meter and FTIR probe were collecting data every 10 seconds.

CO_2 absorption rate and capacity

The uptake of CO_2 was measured either throughout the carbonation experiment, or only at the end, and three different methods were used: gravimetric, CO_2 sensor and acid-gravimetric.

In the gravimetric method an analytical balance (QUINTIX2102-1S, Sartorius), with readability of 0.01 g, was used to monitor the weight of the reactor. The increase of the weight of the reactor during an experiment was a direct result of the absorption of CO_2 into the solution. The weight measurements can be heavily affected by weight losses during the experiment. The two causes of weight loss in the system are solvent evaporation and loss of liquid that is carried away with the gas bubbles. Thus, blank measurements were conducted with sparging only nitrogen and recording the weight decrease.

An alternative method used was to connect a CO_2 gas sensor at the outlet of the reactor. The CO_2 sensors used (ExplorIR, or SprintIR, GSS) operate with the use of a low-power LED optical technology and a nondispersive infrared (NDIR) detector tuned at the wavelength of 4.26 μm, where CO_2 has a particularly strong signal. The sensor was taking measurements of the CO_2 concentration at the outlet in 5 s intervals and the experiment was be stopped once the outlet flow had the same composition of CO_2 as the inlet, meaning that CO_2 was no longer absorbed into the liquid phase. The range of the sensors used was 0 – 20% CO_2 and the flow was typically 15% CO_2 and 85% N_2. The information of the outlet gas % of CO_2 was used to obtain the rate of absorption and absorption capacity in the following way:

Knowing that the inlet flow was F_{in} = 200 mL/min with 85% N_2 and since N_2 is an inert gas that is not held up in the reactor, the outlet flow of N_2 was the same as the inlet

$$F_{OUT,N_2} = F_{IN,N_2} = 200\left(\frac{mL}{min}\right) * 85\% = 170\left(\frac{mL_{N_2}}{min}\right) \tag{2.1}$$

Thus, the total flow rate of the outlet was

$$F_{OUT,N_2} + F_{OUT,CO_2} = 170\left(\frac{mL_{N_2}}{min}\right) + F_{OUT,CO_2}\left(\frac{mL_{CO_2}}{min}\right) \tag{2.2}$$

Based on Equation (2.2), the outlet composition of CO_2 ($CO_2\%_{OUT}$) was

$$CO_2\%_{OUT} = \frac{F_{OUT,CO_2}\left(\frac{mL_{CO_2}}{min}\right)}{170\left(\frac{mL_{N_2}}{min}\right) + F_{OUT,CO_2}\left(\frac{mL_{CO_2}}{min}\right)} \tag{2.3}$$

Thus, the outlet flow of CO_2 (F_{OUT,CO_2}) can be expressed according to Equation (14).

$$F_{OUT,CO_2}\left(\frac{mL_{CO_2}}{min}\right) = \frac{CO_2\%_{OUT} * 170\left(\frac{mL_{N_2}}{min}\right)}{1 - CO_2\%_{OUT}} \quad (2.4)$$

Since $CO_2\%_{OUT}$ was given every 5 s from the sensor, F_{OUT,CO_2} can be deducted from Equation (2.4). The density of CO_2 can be assumed to be $1.8*10^{-3}$ g / mL at 21 °C according to [101]. So, the mass of absorbed CO_2 can be calculated using Equation (2.5).

$$M_{absorbed\ CO_2} = \left(F_{IN,CO_2}\left(\frac{mL_{CO_2}}{min}\right) - F_{OUT,CO_2}\left(\frac{mL_{CO_2}}{min}\right)\right) * 5s * \frac{1}{60}\left(\frac{min}{s}\right) * 0.0018\left(\frac{g}{mL}\right) \quad (2.5)$$

The third method used to determine the CO_2 uptake was by acidifying the carbonates to release gaseous CO_2 and measure the weight loss. This was only conducted on precipitated and separated carbonates for NaOH-ethanol solutions when it was unfeasible to use the CO_2 sensor due to the ethanol vapor damaging the sensor. For this method, 10 mL of 1 M HCl was placed on a balance along with the solid carbonates and the total weight was marked. Then the acid was poured on the precipitates, and the weight loss was recorded once gas bubbles were no longer forming. This method was calibrated with Na_2CO_3. The Na_2CO_3 was placed in a 105 °C oven for 4 hours prior to use to dehydrate it and decompose any $NaHCO_3$ that could have formed over time. More information on the calibration and correction of data can be found in the supplementary information of **Paper VI**. The statistical error generated by this treatment as well as the variance of the measurement method are also discussed in the supplementary information.

Materials

Table 2.1 shows the chemicals used in each study, along with suppliers and preparation methods of the absorbents. In case of the NaOH experiments in water or ethanol, reagent grade chemicals were used. The black liquor was produced in the laboratory, while the by-product and waste materials were provided by Swedish companies. One important consideration in the utilization of waste and by-products as reagents is that their composition is not strictly controlled and it can vary based on the raw materials and operating conditions. Thus, for the sake of comparison, in each study, all experiments were conducted using materials from a single batch.

Table 2.1. *Chemicals, suppliers and absorbent preparation methods for each study.*

Study	Absorbent system	Chemical suppliers	Absorbent preparation	Gas composition*
Paper I	Aqueous NaOH	• NaOH: VWR, 99% purity • 3D printed reactor resin: Rigid 10K, Formlabs	NaOH was dissolved in deionized water at concentrations of 1, 2, 3,4 ,5 6, 7 and 8 wt %	30% CO_2 70% N_2
Paper II	Black liquor	Black liquor: Produced in-house Antifoamer: BIM Kemi	The black liquor was prepared by soda pulping of oat husks and used with the addition of 0.043 g / L of a commercial antifoamer	30% CO_2 70% N_2
Paper III	Petrit T (TK slag), Petrit E (EAF slag) and Petrit L (LF slag)	Höganäs	The solids were mixed with deionized water at S/L ratios of 50, 100, 150 and 200, and stirred for 24 h at 400 rpm. MOH extract solutions were prepared by stirring solids in water at 50 g/L for 24 h and centrifuging.	15% CO_2 85% N_2
Paper IV	GLD and wastewater	SCA	The solids were mixed with deionized water at S/L ratios of 50, 100, 150 and 200, and with wastewater at 50 and 200, and stirred for 24 h at 400 rpm.	15% CO_2 85% N_2
Paper V	Petrit T, L and E slags, and GLD	Höganäs and SCA	The solids were mixed with deionized water at S/L ratio of 50. MOH extract solutions were prepared by stirring solids in water at 50 g/L for 24 h and centrifuging.	15% CO_2 85% N_2
Paper VI	NaOH dissolved in ethanol	• NaOH: SigmaAldrich, ≥98%, anhydrous pellets • Ethanol: Fisher Chemical, absolute ethanol, ≥99.8%) • HCl 1M: Fisher Chemical • Na_2CO_3: VWR, ≥98%	Solutions of NaOH in ethanol at concentrations 10, 20, 30, 40 and 50 g/L were prepared by stirring at 400 rpm, until the NaOH was dissolved.	Compressed air

* All gas bottles were provided by Linde, apart from the compressed air, which is directly connected to the laboratory fumehoods.

The weak black liquor used in carbonation experiments was prepared as follows. Oat husks were subjected to prehydrolysis to loosen the lignocellulosic structure and leach some of the hemicellulose out of the material. During this process, the raw material was immersed in a weak acid inside a 1.5 L steel autoclave which rotated at a speed of 15 rpm, at 160 °C [102]. Following that, the pretreated husks were washed thoroughly with deionized water until the pH of the washing water was neutral. Finally, the soda pulping process was used to extract the pulp from the rest of the material. The pretreated material was added again to the same autoclave together with an aqueous solution of 4% w/w of NaOH and was rotated at the same speed at 170 °C for 2 h [103]. After cooking, the product was filtered to separate the pulp from the weak black liquor. The dry solid weight of the liquor was determined by drying it in an oven at 50 °C. The composition of the black liquor is presented in Table 2.2.

Table 2.2. *Composition of the oat husk black liquor used in the experiments.*

Composition	**Amount (wt %)**
Total solids (TS)	8
Compounds in TS	
Klason lignin	19.4
Acid soluble lignin	6.4
Glucose	0.3
Xylose	0.1
Elements	Amount (ppm)
Na	20,951.4
Si	1440.2

Three commercial steel slags were provided by Höganäs (see Table 2.1). Their composition expressed in metal oxides can be seen in Table 2.3. The main crystalline phases in each slag were Ca_2SiO_4 (larnite), $Ca_2Al_2SiO_7$ (gehlenite) and CaO (lime) in Petrit T, Ca_2SiO_4 (larnite), $Ca_2(Al,Fe)_2O_5$ (brownmillerite) and Feo (wuestite) in Petrit E, and MgO (periclase), Ca_2SiO_4 (calcio-olivine), $Ca(OH)_2$ (portlandite) and $Ca_3Al_2O_6$ (tricalcium aluminate) in Petrit L. This data was obtained by XRD analysis conducted at Luleå University and provided by Höganäs. It must be noted that this analysis was not conducted on the same batch that was used in this work. Steel slag slurries were prepared by mixing the solids with deionized water at 50, 100, 150 and 200 S/L ratios and stirring at 400 rpm for 24 h. To investigate the effect of the metal ions dissolution in water, control experiments were conducted where mixtures of S/L = 50 were stirred for 24 h and then centrifuged to separate the supernatants (liquid phase) from the

pellets (solid phase). Subsequently, carbonation experiments were performed only on the supernatants.

Table 2.3. *Composition of the Höganäs steel slags and their annual production. The average composition data are available at the company site, while specific data for the batches used were provided by the company.*

Chemical (wt %)	**Petrit T**		**Petrit E**		**Petrit L**	
	Average	Batch used	Average	Batch used	Average	Batch used
CaO	37	32.30	40	41.6	48	42.70
MgO	–	1.74	10	8.57	13	16.90
SiO_2	18	20.40	15	17.90	11	15.30
Al_2O_3	9	11.50	6.5	8.72	9	12.10
FeO	–	–	25	22.2	13	13.80
Fe_2O_3	7	9.68	–	–	–	–
MnO	–	0.26	–	4.19	–	1.97
C	–	17.30	–	0.25	–	0.64
S	20	1.15	–	0.16	–	0.13
Annual production (kton)	17 – 20		15 – 18		4 – 5	

The GLD was obtained from SCA. Its composition is given in Table 2.4. The same company also supplied wastewater, which comes from a combination of water streams generated through the pulping process, and it mainly contains NaOH, Na_2S, $Na_2S_2O_3$, Na_2SO_4, Na_2CO_3, and KSO_3. Slurries were prepared by mixing the solids with deionized water at S/L ratios of 50, 100, 150 and 200 and with wastewater at 50 and 200 and stirring at 400 rpm for 24 h.

Table 2.4. *Main composition of GLD.*

Chemical (wt %)	**Amount (wt %)**
CaO	25
MgO	12.5
SiO_2	1.86
Al_2O_3	0.92
Fe_2O_3	0.44
MnO	2.44
Na_2O	3.76
Annual production in Sweden (kton)	240

The gas mixtures used were 15 or 30% CO_2 balanced with N_2, to simulate the concentration of CO_2 in industrial flue gases. For the DAC experiments compressed air was used. Values of the air humidity and CO_2 concentration were collected over 5 minutes with 5 s intervals. The humidity was about 7.6 % and the CO_2 concentration was 476 ppm ±11ppm.

Methodology

Table 2.5 presents a summary of the carbonation methodology and physicochemical characterization techniques used in each study. These will be discussed in detail below.

Table 2.5. *Summary of the experimental methodology and analytical techniques used in each study discussed in the thesis.*

Study	Description	Reactor	Conditions	Carbonation monitoring	Characteriz. of products
Paper I	Carbon capture with aqueous NaOH	3D printed reactor (60 mL)	• Gas flow: 200 mL/min • Ambient T and P	• In-line pH meter and FTIR • Gravimetric measurement of CO_2 uptake during the experiments	SEM and XRD
Paper II	Carbon capture with weak black liquor	Glass reactor (100 mL) stirred at 700 rpm	• Gas flow: 200 mL/min • Ambient T and P	• In-line pH meter and FTIR • Gravimetric measurement of CO_2 uptake at the end of the experiments	NMR, SEM, XRD and optical microscopy
Paper III	Steel slag carbonation	3D printed reactor (60 mL)	• Gas flow: 200 mL/min • Ambient T and P	• In-line pH meter • CO_2 sensor	ATR-FTIR, SEM-EDS, XRD-Rietveld
Paper IV	GLD carbonation				SEM-EDS, XRD
Paper V	Effect of particle size, temperature, and wetting time in steel slag and GLD carbonation	Glass reactor (60 mL) stirred at 400 rpm inside a water bath	• Gas flow: 200 mL/min • Varied T, ambient P	• In-line pH meter • CO_2 sensor	SEM-EDS, XRD-Rietveld
Paper VI	NaOH-ethanol DAC	Glass bubble column with fritted bottom (40 mL), or Glass reactor (40 mL) stirred at 300 rpm	• Gas flow: 800 mL/min • Ambient T and P	HCl gravimetric measurement of CO_2 uptake at the end of the experiments	NMR, FTIR, XRD, SEM

NaOH and Black liquor carbonation experiments

A gas mixture of 30% CO_2 balanced with N_2 was sparged through the reactor at a rate of 200 mL/min. The 3D printed reactor was used for the aqueous NaOH experiments, while a stirred reactor was used for the black liquor as discussed above. Each carbonation experiment was carried out in two different setups. In the first setup, the pH meter and FTIR probe were connected to follow the carbonation process. Once the pH of the solution reached 8 the experiment was stopped. In the second setup, the experiment was repeated for the same duration of time without any probe inserts, and the CO_2 uptake was determined gravimetrically. For the aqueous NaOH solutions the 3D printed reactor was mounted on the balance, and the weight was recorded with time. For the black liquor, the vibrations caused by stirring inhibited the use of the balance in real time, thus instead the weight of the reactor was compared at the beginning and end of each experiment.

The NaOH solutions with ≥5 wt% concentration and above exhibited solid precipitation during the carbonation reactions. The 6 wt% carbonated solution was filtered and the separated solids were dried at ambient temperature. The carbonated black liquor was treated as follows: A part of the liquid was dried in an oven at 70 °C without further processing. Another part was filtered using filter paper number 3 (Munktell), to separate the precipitated solids from the rest of the liquid. Then both the residue and the filtrate were placed in an oven at 70 °C for two days. A sample of non-carbonated black liquor was also dried. The solid samples were ground to a fine powder and then studied with Powder XRD (D8 Discover, Bruker). The patterns were recorded for a diffraction angle range of 2θ from 10 to 70° with a scan step of 0.02° per second. The diffractograms were recorded using the software DIFFRAC.EVA V5.2 and the Crystallography Open Database was used to analyze and recognize the patterns. The samples were also subjected to SEM (Phenom ProX, ThermoFisher Scientific) and the carbonated black liquor solids were also put under an optical microscope (ZEISS SteREO Discovery.V12). Black liquor before and after carbonation was also analyzed with liquid state ^{13}C NMR. The spectra were recorded on a Bruker Avance III HD (700 MHz ^{1}H) equipped with a QCI cryoprobe. The samples were transferred to an NMR tube, and a small amount of D_2O (Sigma, 99.8% D) was added to lock and shim the sample. A *z*-restored spin-echo pulse sequence was used with 8192 scans and a repetition time of 0.1 s [104]. An exponential window function of 20 Hz was applied before the baseline correction

Steel slag and GLD carbonation experiments

A gas mixture of 15 % CO_2 balanced with N_2 was sparged through the 3D printed reactor at the rate of 200 mL/min, set with MFCs (Brooks Instrument). The reactor's outlet

was connected to a CO_2 sensor (ExplorIR, GSS) measuring the CO_2 concentration every 5 s. A pH meter was also connected to follow the pH of the mixture with 10 s interval measurements. Each experiment was stopped when the CO_2 reading of the sensor had reached a set value. Typically, the CO_2 reading would plateau at the inlet concentration marking the end of the experiment. In cases where the carbonation process lasted very long and the CO_2 reading took a long time to reach the inlet concentration, the experiment was instead stopped when the CO_2 outlet concentration was 14 %.

The effect of temperature, particle size and stirring time were also investigated for these materials. For this study, the S/L ratio was fixed at 50 and the carbonation experiments were conducted in a stirred reactor at 400 rpm. For the temperature experiments, the reactor was placed in a water bath and the temperature was set to 25 °C and 60 °C. This setup can be seen in Figure 2.7. The steel slag and GLD slurries were stirred for 24 h and 2 h, respectively, prior to carbonation.

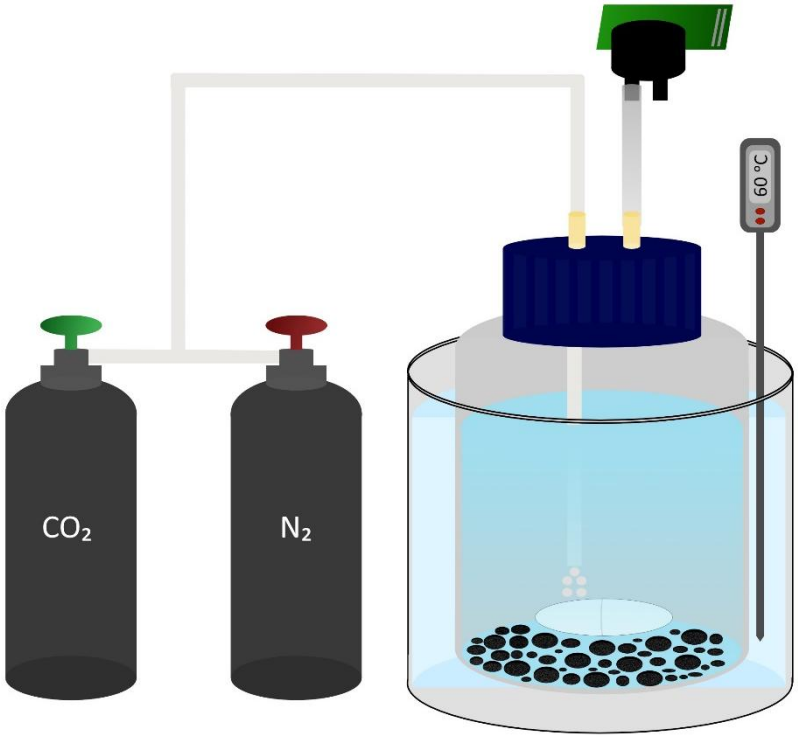

Figure 2.7. *Schematic representation of the setup for different temperatures.*

For the effect of particle size the same reactor and stirring times were used and the carbonation took place at 25 °C. Petrit E and Petrit L consist of both powder and rocks in their composition. The powder was obtained by sifting the samples through a 1 mm sieve, and experiments were conducted for both powder and rock particles. For GLD, experiments were conducted using both the material as received and a crushed GLD sample. Petrit T was excluded from this study because it is a powder. The effect of the stirring time prior to carbonation was evaluated by stirring the slurries for 2, 4 and 24 h. To isolate the effect of stirring time in the extraction of metal ions, samples were

stirred for 2, 4 and 24 h, followed by centrifugation to separate the precipitates from the supernatants. Experiments were conducted using the supernatants under the same conditions.

Some of the experiments were replicated to evaluate the variability of the experiments and TGA analysis was performed on selected samples to further corroborate the CO_2 uptake values measured with the CO_2 sensor. More information on the TGA analysis and statistical error calculations is provided in the supplementary information of **Paper V**. This treatment was only applied to the experiments conducted in the stirred reactor and therefore error bars were only applied to the data generated with this reactor.

The raw materials (steel slags and GLD) were analyzed with a High Throughput Surface Area and Porosity Analyzer (TriStar3000, Micromeritics) to determine their Brunauer-Emmett-Teller (BET) surface area. The adsorbent gas was N_2 (77 K) and the samples were dried in the SmartPrep instrument (Micromeritics) at 150 °C for 20 h, under nitrogen flow, to remove moisture before the measurement. To evaluate the stability of the materials during high-temperature degassing, as well as to corroborate the results of carbon dioxide uptake with another technique, samples were subjected to TGA (TGA/DSC 3+ STAR System, Mettler Toledo). The temperature range was 40 – 900 °C with a ramp of 10 °C/min and N_2 flow of 60 mL/min. The morphology of the materials before and after carbonation was studied with SEM (FEI Quanta 200 FEG ESEM) at 20 kV. To obtain information on the particle size of the materials RBG camera and SEM images were analyzed with the software FIJI (ImageJ), by measuring the dimensions of 40-60 particles for each material. Energy-Dispersive X-ray Spectroscopy (EDS) was also performed to identify the elemental composition of the different structures. The crystal phases of the materials before and after carbonation were studied with XRD (D8 Discover, Brucker), over a diffraction angle range from 10 to 70° with a scan step of 0.04°/s. The QualX2.0 program (Altomare et al., n.d.) was used to identify the crystalline phases [105]. Quantitative Phase Analysis (QPA) by Rietveld method (Paufler, 1995) [106] was also performed using the TOPAS Academic suite program ("TOPAS-R, Version 4.2" 2009) [107]. The steel slags before and after carbonation were also analyzed with Solid state ATR-FTIR (Bruker Vertex70v). Each analysis was accumulated by 64 scans in a range from 4000 to 400 cm^{-1} with a resolution of 4 cm^{-1} using an RT-DLaTGS detector.

NaOH-ethanol DAC experiments

Two types of reactors were employed for this study, a bubble column and a stirred reactor (Figure 2.4). The methodology followed in these experiments is presented in Figure 2.8. Both reactors help 40 mL of absorbent and air with flow rate of 800 mL/min was sparged through for 8 h. The high airflow caused rapid ethanol

evaporation. Thus, a condensation column was fitted above the bubble column and was kept at 7 °C with an isopropanol cooling bath (F25-ME Refrigerated/Heating Circulator, Julabo). Even so, ethanol was replenished to reach 40 mL halfway through the experiments. In the stirred reactor, the stirring further enhanced ethanol evaporation. Ethanol was again replenished halfway through and even so very little remained by the end of each experiment. DAC experiments in the stirred reactor were also performed at temperatures of -20 and 45 °C with the 10 g NaOH/L solution. The -20 °C experiment was conducted by immersing the stirred reactor in a jacketed bottle filled with isopropanol, which was maintained at -20 °C. No ethanol was added for the duration of the experiment, because its evaporation was almost insignificant. The 45 °C experiment was conducted by immersing the stirred reactor in a water bath and turning on the heating plate of the magnetic stirrer. At this temperature, the evaporation of ethanol was significantly faster, and the solvent was replenished by adding approximately 20 mL every hour. In both cases, the temperature of the bath was recorded with a thermometer and was found to be stable throughout the experiments.

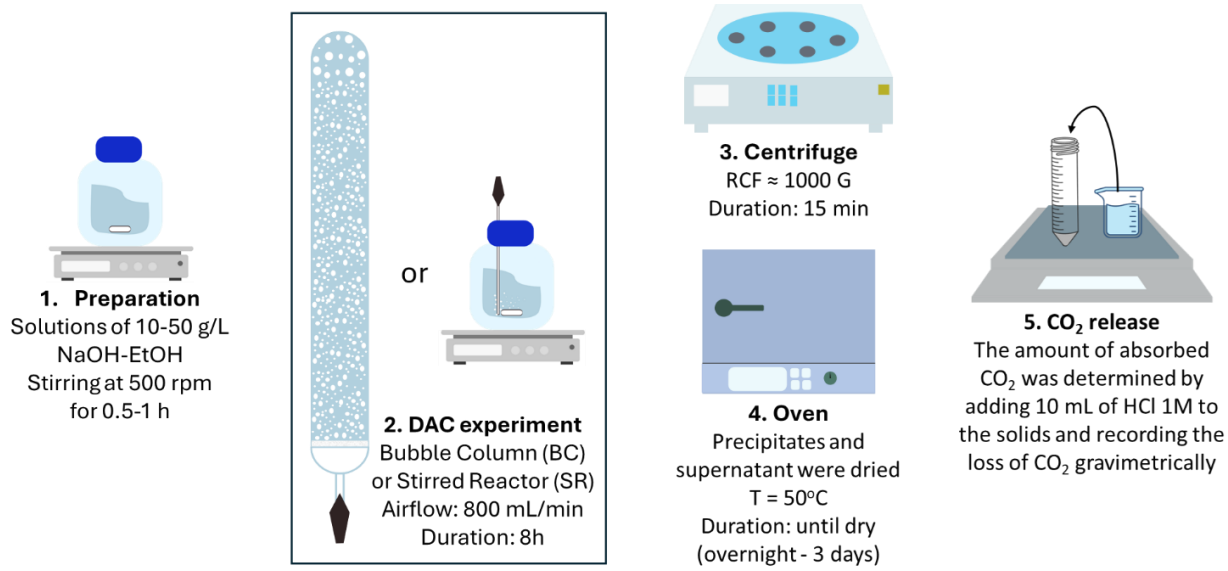

Figure 2.8. *Schematic representation of the methodology followed in the DAC experiments.*

Various characterization techniques were used to investigate the types and structures of carbonates formed in the DAC experiments. Solution ^{1}H and ^{13}C NMR experiments were conducted on a Bruker Avance III HD (700 MHz ^{1}H) equipped with a QCI cryoprobe. The analyzed samples were solid precipitates of NaOH-ethanol 10 and 50 g/L, the dried supernatants of the same solutions, and the liquid supernatant of the NaOH-ethanol 30 g/L solution collected right after centrifugation. The samples were dissolved in a small amount of D_2O (Sigma, 99.8% D) which was used to lock and shim. Samples were also analyzed with ATR-FTIR (Perkin Elmer Frontier) to corroborate the NMR findings. The spectra were obtained in the range of 4000 to 400 cm^{-1}, based on

32 scans with a resolution of 4 cm^{-1}. XRD (D8 Discover Bruker) was employed to evaluate the crystalline forms of carbonates for the 10, 30 and 50 g/L precipitates. The diffraction angle range (2θ) of the diffractograms was 10 – 70° with a scan step of 0.02° per second. The diffractograms were recorded in the software DIFFRAC.EVA V5.2 and the patterns were analyzed with the Crystallography Open Database. Lastly, SEM (FEI Quanta 200 FEG ESEM) was used to observe the morphology and size of the crystal structures of the precipitated carbonates. The samples were coated with a 4nm layer of gold to enhance the signal/noise ratio. Images were recorded at 20 kV using a secondary electron detector (LED).

Chapter 3: Carbon capture with aqueous NaOH-based absorbents

Based on **Papers I and II**

Overview

The focus of this chapter is the use of aqueous NaOH systems for CO_2 absorption. A model system was first built with standard NaOH solutions at the concentration range of 1 – 8 wt% to establish a method for monitoring the carbonation process in real-time and evaluate the performance of the 3D printed reactor. This was followed by the investigation of black liquor as the absorbent. The carbonation process was followed in-line with an FTIR probe and a pH meter, while the CO_2 uptake was measured gravimetrically. The black liquor absorbed around 30 g of CO_2 / L. The carbonation products were characterized with SEM and XRD.

In-line monitoring of the carbonation reactions

The presence of CO_3^{2-} and HCO_3^- in solution can be detected using FTIR. CO_3^{2-} has a characteristic band of asymmetric stretching of the C–O bonds around 1395 cm^{-1}. HCO_3^- has bands of C–O symmetric stretching at 1365 cm^{-1}, C–OH bending at 1300 cm^{-1}, C–OH and C–O asymmetric stretching at 1005 and 1650 cm^{-1} respectively [108]. Water is also detectable, with a strong band at 1640 cm^{-1}. In the experiments described here the asymmetric stretching band of CO_3^{2-} was slightly shifted to 1388 cm^{-1}. The bands at 1388, 1365 and 1300 cm^{-1} were partially overlapping and the HCO_3^- band at 1650 cm^{-1} was hidden by the very prominent water band. Figure 3.1 depicts the evolution of the FTIR spectra for the carbonation experiment with 4% NaOH in a surface (A) and contour (B) plot. In the figure, the spectra are focused on the range of 1480 to 960 cm^{-1} to isolate the progression of the CO_3^{2-} and HCO_3^- bands. Initially there were no bands of CO_3^{2-} or HCO_3^-. As the gas bubbling started, the CO_3^{2-} band became visible and increased in intensity over time. Gradually the 1388 cm^{-1} band shifted to the right, while bands at 1300 and 1008 cm^{-1} emerged, signifying that the chemical equilibrium was shifted towards the formation of HCO_3^-. At the end of the experiment the HCO_3^- bands were at their peak intensity.

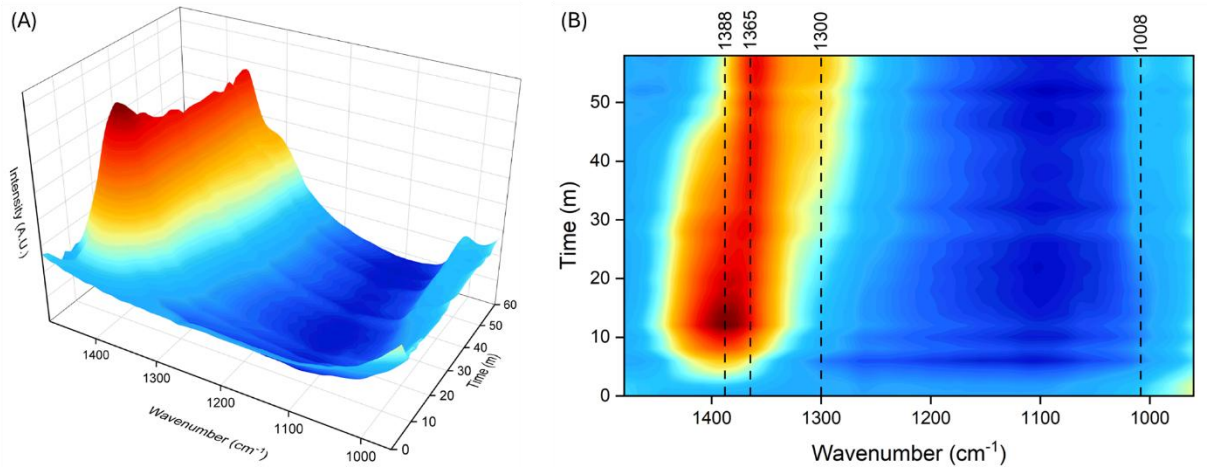

Figure 3.1. *(A) Surface plot and (B) contour plot of the FTIR spectra during the carbonation of the 4 wt% NaOH solution.*

The same peak evolution was observed at all NaOH concentrations within the 1 – 8 wt% range, but at different intensities. At 1 and 2 wt% the CO_3^{2-} and HCO_3^- bands were insignificant compared to the water peak, but in the solutions above 3 wt% the spectral changes were much more significant. The FTIR spectra over time for different NaOH concentrations are shown in Figure 3.2.

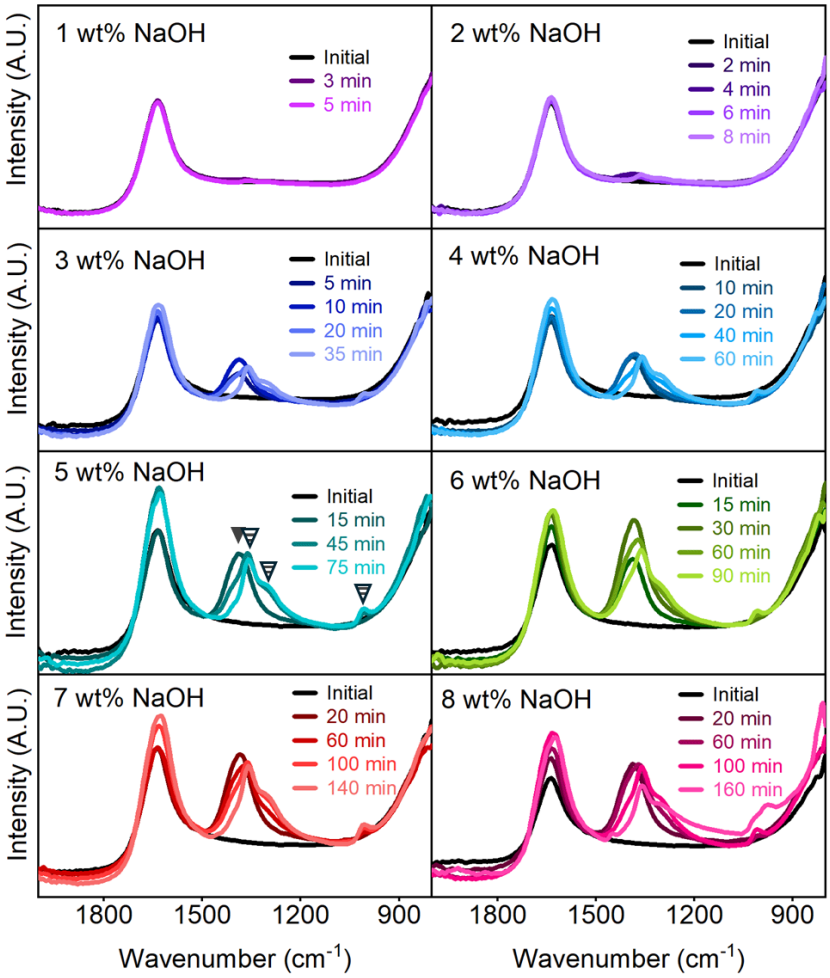

Figure 3.2. *FTIR spectra of CO_2 absorption in the NaOH solutions over time. In the spectra of 5 wt% NaOH the arrow with solid fill marks the peak of CO_3^{2-} at 1380 cm^{-1} and the dashed arrows mark the peaks of HCO_3^- at 1360, 1300, and 1008 cm^{-1}.*

The evolution of CO_2 uptake, pH, CO_3^{2-} and HCO_3^- for the 4 wt% NaOH solution are displayed combined in Figure 3.3. To follow the CO_3^{2-} and HCO_3^- more clearly the absorbance intensity at the range of 1372 – 1388 cm^{-1} and 1000 – 1016 cm^{-1} was isolated and followed with time. It should be noted that this is not a quantitative representation of the concentrations of the CO_3^{2-} and HCO_3^- as the bands of the two species are convoluted and the spectral baseline was not constant overtime. In Figure 3.3(A) three distinct CO_2 uptake regions can be observed. In the first 6 minutes the CO_2 uptake rate was the highest, while the pH was slowly decreasing (Figure 3.3B) and the CO_2 was converted to CO_3^{2-} following equation (1.4) (Figure 3.3C). High pH favors the instantaneous reaction between CO_2 and OH^- towards the formation of CO_3^{2-}, so at this stage the mass transport of the gaseous CO_2 into the liquid phase is the limiting factor. The next section, between 6 and 24.5 minutes, displayed slower CO_2 absorption. In this section there was a rapid pH drop at the time where the CO_3^{2-} concentration was at its maximum and upon this the HCO_3^- band appeared. Thus, the inflection point at pH

11.2 marked the complete shift of equation (1.4) to the right and the start of equation (1.5). The CO_2 uptake until the inflection point was 19.9 g/L of solution. The last section had the slowest CO_2 uptake, lasting 35 minutes from pH 9.6 until 8. At this pH range both the new CO_2 that flows into the reactor and the CO_3^{2-} in solution turn into HCO_3^-. The total CO_2 uptake after 1 hour was 41.7 g/L. These results fall in line with previous literature and the in-line FTIR spectra provided additional insight into the evolution of the CO_3^{2-} and HCO_3^- species [22].

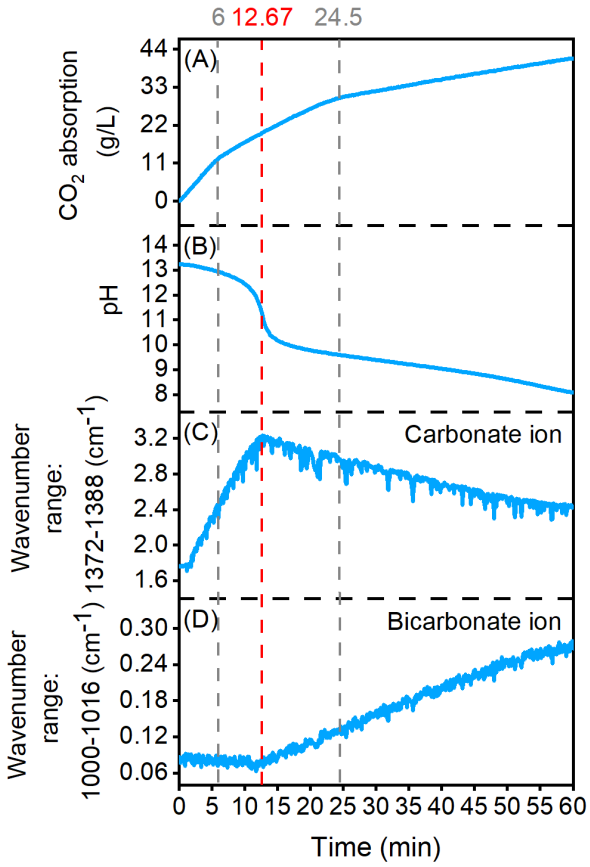

Figure 3.3. *(A) CO_2 absorption, (B) pH, (C) Sum of the absorbance intensities of the wavenumber range 1372– 1388 cm^{-1} corresponding to the CO_3^{2-} region and (D) Sum of the absorbance intensity of the wavenumber range 1000 – 1016 cm^{-1} corresponding to the HCO_3^- region with time for 4 wt% NaOH.*

The black liquor had been produced by soda pulping with a 4 wt% NaOH solution and was thus expected to behave similarly to the standard 4 wt% NaOH solution. FTIR showed that the solution contained CO_3^{2-} before the experiment. Figure 3.4A shows the small band at 1390 cm^{-1} present in the spectrum of black liquor before carbonation. Figure 3.4B depicts the progression of the FTIR spectra at the range 1270 – 1480 cm^{-1} overlayed with the pH curve. The black liquor carbonation displayed similar behavior to the standard NaOH solutions, especially within the concentration range of 3 – 4 wt%. The contour in Figure 3.4B exhibited a smooth transition between the band of CO_3^{2-} and those of HCO_3^-. This is likely due to the use of a stirred reactor which allowed for better distribution of the gas phase and homogenization of the solution. In contrast,

the local gradients caused by the gas bubbles in the 3D printed reactor could be a source of artifacts reflected as irregularities in Figure 3.1B.

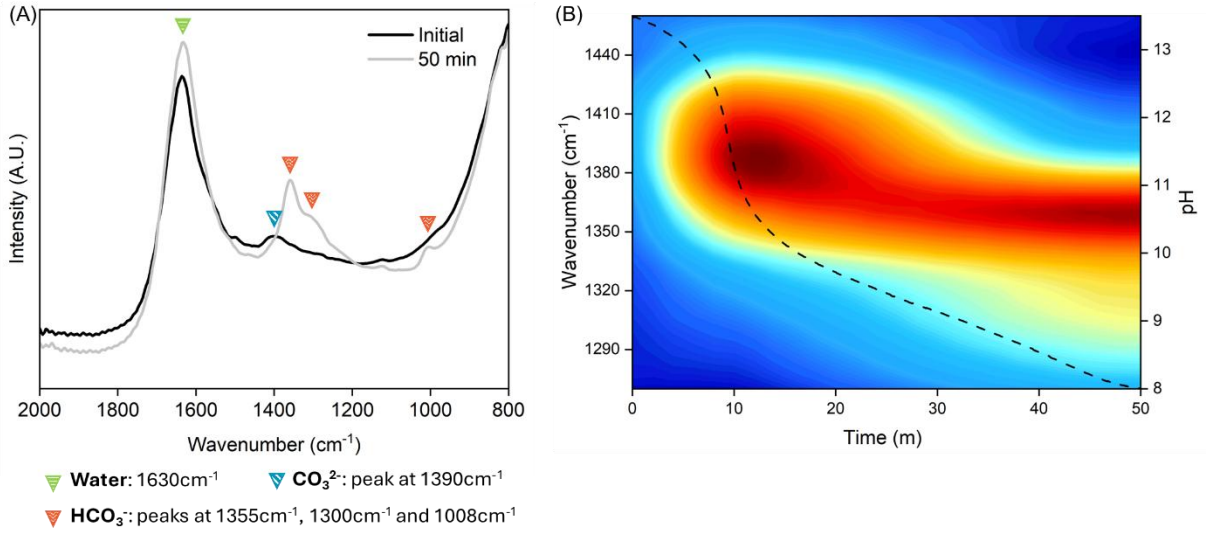

Figure 3.4. *(A) Isolated FTIR spectra of black liquor before and after carbonation and (B) Contour plot of the FTIR spectra overtime at 1270 – 1480 cm^{-1} overlayed with the pH curve.*

CO_2 uptake

The concentration of alkali in solution has a direct effect both on the CO_2 uptake capacity and the rate of absorption. The cumulative mass of absorbed CO_2 over time, expressed in g of CO_2/ L of solution, is presented in Figure 3.5 for NaOH concentrations of 1, 4, and 8 wt%. At the lowest NaOH concentration the absorption rate displayed a near-linear trend throughout the experiment, reaching a final CO_2 uptake of 9.5 g/L after 4.3 minutes. In the 4 wt% NaOH solution, three distinct absorption regimes with progressively decreasing rates were observed, as discussed previously, resulting in a total CO_2 uptake of 41.7 g/L after 61 min. For the highest NaOH concentration, an initial regime lasting approximately 27 min was identified, during which nearly 48 g/L of CO_2 was absorbed. Beyond this period, only an additional 31 g/L was captured over the remaining 120 min of the experiment. Notably, the maximum absorption achieved in the 4 wt% solution after 61 min was attained in approximately one-third of that time in the 8 wt% solution.

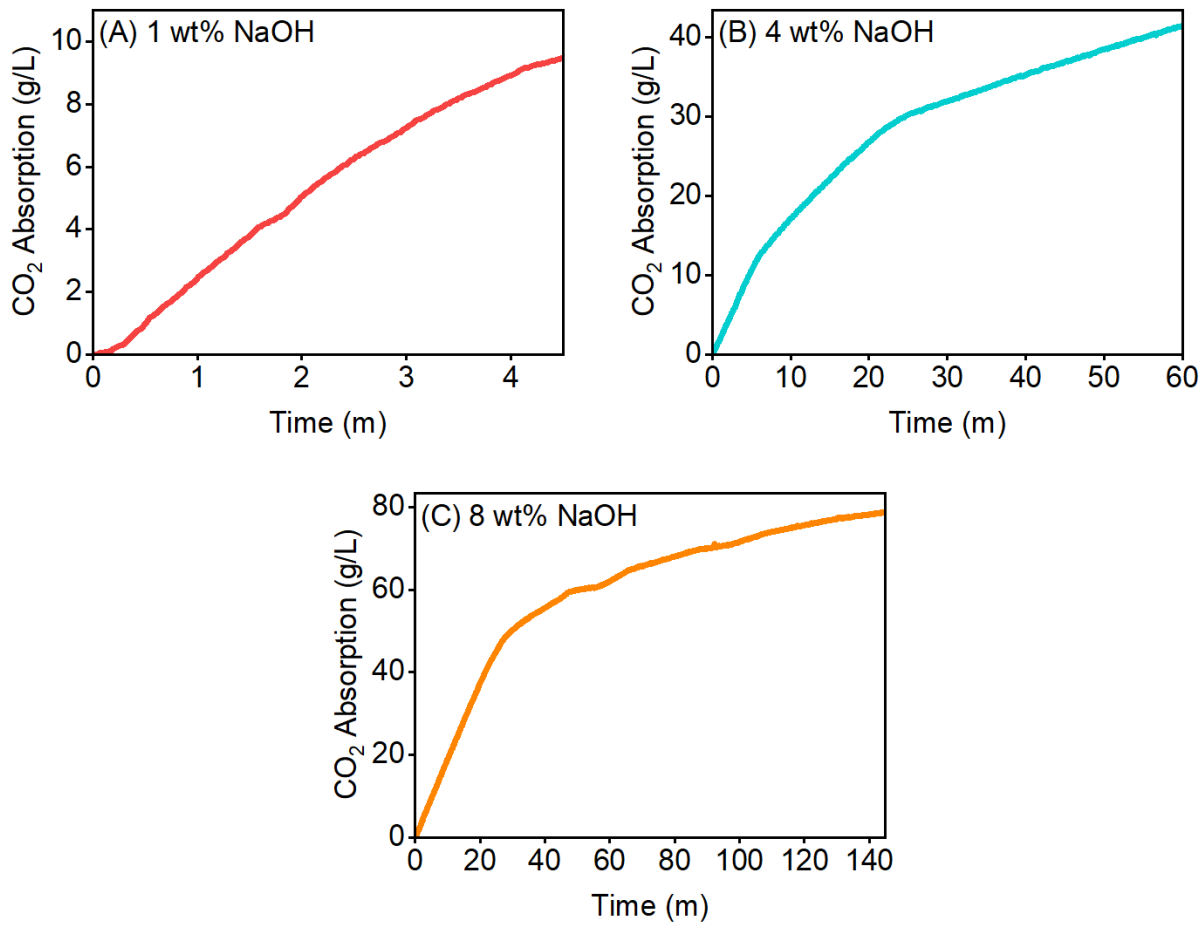

Figure 3.5. *CO_2 absorption with time for 1, 4 and 8 wt% aqueous NaOH solutions.*

The absorption capacity of the NaOH solutions was compared with the stoichiometric amount of CO2 corresponding to complete conversion into either CO_3^{2-} or HCO_3^-, as shown in Figure 3.6A. For all NaOH concentrations, the measured absorption capacities were close to the theoretical values assuming full conversion to HCO_3^-. This indicates that HCO_3^- was the dominant reaction product in all experiments. As illustrated in Figure 3.6B, the absorption capacity increased linearly with increasing NaOH concentration. These findings are consistent with previously reported literature values [22], thereby supporting the reliability of the experimental setup. The CO_2 absorption capacity of black liquor was 30.8 ±1.8 g/L. This is projected in Figure 3.6B. The NaOH solution used in soda pulping to produce the black liquor was 4 wt%, but as a small portion of this was consumed in the cooking process the remaining liquor had a carbon capture potential closer to that of the standard 3 wt% aqueous NaOH solution. Of course, the projected strength of the black liquor as a CO_2 absorbent can be tuned by removing or adding water to alter the NaOH concentration.

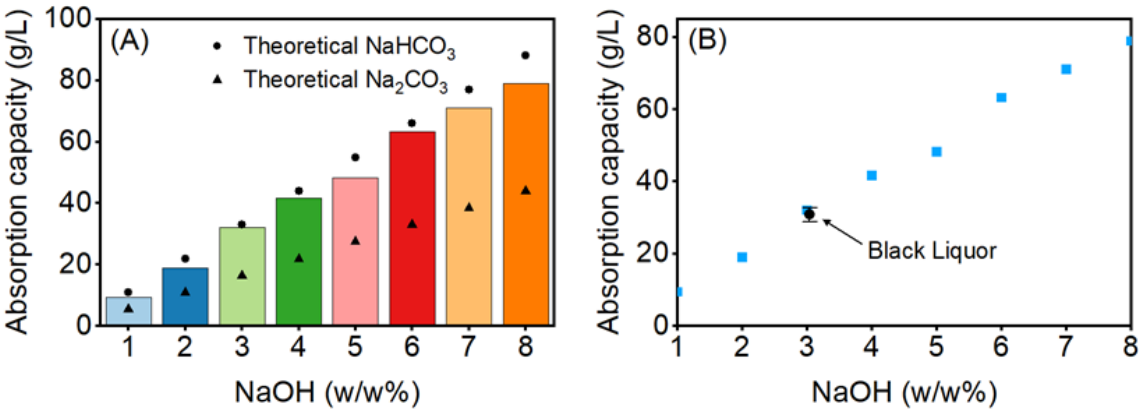

Figure 3.6. *(A) Obtained and theoretical absorption capacities for NaOH solutions of 1 to 8 wt% NaOH. (B) Absorption capacity of the NaOH solutions (blue points) and of the black liquor (black point).*

Physicochemical characterization of products

Solids products of the carbonation reactions were prepared and analyzed with XRD and SEM. To obtain reference morphological and structural information of the Na_2CO_3 and $NaHCO_3$ prepared under the experimental conditions of this study precipitated carbonates were collected from the 6 wt% NaOH carbonation experiment and dried prior to analysis. The carbonated black liquor required further treatment. As mentioned in Chapter 1, the acidification of black liquor leads to precipitation of lignin and silica. At the pH 8 which was reached in the carbonation experiments all the silica present in the black liquor, and some lignin had precipitated. The carbonated black liquor was filtered, and the filtrate and residue were collected and dried separately. Figure 3.7 shows the XRD diffractograms of these three samples. The solids from the 6 wt% NaOH experiment showcased a pattern that strongly matched that of natrite (Na_2CO_3) as identified by the Crystallography Open Database and literature on $NaHCO_3$/Na_2CO_3 crystal phases [109,110]. As can be seen in Figure 3.7A and B, the filtrate solids of black liquor showcased a very similar XRD pattern, while the residue solids (Figure 3.7C) presented a pattern that matches more that of $Na_2CO_3 \cdot H_2O$, as well as a broad band between 18 and 29 ° which can be attributed to amorphous lignin and silica [57]. There was no significant indication of the presence of $NaHCO_3$ in any of the XRD diffractograms, although this was the primary species at the end of each carbonation experiment. This can be attributed to the drying process, during which the $NaHCO_3$ decomposed to Na_2CO_3.

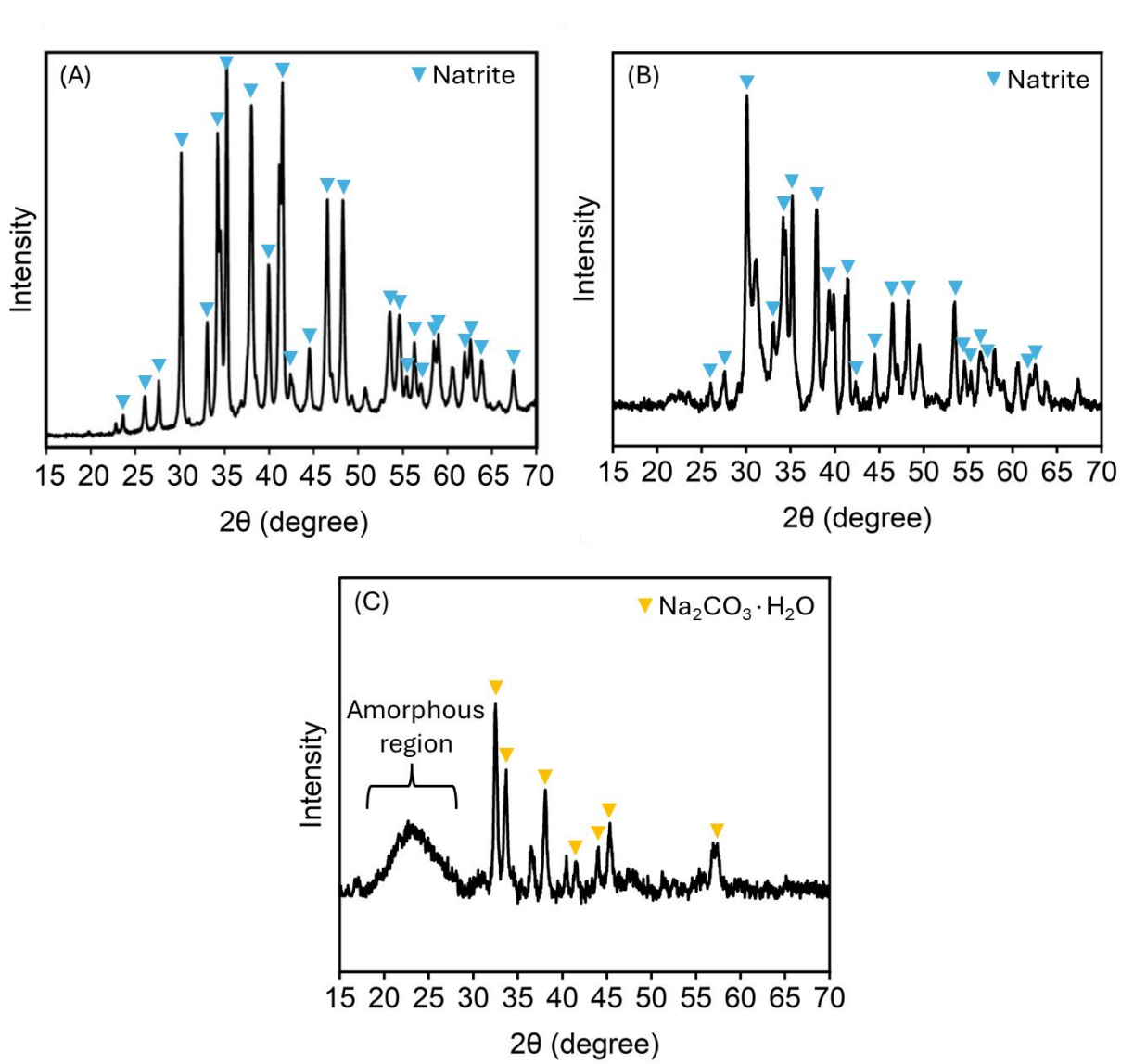

Figure 3.7. *XRD diffractograms of (A) the precipitated salt collected from the carbonation of 6 wt% NaOH, (B) the dried solids of the black liquor filtrate separated by filtration after carbonation and (C) the dried solids of the black liquor residue separated by filtration after carbonation.*

The morphology of the same samples is displayed in Figure 3.8. Figure 3.8A and B show SEM images of the solids from 6 wt% NaOH carbonation, recognized as natrite with XRD. The filtrate solids of black liquor were observed both with SEM (Figure 3.8C and E) and optical microscopy (Figure 3.8D), and particles of the same morphology were identified with both techniques.

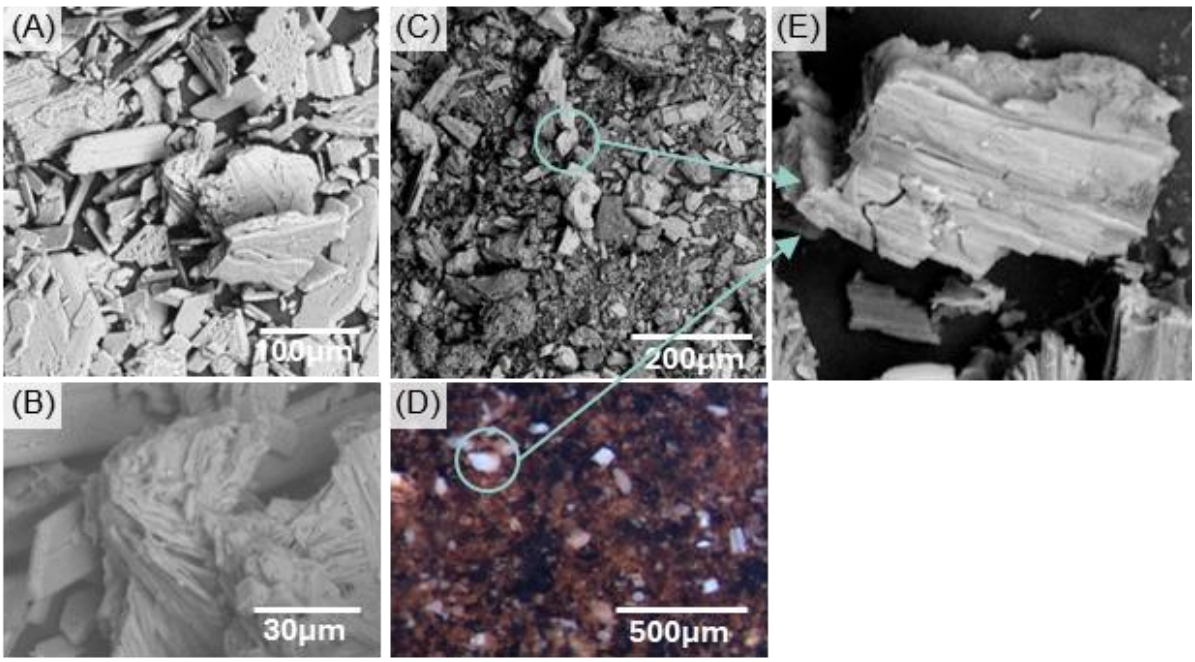

Figure 3.8. *(A) and (B) SEM images of the precipitated salt collected from the carbonation of 6 wt% NaOH, (C) SEM image of the dried solids of the black liquor filtrate separated by filtration after carbonation, (D) optical microscopy image of the dried solids of the black liquor filtrate separated by filtration after carbonation, and (E) zoomed in SEM image of a particle from image (C).*

The NMR spectra of black liquor before and after carbonation shown in Figure 3.9 reveal a chemically complex mixture. Peaks associated with the aromatic structures of lignin are expected in the region between 100 and 120 ppm, while methoxy groups typically appear around 50 ppm. Signal observed between 50 and 100 ppm is most likely attributable to hemicellulosic components. Nevertheless, the NMR spectra of the non-carbonated and carbonated black liquor (Figure 3.9A and B) exhibited negligible lignin-related signals, which may be attributed to the low lignin content in the sample. The resonance at 168 ppm is assigned to CO_3^{2-}, confirming the presence of a small amount of CO_3^{2-} prior to carbonation, in agreement with the FTIR results. Following carbonation to pH 8, no substantial changes in the composition of organic species were observed (Figure 3.9B) In contrast, the CO_3^{2-} signal disappeared and was replaced by a more intense resonance at 161 ppm, corresponding to HCO_3^-. This spectral shift confirms that HCO_3^- was the predominant species at the end of the experiments.

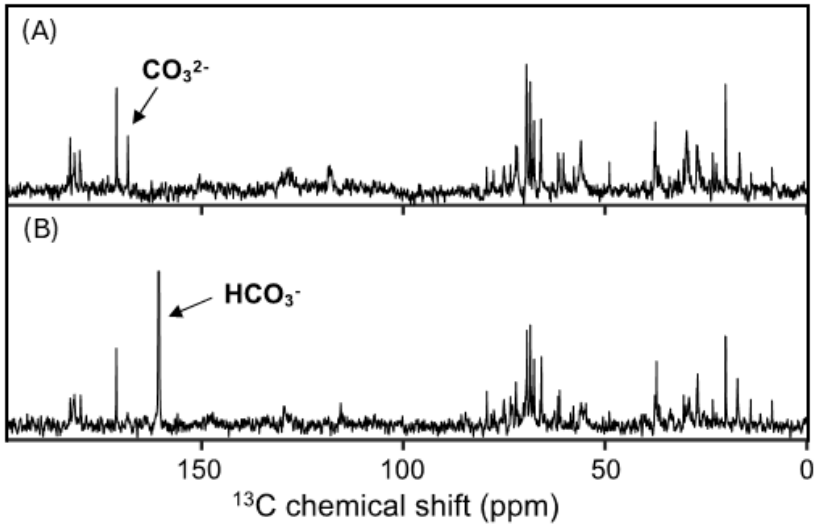

Figure 3.9. *Liquid state ^{13}C NMR spectra of black liquor (A) before and (B) after carbonation.*

Summary

CO_2 absorption with aqueous NaOH was studied with two different absorbent systems and under different experimental setups. Aqueous solutions of NaOH in the range of 1 – 8 wt% were used as a reference system to evaluate the performance of the 3D printed bubble column reactor designed here, and the carbonation process was followed with in-line measurements of pH, FTIR and gravimetric measurements of the CO_2 uptake. Time resolved FTIR spectra was useful in following the equilibrium between the Na_2CO_3/$NaHCO_3$ species and associating that with the pH and the absorption rate throughout each experiment. Subsequently, black liquor prepared from soda pulping of oat husks was also investigated as a CO_2 absorbent. Owing to the intense foaming of black liquor, a stirred tank reactor was used instead of the 3D printed one. The liquor used in soda pulping was a 4 wt% aqueous NaOH solution. However, after the pulping process the produced black liquor presented a small FTIR peak of Na_2CO_3, and the CO_2 uptake capacity was 30.8 ±1.8 g/L, which was closer to that of the 3 wt% aqueous NaOH solution. During the carbonation of black liquor, the decrease in pH causes the precipitation of silica and some lignin. The precipitates and the liquid were separated by filtration, dried and analyzed with XRD and SEM. Solids from the carbonation of NaOH were also analyzed and served as reference to study the structure of carbonates formed under these experimental conditions. Natrite was the main product found in both the standard NaOH experiments and the black liquor, as identified by XRD. A broad band at low 2θ was attributed to the amorphous precipitated silica and lignin. Liquid state NMR of the black liquor before and after carbonation confirmed the FTIR spectra showing that the end product at pH 8 is $NaHCO_3$, suggesting that natrite was formed by decomposition of the $NaHCO_3$ when drying the samples for analysis.

Chapter 4: Aqueous carbonation with Ca and Mg-containing industrial side-streams

Based on **Papers III, IV and V**

Overview

In this chapter two alkaline industrial side streams will be investigated for CO_2 capture, steel slags and GLD. Three steel slags, TK, EAF and LF slag, with the commercial names Petrit T, Petrit E and Petrit L were provided from Höganäs. GLD and an alkaline wastewater were provided by SCA. Aqueous slurries were prepared and direct aqueous carbonation was performed. The effect of S/L ratio, temperature, particle size and stirring time prior to carbonation were explored. GLD was mixed with both deionized and wastewater to examine the potential of valorizing an industrial wastewater instead of consuming fresh water. The study of S/L ratio was conducted in the 3D printed reactor, with the pH meter following the pH of the slurries. The other studies were conducted in a stirred reactor in a water bath.

Particle characteristics of the samples used

Table 4.1 and Table 4.2 summarize the particle size distributions of the materials used, determined by ImageJ analysis of SEM micrographs. Petrit T was provided as a powder and was thus used as is in all experiments. In contrast, Petrit L and Petrit E exhibited larger particle sizes. For the S/L ratio investigation particles with diameter below approximately 1 mm were selected (Table 4.1). For all other studies the samples were crushed and classified into coarse and fine fractions (Table 4.2). The fine fractions of Petrit E and Petrit L were used in all subsequent experiments, while the coarse fractions were employed to assess the effect of particle size. GLD is a relatively soft material and was used as received in all experiments. It was also crushed to study the effect of particle size.

Table 4.1. *Particle size of the steel slags and GLD used in the S/L ratio study*

Size (μm)	Petrit T	Petrit E	Petrit L	GLD
Mean	7.1	250.1	131.6	110.0
Max	63.1	1384.7	927.0	450.0
Min	0.7	5.6	16.8	24.0

Table 4.2. *Particle sizes of the steel slags and GLD used in the particle size study. In all other studies GLD were used as is (big particles). For the Petrit E and L, the effect of temperature and stirring time were studied using the small particles.*

Size (µm)	**Petrit T**	**Petrit E**		**Petrit L**		**GLD**	
		fine	coarse	fine	coarse	fine	coarse
Mean	7.1	28.0	600.0	16.0	800.0	3.6	110.0
Max	63.1	100.0	1130.0	99.0	1540.0	130	450.0
Min	0.7	0.3	160.0	0.5	110.0	0.1	24.0

The N_2 physisorption isotherms and BET surface areas of the three steel slags are presented in Figure 4.1. All materials exhibited type II isotherms with H3-type hysteresis loops, according to the 2025 IUPAC classification [111]. Type II isotherms are characteristic of nonporous or macroporous materials. The presence of H3 hysteresis may indicate either plate-like particle morphologies or the existence of macropores that are not completely filled with pore condensate. Petrit E exhibited the lowest BET surface area (2.8 m^2/g), whereas GLD showed the highest values, both in the fine and coarse states (35.9 and 34.6 m^2/g, respectively). Of the three steel slags Petrit T had the highest surface area, followed by Petrit L.

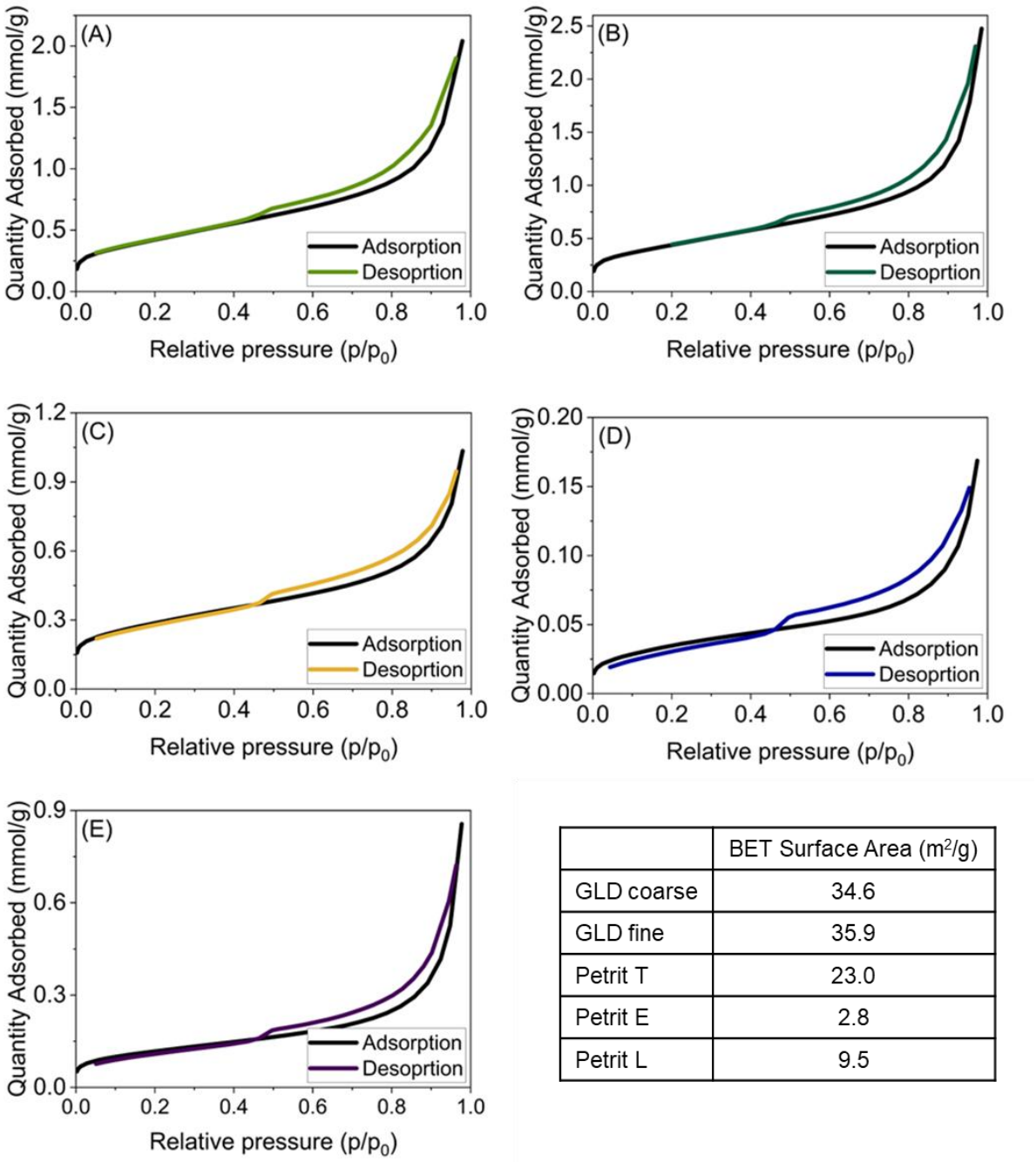

	BET Surface Area (m^2/g)
GLD coarse	34.6
GLD fine	35.9
Petrit T	23.0
Petrit E	2.8
Petrit L	9.5

Figure 4.1. *Physisorption isotherms and BET surface areas of (A) GLD coarse, (B) GLD fine, (C) Petrit T, (D) Petrit E and (E) Petrit L.*

Following the carbonation process

The carbonation process was followed with a pH meter and a CO_2 sensor connected to the outlet of the reactor. Figure 4.2 shows the outlet CO_2 concentration, CO_2 absorption (in g/L) and pH throughout time for each of the investigated materials at S/L ratio of 50. Petrit T exhibited the best performance in terms of absorption capacity and duration of the carbonation. The experiment lasted 60 minutes and resulted in around 10.7 g/L of absorbed CO_2. Petrit L has the highest CO_2 absorption of about 13.2 g/L but took more than 7 hours to reach this value. Within the first 1 hour 7.1 g/L of CO_2 had been absorbed and the pH was 7.29. After this the pH kept slightly increasing and the outlet CO_2 was very slowly rising to meet the inlet CO_2 concentration. Petrit E displayed a similar behavior. The CO_2 absorption reached 5.8 g/L within the first 50 minutes and then significantly slowed down until the outlet CO_2 concentration matched the inlet after another 60 minutes. During this second half the CO_2 uptake increased by only 1 g/L to reach a total of about 6.8 g/L. GLD had a trend closer to Petrit T, but its CO_2 uptake was a bit more than half that of Petrit T in the same amount of time. Since both Petrit L and Petrit E appeared to have a turning point at 14% of CO_2 outlet concentration, it was decided for the steel slags to carry out experiments up to 14% of CO_2 outlet concentration for the rest of the experiments for the effect of S/L ratio, as at higher S/L ratios the duration of carbonation was higher. For all experiments with S/L ratio of 50 the experiment ended when the outlet CO_2 concentration reached the inlet one.

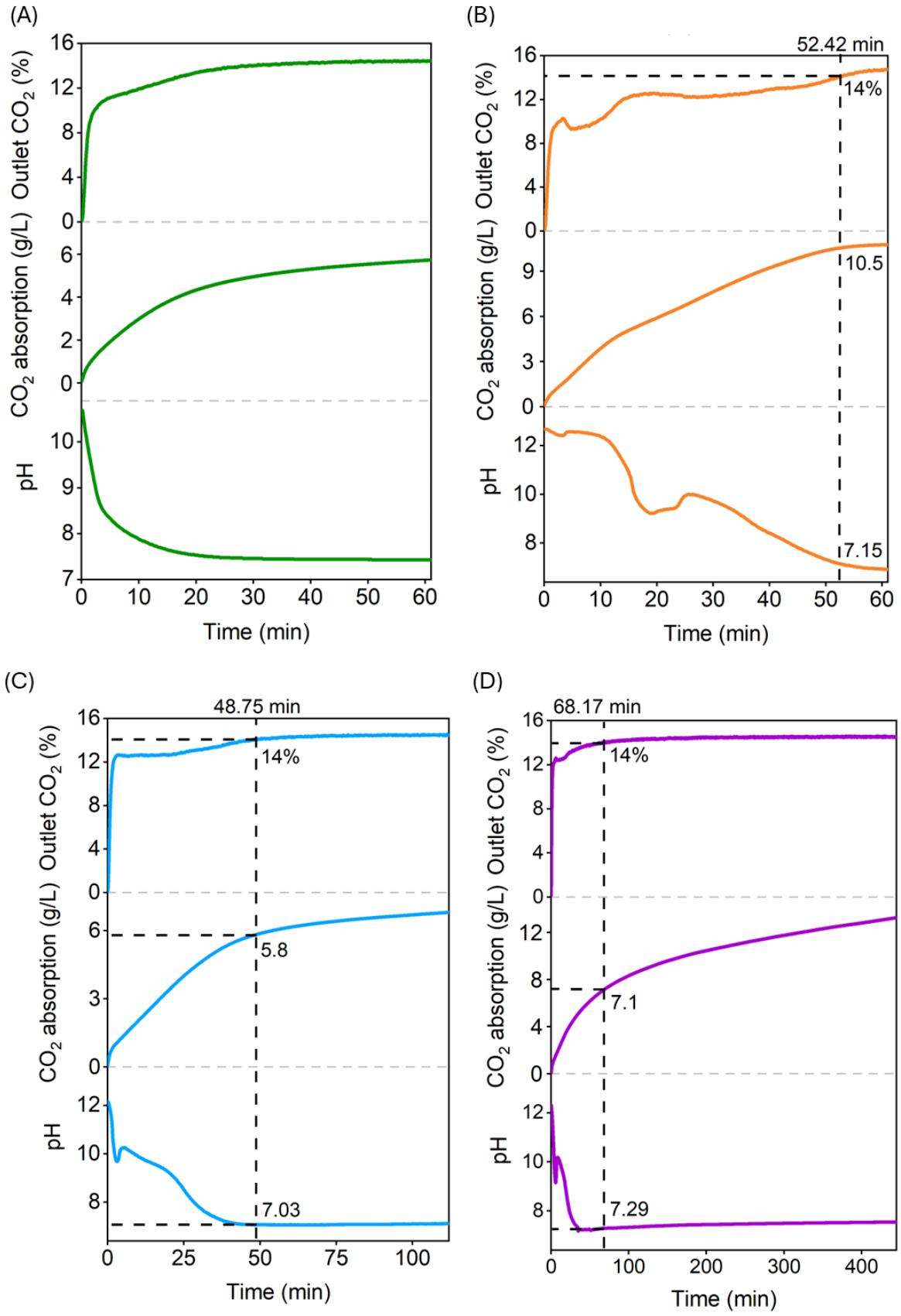

Figure 4.2. *Graphs of CO_2 outlet, absorption and pH with time for (A) GLD, (B) Petrit T, (C) Petrit E and (D) Petrit L at S/L ratio of 50.*

The pH graphs in Figure 4.2 also contain information on the progression of the carbonation process. GLD showed an exponential decrease in pH as the Ca^{2+} was consumed, suggesting that the primary reactive phase was $Ca(OH)_2$ and other Ca phases in the material were insignificant. The steel slags displayed a more complex profile with irregular pH trends. Additionally, the distortions in pH were reflected in the CO_2 outlet concentration, which displayed a drop whenever the pH presented a small spike. These irregularities can be attributed to the dissolution of different Ca and Mg-containing phases throughout the experiments.

Factors affecting the carbonation process

Effect of S/L ratio

Figure 4.3 shows the absorption capacity (g of CO_2 / L of slurry), and the yield of carbonation expressed as g of CO_2/ kg of material. The S/L ratio exhibited a positive correlation with the CO_2 uptake of the slurry. In other words, slurries with higher amount of solid achieved higher CO_2 uptake, which is expected, due to the increased amount of reagent present. In contrast, the carbonation yield followed the opposite trend. Lower S/L ratio enhanced the carbonation degree. This phenomenon can be conceptually interpreted by discussing the reaction mechanism throughout the carbonation process. The following discussion is derived from two theoretical kinetic models, the two film theory model and the shrinking-core model. Both have been employed in the literature to describe the mechanism of direct aqueous carbonation [112–115].

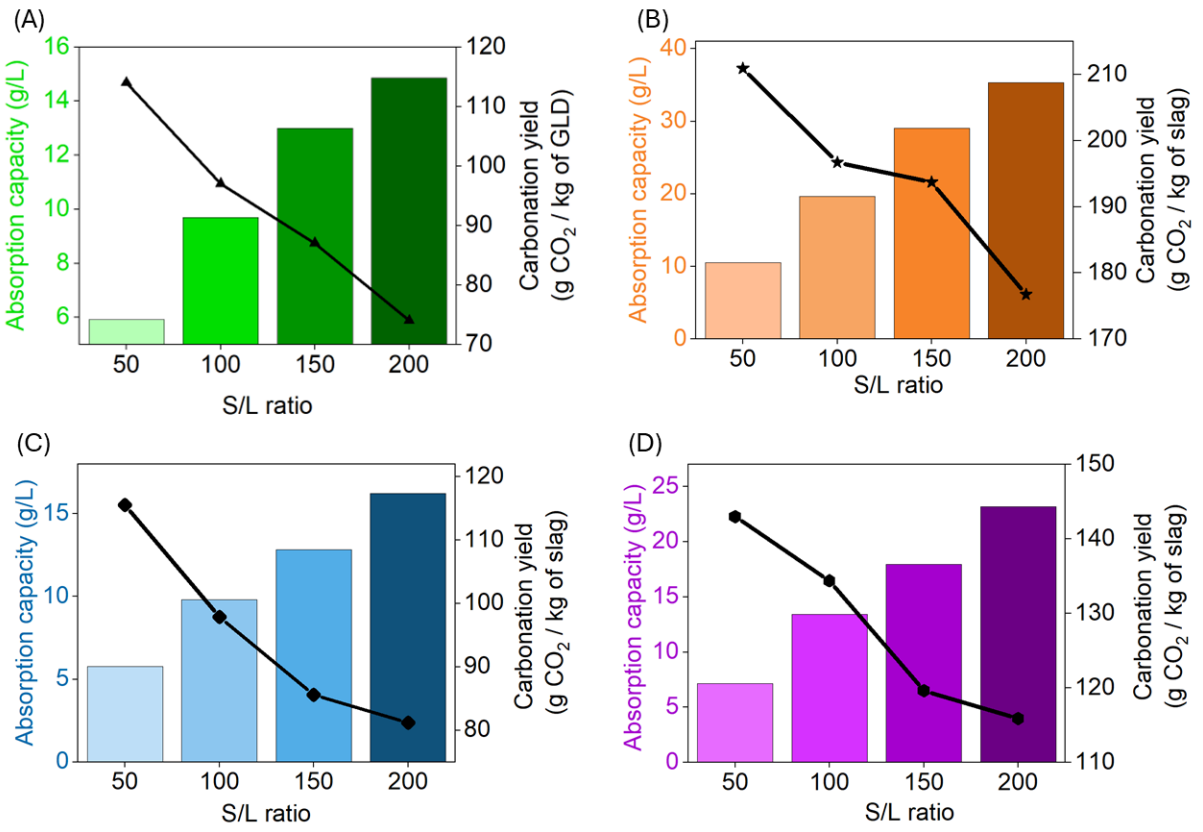

Figure 4.3. *Absorption capacities (left y axis) and carbonation yield (right y axis) of (A) GLD, (B) Petrit T, (C) Petrit E and(D) Petrit L for a range of S/L ratios.*

Direct aqueous carbonation is a heterogeneous system containing a gaseous, liquid and solid phase. Two film barriers are present, the gas-liquid film, through which mass transport of CO_2 takes place and the solid-liquid film, where Ca^{2+} and Mg^{2+} cross to the bulk liquid. At the initial phase of carbonation there is a high amount of M^{2+} and OH^- ions in the bulk liquid phase. Thus, the CO_2 reacts towards the formation of MCO_3 in the liquid phase and the products precipitate out of the solution. The consumption of the reactants promotes the dissolution of more reactive ions from the solid phase. Thus, at this stage, the mass transport of CO_2 is a significant factor. As the reaction progresses the availability of reactive ions from the solid decreases. The amount of readily soluble compounds (such as $Ca(OH)_2$) is reduced, leaving Ca-containing compounds to provide the reactive ions, which dissolve at a slower rate. Thus, instead of the CO_3^{2-} and Ca^{2+} coming in contact near the gas-liquid interphase, the reaction location shifts closer to the liquid-solid interphase. There, as the shrinking core model describes, the carbonate products can be deposited on the Ca-containing particles, thus creating a passive layer of product (known as the ash layer). This inhibits aqueous CO_3^{2-} from reaching the unreacted core of the particles, as well as unreacted Ca from dissolving in the liquid phase. This is the second stage of the process, in which the absorption mechanism is determined by the diffusion of ions through the liquid-solid layer. When $CaCO_3$ nucleates at the surface of solid particles covering the active sites

the carbonation process comes to a halt, leaving unreacted reagent at the core of the particles. At higher solid content (higher S/L ratio), even though there is a higher quantity of Ca-containing compounds, their availability is still limited by the rate of dissolution. Thus, the lower degree of carbonation can be attributed to the formation of a passive product layer before all the available Ca is able to leach to the liquid phase.

Effect of temperature

Figure 4.4 compares the CO_2 uptake of GLD and Petrit T, E and L at two different temperatures. In all cases, increasing temperature resulted in a lower extent of carbonation. For GLD, the carbonation yield decreased from 84.3 g/kg at 25 °C to 22.7 g/kg at 60 °C, corresponding to a reduction by a factor of approximately 3.5. A similar trend was observed for the steel slags: at 60 °C, CO_2 uptake was 106.5 g/kg for Petrit T, 101 g/kg for Petrit E, and 119.5 g/kg for Petrit L, whereas at 25 °C the respective values were higher, at 171.9 g/kg, 186.8 g/kg, and 162.9 g/kg. This temperature-dependent decline in carbonation efficiency is consistent with the reduced solubility of both CO_2 and $Ca(OH)_2$ at elevated temperatures, as described by the relationship given in equation [19,20]:

$$Ca(OH)_2 \text{ solubility (g/kg of solution)} = -0.0108\ T\ (^oC) + 1.7465 \quad (4.1)$$

Most studies on direct aqueous carbonation of steel slags reported a positive relationship between temperature and carbonation yield in the range of 20 – 60 °C, in contrast to our findings [114,116,117]. However, Bonfante et a. conducted a design of experiment study on the accelerated carbonation of EAF slag at a liquid-to-solid ratio of 3 L / kg (S/L = 333), with 100% CO_2 flow and similarly observed a decline in carbonation efficiency with increasing temperature. This work identified 33 °C as the optimal temperature, according to their generated regression model [118]. These findings suggest that carbonation performance is governed by coupled effects of the S/L ratio, CO_2 inlet concentration and temperature, rather by the individual parameters. Under the conditions employed in the present work, the relatively low CO2 concentration of 15% amplifies the effect of gas dissolution in the liquid phase. Aqueous solubility of calcium silicates increases with temperature [43,44]. Thus, at higher CO_2 concentrations increased temperature can have a positive effect on carbonation by enhancing the availability of Ca^{2+} from silicate phases. In contrast, at low CO_2 inlet concentration and low S/L ratio, the solubility of CO_2 is the determining factor for the carbonation performance.

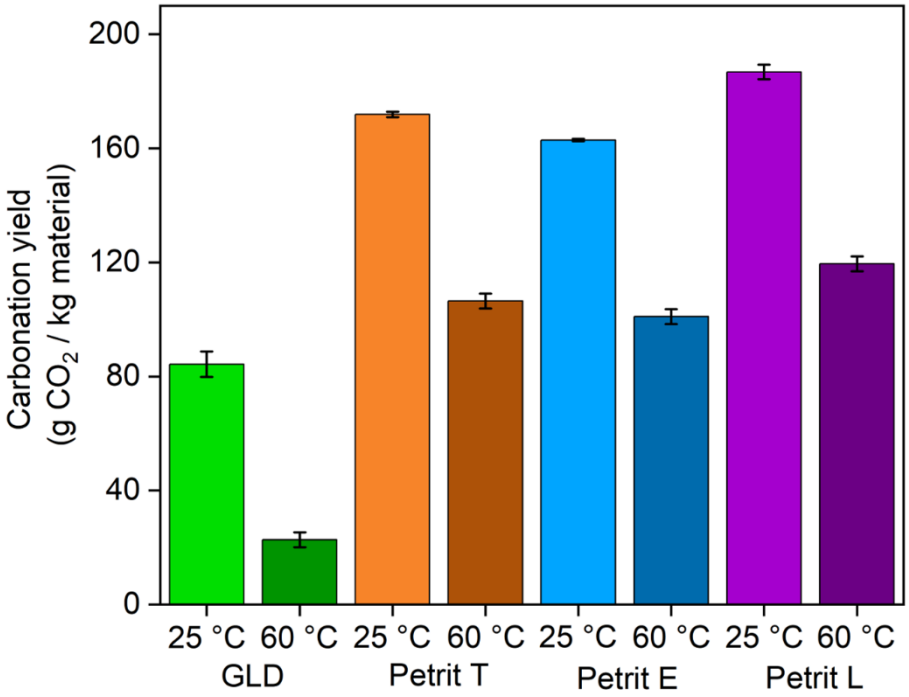

Figure 4.4. *Carbonation yield of the materials investigated at temperatures 25 and 60 ℃.*

Effect of particle size

Figure 4.5 displays the carbonation yield for GLD, Petrit E and Petrit L at two different particle sizes. All three materials exhibited a consistent trend of reduced performance at higher particle size. This is an expected behavior, as decreasing the particle size increases the total surface area, thus exposing more reactive Ca-bearing phases. For GLD this difference was not as prominent, as the carbonation extent increased from 84.3 g/kg to 89.6 g/kg after crushing the material. As presented in Figure 4.1, GLD have the highest porosity of all materials and the surface area was marginally affected by crushing, explaining the small effect in performance. Petrit E, which had the lowest surface area, also showed the most prominent effect of particle size in the carbonation degree, with the fine sample yielding 162.9 g/kg in contrast to 58.2 g/kg for the coarse particles. In the case of Petrit L, the performance dropped from 186.8 g/kg for the fine particles to 124.2 g/kg for the coarse ones. These observations fall in line with the results of the BET surface area. However, it should also be noted that the stirring pretreatment of the slurries also affects the particle size in different extends, owing to the differences in hardness between the materials.

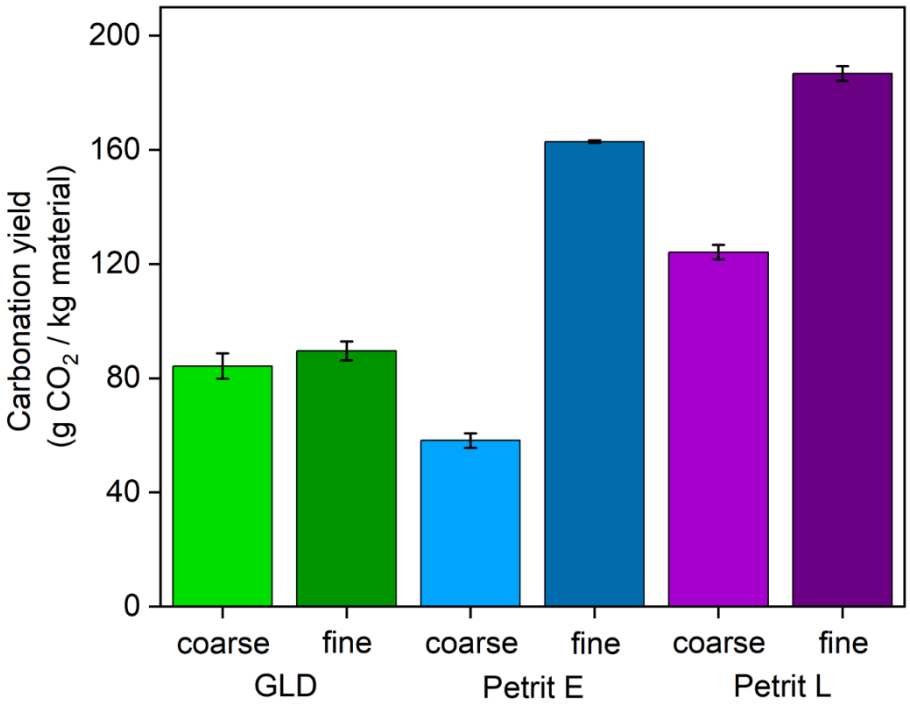

Figure 4.5. *Degree of carbonation for two different particle sizes of the investigated materials.*

Effect of stirring time

Prior to all experiments, the slurries were stirred for 24 h. To investigate the effect of this stirring pretreatment on carbonation, additional experiments were conducted in which the slurries were stirred for 2, 4, and 24 h before carbonation. Furthermore, separate experiments were performed in which the slurries were stirred for a defined period, followed by filtration and carbonation of the resulting filtrate. These experiments were designed to examine the leaching behavior of Ca^{2+} and Mg^{2+} during the stirring period and to decouple this effect from the influence of stirring on the slurry itself. The results of all experiments are illustrated in Figure 4.6. The filtrate solutions displayed a constant CO_2 absorption capacity for 2, 4 and 24 hours of stirring as seen by the bars with diagonal line fill. This suggests that within 2 hours the water is saturated with the dissolved metal ions and further stirring beyond that does not result in more leaching. In contrast to the filtrate solutions, the carbonation of the slurries showed an upward trend with the increase in stirring time. The effect of the stirring time was least prominent for the GLD. The CO_2 absorption in the reactor went from 0.24 g in 2 h to 0.27 in 4 h and 0.29 after 24 h. The highest impact was in Petrit E, which absorbed 0.22, 0.26 and 0.49 g of CO_2 after stirring for 2, 4 and 24 h respectively. Petrit L had a similar trend, with absorptions of 0.24 and 0.36 in the first 2 and 4 h, reaching up to 0.56 g after 24 h of stirring. Petrit T had an initial higher absorption increase, from 0.44 g after 2 h stirring to 0.59 g after 4 h and a smaller increase to 0.65 g after 24 h.

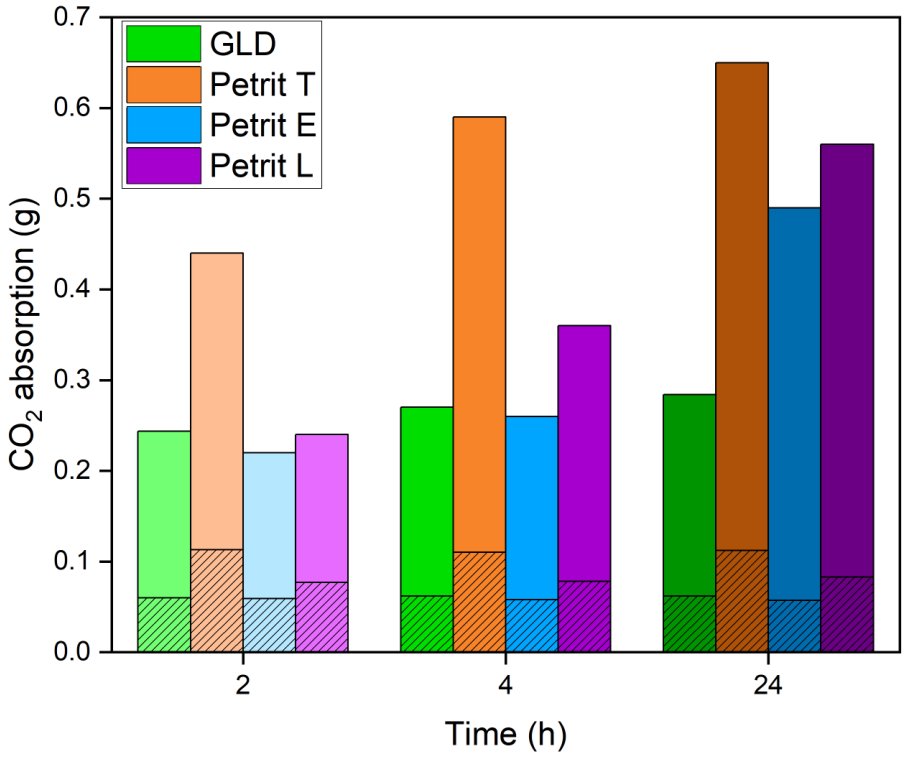

Figure 4.6. *CO_2 absorption in the reactor for each material at three different stirring times (2, 4 and 24 h). The bars with diagonal lines indicate the absorption of the filtrates prepared after stirring and filtering out the solids. The bars without fill indicate the absorption of the slurries.*

Deionized versus wastewater

Wastewater (WW) provided by SCA was investigated in the replacement of deionized water (DW) for GLD carbonation. The utilization of a wastewater stream would be beneficial in minimizing freshwater consumption. WW had an initial pH of 10.44, owing to dissolved Na and K compounds. The absorption of CO_2 in WW was measured to be 2.04 g/L, while, for reference, the absorption of CO_2 due to dissolution in DW was 0.89 g/L. Figure 4.7 shows the absorption capacities of DW, WW, and GLD in DW and WW at two different S/L ratios. The absorption capacity of the mixtures improved with the utilization of WW instead of DW. Interestingly, the mixtures with WW exhibited higher absorption capacity than that of GLD in DW and WW combined. This could be an effect of the pH, as the initial pH of the mixtures in WW was higher and the presence of Na and K CO_3^{2-} and HCO_3^- species could create a buffering effect that keeps the pH elevated for a longer time, thus enhancing the carbonation.

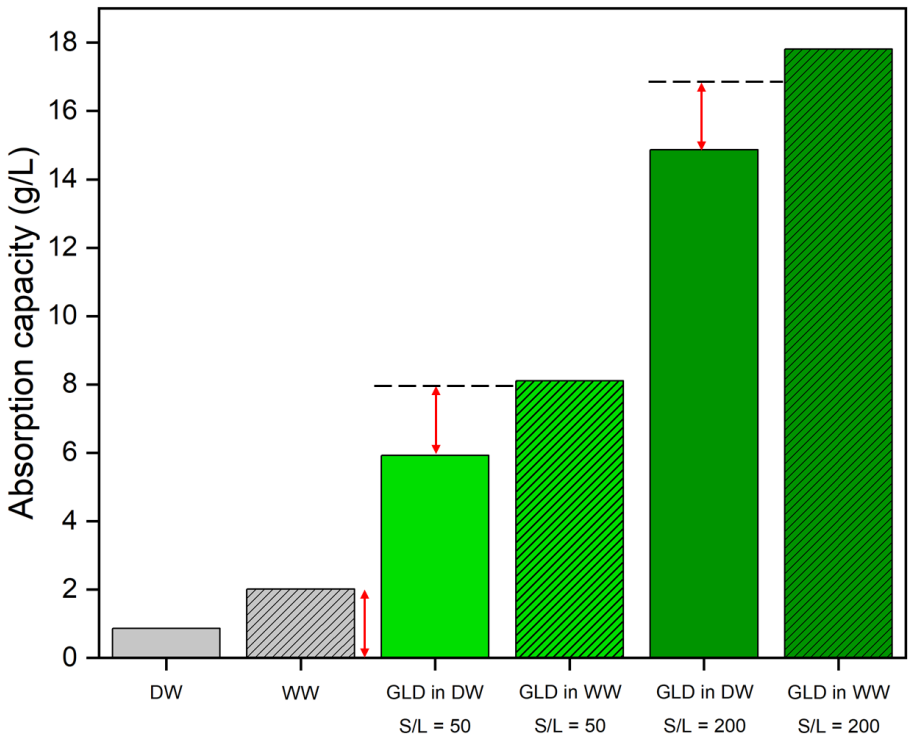

Figure 4.7. *Absorption capacities of deionized water, wastewater and mixtures of GLD in each at 50 and 200 S/L ratio.*

Figure 4.8 shows the FTIR spectra with time for carbonation experiments of WW (A) GLD with WW (B) and GLD with DW (C). The initial pH of the WW was 10.44 and 10.43 for the mixture in WW, while it was slightly lower, at 10.06 in DW. FTIR revealed that CO_3^{2-} was present in WW before the carbonation. The spectra then showed a decrease in the CO_3^{2-} band along with the rise of HCO_3^- bands in all three systems. A band at around 1080 cm^{-1} was also observed. It was present in all mixtures, although it had higher intensity in WW and its mixture with GLD, and it appeared to remain constant throughout the carbonation. This band could be attributed to Na_2SO_4 [119], which is present in the WW and could also exist in GLD as it contains a small concentration of S.

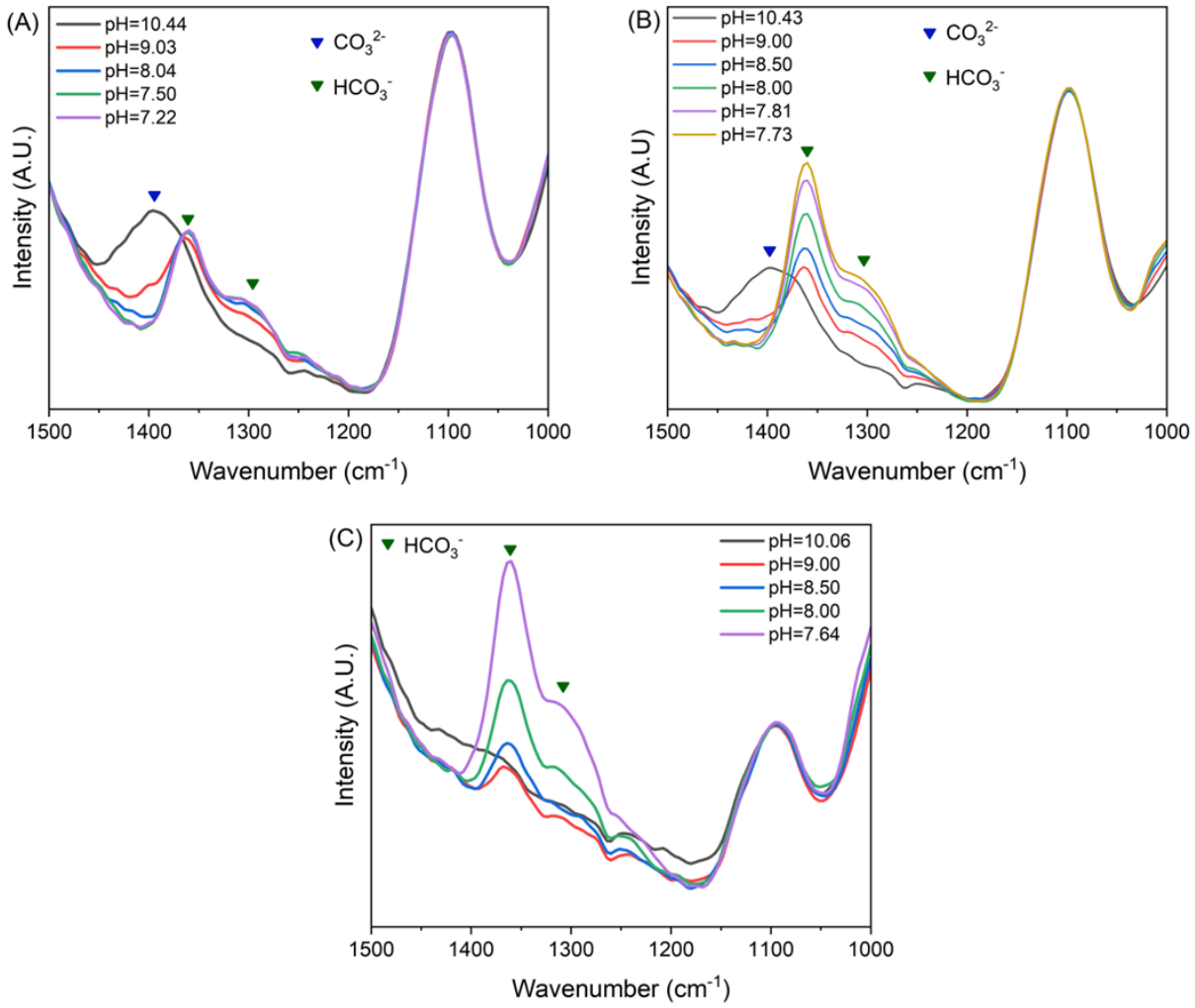

Figure 4.8. *FTIR spectra of (A) WW, (B) GLD in WW and (C) GLD in DW, monitored at varying pH levels during a carbonation experiment.*

Physicochemical characterization

After the carbonation process the slurries were oven dried and the solids were subjected to various analytical techniques to examine the microstructural changes caused by the process and the formation of products. Carbonated samples from both 25 and 60 °C experiments were used to investigate the effect of temperature in the restructuring of mineral phases. $CaCO_3$ – the primary product of the process – can occur in four different phases: calcite, aragonite, vaterite and amorphous $CaCO_3$ (ACC) [120–122]. Calcite is the most stable polymorph and has a characteristic cubic structure. Aragonite is metastable polymorph and it assembles in needle-like structures. Vaterite and ACC are the least stable phases, and the most soluble in water. They usually form as precursors upon which aragonite and calcite nucleate [123]. Vaterite is spherical and ACC forms irregular aggregations.

The three crystalline polymorphs of CaCO3 have characteristic XRD patterns. Figure 4.9 shows the diffractograms of all materials after carbonation at 25 and 60 °C. Patterns characteristic of calcite were the most prominent in all diffractograms. Aragonite patterns were also present in lesser extent in GLD, Petrit E and Petrit L, but not in Petrit T. Literature suggests that Mg^{2+} ions inhibit the nucleation of calcite and promote the formation of aragonite [124,125]. Since Petrit T is the only material with little to no MgO, the presence of aragonite in the other materials can be interpreted as an effect of the Mg2+ ions to the crystal growth of the formed CaCO3. In GLD, calcite and aragonite were the only identified phases in the diffractograms (Figure 4.9A and B). In the steel slags CaCO3 was also the dominant phase observed, but other phases could also be recognized. Petrit T presented patterns of wustite (Figure 4.9C) and small peaks that could be attributed to tricalcium silicate in the diffractogram of the 60 °C carbonated slag (Figure 4.9D). Petrit E had a noticeable peak that can belong to periclase in the 25 C carbonated sample, as seen in Figure 4.9E while at 60 C peaks of wustite were present (Figure 4.9F). Patterns of wustite were also observed in Petrit L and the carbonated sample at 25 C also displayed peaks possibly from the presence of nesquehonite (Figure 4.9G and H). The diffractograms reveal that the aqueous chemical environment might have an effect to the crystal growth of $CaCO_3$, but temperature did not seem to have an influence in the developed polymorphs.

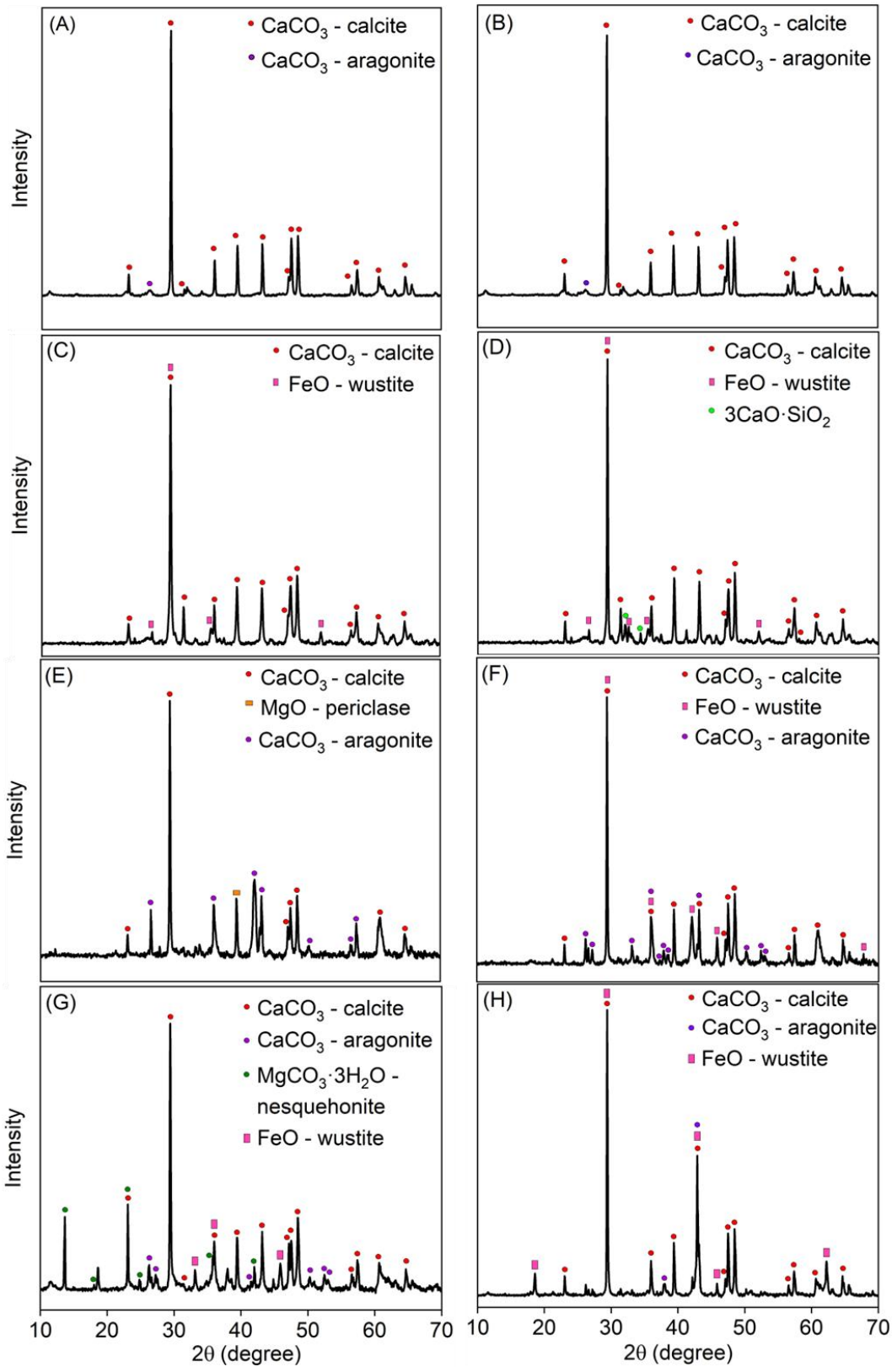

Figure 4.9. *XRD diffractograms of: GLD at (A) 25 °C and (B) 60 °C after carbonation, Petrit T at (C) 25 °C and (D) 60 °C after carbonation, Petrit E at (E) 25 °C and (F) 60 °C after carbonation and Petrit L at (G) 25 °C and (H) 60 °C after carbonation.*

The morphology of the samples before and after carbonation was also observed with SEM imaging coupled with EDS to obtain information on the elemental composition of the observed structures. Figure 4.10 shows the SEM images of GLD before (A) and after carbonation (B). The sample before carbonation contained the characteristic cubic structures of calcite. Floral-shaped structures with Mg content were also encountered. This morphology is characteristic for a type of hydrated $MgCO_3$ known as hydromagnesite ($4MgCO_3{\cdot}Mg(OH)_2{\cdot}4H_2O$) [126,127]. After carbonation hydromagnesite was not detected, but in multiple occasions a crystal growth was observed on the surface of the solids after carbonation (Figure 4.10C). SEM analysis revealed Mg-containing crystals in an assembly typically found in structures of nesquehonite (Figure 4.10D) [126,128]. Cubic calcite structures were also recognized after carbonation.

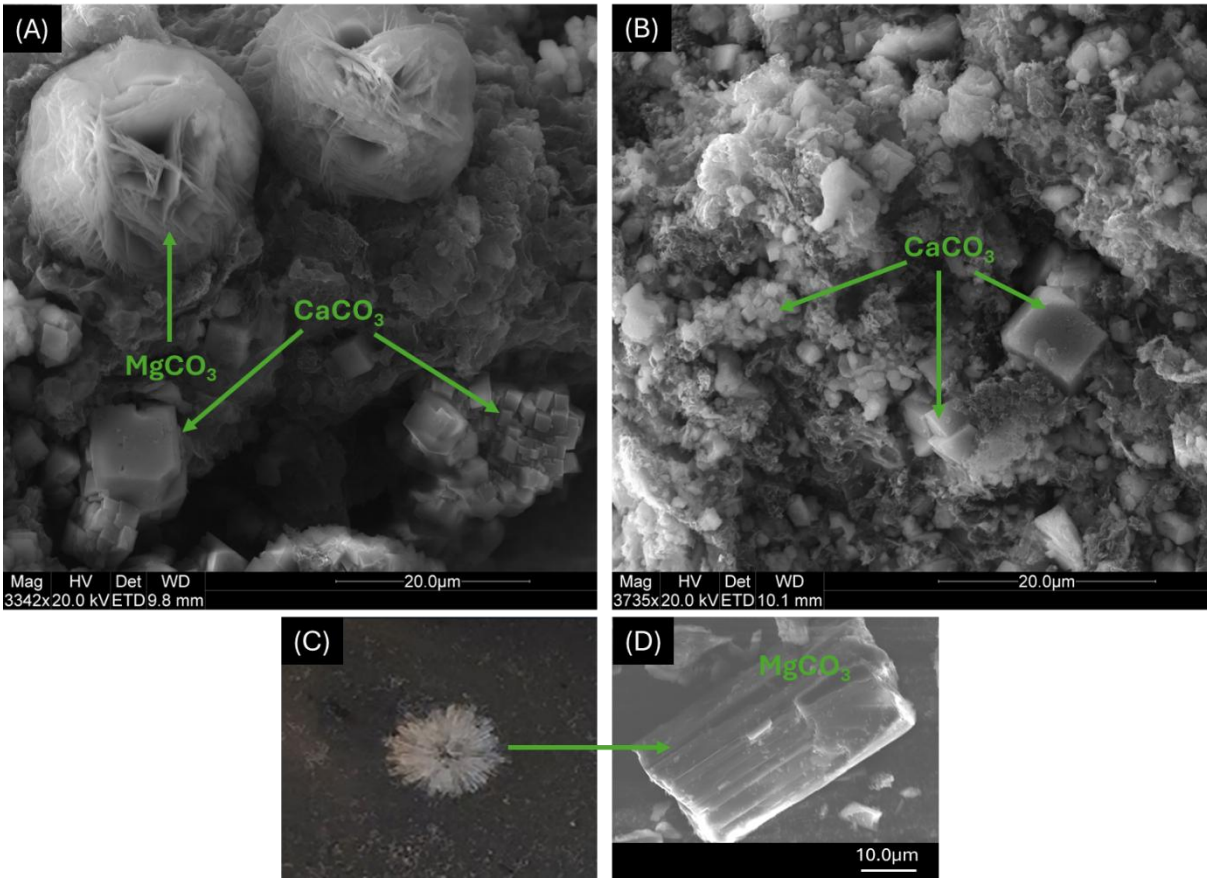

Figure 4.10. *(A) SEM image of GLD before carbonation, (B) SEM image of GLD after carbonation, (C) crystal growth on a GLD sample after carbonation and (D) SEM image of the crystal growth.*

The morphology of the steel slags before carbonation is displayed in Figure 4.11. Petrit T appeared to contain a variety of distinct morphologies (Figure 4.11A). Bright white particles were identified with EDS as Fe-dominated, while dark particles were C-dominated. Spherical particles primarily contained Al and Si. This shape is distinctive for amorphous aluminosilicate structures [129–131]. Other, less distinctive phases were also present with varying elemental compositions. Petrit E and L contained bigger particles in the shape of irregular clusters and with varying elemental composition (Figure 4.11B and C).

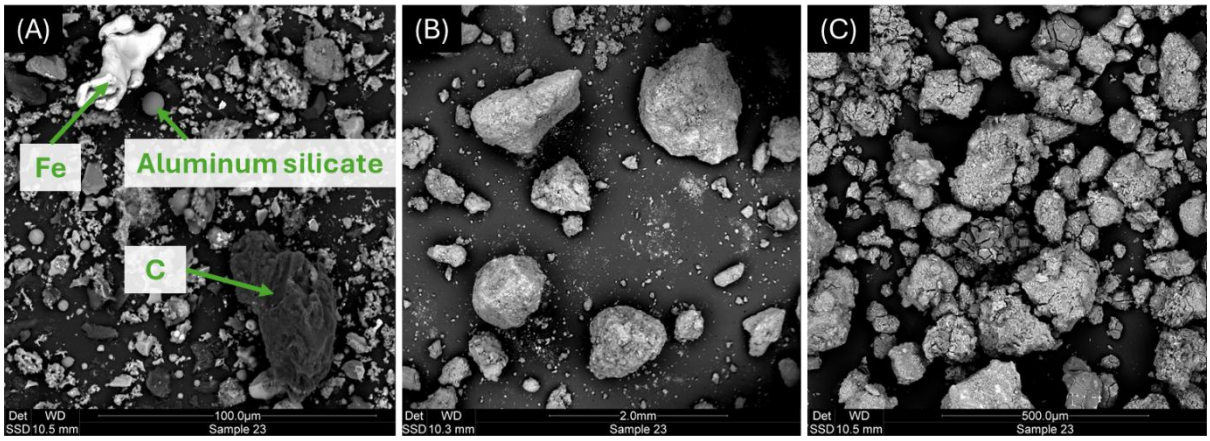

Figure 4.11. *SEM images of (A) Petrit T, (B) Petrit E and (C) Petrit L before carbonation.*

After carbonation $CaCO_3$ structures were present in all three slags (Figure 4.12). Figure 4.12A shows discernible cubic clusters characteristic of calcite nucleated on a Ca-bearing substrate. Multiple such clusters were found in carbonated Petrit T. Petrit E did not display as prominent cubic structures, but near-cubic growths could be observed. Some of these structures are pointed out in Figure 4.12B. Other elements that were detected with EDS in significant percentage (wt%) are also displayed in parenthesis. Possibly, the presence of other elements disturbed the calcite lattices resulting in less regular nucleations. Figure 4.12C depicts the surface of a particle of carbonated Petrit L. The image shows both cubic and irregular structures dominated by Ca, C and O, with other elements such as Si, Al and Fe also detected. These structures appear to have grown on a substrate consisting of a Fe and Mg-dominated phase. In addition to $CaCO_3$, Mg-bearing phases with the characteristic nesquehonite morphology were also recognized (Figure 4.12D).

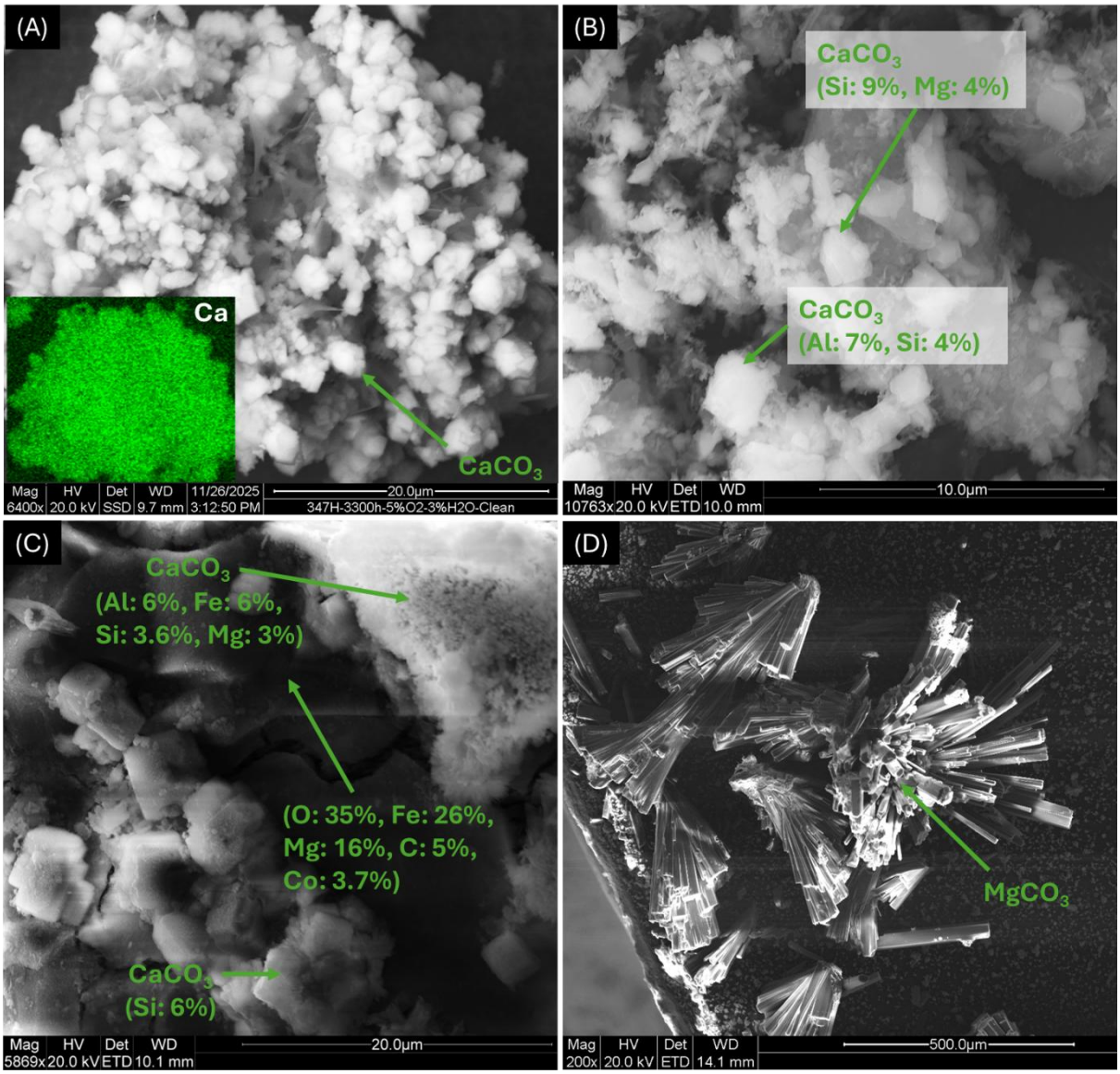

Figure 4.12. *SEM images of (A) Petrit T, (B) Petrit E and (C,D) Petrit L after carbonation.*

Summary

Four Ca and Mg-bearing industrial side streams were evaluated for their potential to sequester CO_2. GLD, a waste from the pulp and paper industry, provided by SCA, displayed absorption capacity between 74 and 114 kg / ton of feedstock. Three steel slags were provided from Höganäs and they displayed the potential to sequester 177 – 211 kg / ton of Petrit T, 81 – 116 kg / ton of Petrit E and 116 – 143 kg / ton of Petrit L.

Higher sequestration capacities were observed for mixtures prepared with lower S/L ratios. It was speculated that this is a result of the extraction of more metal ions in the aqueous phase which allows for the carbonation reactions to occur longer at the gas-liquid interphase before the carbonate ions react directly on the solid surface covering the solid particles with $CaCO_3$. Lower particle size had a positive effect on the carbonation potential, as expected. On the other hand, increasing temperature from ambient (25 °C) to 60 °C significantly hindered carbonation, owing to the reduced aqueous solubility of both CO_2 and $Ca(OH)_2$. The stirring time of the mixtures prior to carbonation was also found to have a significant effect. While an equilibrium of meat ion leaching was established within the first two hours for all the materials, stirring for up to 24 hours had a positive influence on the carbonation. This can be interpreted as a result of reduced particle size caused by the stirring motion.

Calcite was the primary product of the process for all samples and regardless of temperature, as suggested by the prominent XRD patterns, which are characteristic of calcite. Aragonite was also recognized as a much less prominent phase. SEM-EDS also revealed cubic, Ca-dominated structures nucleated on various substrates, supporting the XRD results, as well as less organized Ca-bearing growths with the presence of other elements, such as Si and Al in the lattice. $MgCO_3$ in the phase of nasquehonite was identified in the Mg-containing materials after carbonation.

These results provide insight into the possibility of these four industrial waste and by-products to sequester CO_2. Aqueous direct carbonation was an efficient method for low-energy carbonation. By evaluating different parameters, it was highlighted that the process benefits from conditions which extend the initial stage, where the reactants interact at the gas-liquid phase, and delay the deposition of solid carbonates directly on the particles' surface. The resulting products bear $CaCO_3$ and $MgCO_3$ in a variety of morphologies, either in standalone clusters or on the surface of substrates. These characteristics suggest that the carbonated products could potentially be used in construction applications, resulting in a secure and long-term storage of the absorbed CO_2.

Chapter 5:
Direct air capture via carbonation in NaOH-ethanol solutions

Based on **Paper VI**

Overview

This study investigates the use of NaOH-ethanol solutions for direct air capture. Solutions with concentrations of 10, 20, 30, 40, and 50 g/L were prepared, and compressed air was bubbled through each for a fixed duration of 8 hours. Two contactor configurations –a bubble column and a stirred reactor– were evaluated. Following each experiment, the mixtures were centrifuged to separate the precipitated solids from the remaining solution. The recovered solids were analyzed by acid gravimetry to quantify CO_2 uptake, and further characterized using NMR, FTIR, XRD, and SEM to identify the formed products.

Abbreviation of sample names

Table 5.1 shows the abbreviated names assigned to each experiment and sample that will be discussed in this chapter. The type of reactor is denoted as BC for bubble column and SR for stirred reactor. This is followed by the concentration of NaOH in ethanol in g/L. Samples of the precipitated solids and supernatant obtained by centrifugation are denoted with the letter P and S respectively, added after the first four characters. Finally, samples of the supernatant that has been oven-dried end with Sdried.

Table 5.1. *Short name of each precipitate sample accompanied by a description of the experiment that produced it.*

Description	Experiment	Precipitate	Liquid Supernatant	Dried Supernatant
10 g/L NaOH-EtOH solution in the bubble column	BC10	BC10P	BC10S	BC10Sdried
20 g/L NaOH-EtOH solution in the bubble column	BC20	BC20P	BC20S	BC20Sdried
30 g/L NaOH-EtOH solution in the bubble column	BC30	BC30P	BC30S	BC30Sdried
40 g/L NaOH-EtOH solution in the bubble column	BC40	BC40P	BC40S	BC40Sdried
50 g/L NaOH-EtOH solution in the bubble column	BC50	BC50P	BC50S	BC50Sdried
10 g/L NaOH-EtOH solution in the stirred reactor	SR10	SR10P	SR10S	SR10Sdried
20 g/L NaOH-EtOH solution in the stirred reactor	SR20	SR20P	SR20S	SR20Sdried
30 g/L NaOH-EtOH solution in the stirred reactor	SR30	SR30P	SR30S	SR30Sdried
40 g/L NaOH-EtOH solution in the stirred reactor	SR40	SR40P	SR40S	SR40Sdried
50 g/L NaOH-EtOH solution in the stirred reactor	SR50	SR50P	SR50S	SR50Sdried

Direct air capture experiments

Comparison of CO_2 absorption in the two types of reactors

The absorption of CO_2 in the bubble column experiments across all NaOH concentrations is displayed in Figure 5.1 along with the absorption of the 50 g/L solution in the stirred reactor. In the figure, the dashed line indicates the total mass of CO_2 that passed through the system over the 8 hours of experiment. As compressed air was used for all the experiments, the environment-dependent CO_2 concentration is a significant variable which can fluctuate throughout the duration of the experiments. The zone with grey colour expresses the entire range of recorded inlet CO_2 concentrations (458 – 496 ppm). The inset table reports the absorbed CO_2 (g/L of solution), with corresponding percentages relative to the total CO_2 supplied, based on the average concentration of 476 ppm. The results demonstrate two key advantages of the stirred reactor over the bubble column: higher CO_2 uptake and greater operational robustness. Although the borosilicate sparger in the bubble column provides a uniform gas distribution (Figure 2.4), it requires frequent maintenance, including cleaning with dilute acid, and exhibited recurrent clogging in experiments BC30 and BC40. In contrast, no clogging was observed at the other concentrations, which yielded comparable absorption values ranging from 2.64 to 2.98 g CO_2/L (approximately 32 – 36% of the introduced CO_2). In the stirred reactor, the 50 g/L solution achieved a CO_2 uptake of 7.53 g/L, nearly three times higher than that of the bubble column, corresponding to 91.6% of the supplied CO_2. This substantial improvement underscores the critical role of mixing for this system. Consistent with these findings, Tajik et al. reported enhanced carbonation efficiency with improved impeller design in NaOH-ethanol systems in **Paper IX** [132]. That study similarly demonstrated that stirring markedly enhances performance for 2 and 10 g/L solutions. Overall, the results indicate that increased viscosity and particle formation in NaOH-ethanol solutions limit CO_2 mass transfer, while effective mixing significantly mitigates these constraints.

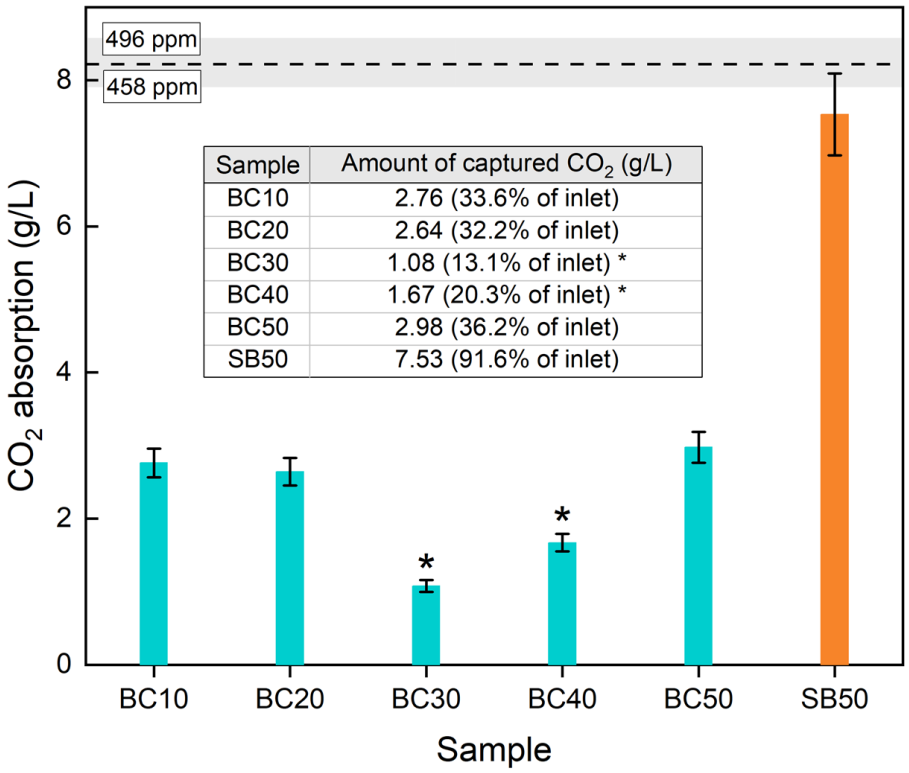

Figure 5.1. *CO_2 absorption in g/L of solution for all concentrations in the bubble column and 50 g/L NaOH-EtOH in the stirred reactor. *The sparger clogged resulting to very low airflow.*

Effect of NaOH concentration

The effect of the NaOH concentration on the performance of the system was investigated with the stirred reactor. The CO_2 uptake across all concentrations in the stirred reactor is displayed in Figure 5.2. With adequate mixing all the solutions showcased nearly complete removal of the CO_2 from the gas phase. The highest observed absorption was 8.27 g of CO_2/L in the 30 g/L solution. The results did not show a direct linear correlation between the NaOH concentration and the absorption of CO_2. The figure shows an upward trend of CO_2 absorption from 10 to 30 g/L followed by a slight decline at the two highest NaOH concentrations. Apart from the 10 g/L solution, which contained 0.4 g of NaOH in the 40 mL of solution, for all the other solutions the amount of NaOH is significantly higher than the stoichiometric amount required to absorb all the fed CO_2. Thus, the trend exhibited in Figure 5.2 is not a direct effect of the alkalinity of the solution, but an indirect effect related to the evaporation of ethanol. It was observed that increasing NaOH concentration led to greater retention of ethanol in the reactor. For the 10 and 20 g/L solutions, complete evaporation occurred within 8 hours, despite replenishment after 3 hours, as applied in all experiments. This likely explains the lower CO_2 uptake observed for SB10 and SB20. In contrast, the higher concentration systems retained liquid after 8 hours, with the 50 g/L solution exhibiting the greatest remaining volume. These findings suggest that

higher alkalinity reduces evaporation losses, thereby prolonging the effective activity of the absorbent. To verify that the reduced absorption in SB10 was not due to its lower alkalinity, an additional experiment was conducted in which sufficient ethanol was added to maintain a liquid phase throughout the duration of the test. Under these conditions, a CO_2 uptake of 8.22 g/L was achieved, comparable to that of SB30.

This observation raises the question of why solutions at the upper end of the concentration range exhibit a decline in performance. It was noted that SB40 and SB50 contained a high level of impurities after oven drying, occasionally leading to foaming and the formation of brown precipitates upon addition of 1 M HCl. To eliminate the influence of these artifacts on CO_2 quantification, SB40 and SB50 samples were treated with HCl immediately after centrifugation, omitting the drying step. For SB50, the measured CO_2 uptake remained essentially unchanged, yielding 7.46 and 7.58 g CO_2/L with and without drying, respectively. These values fall within the experimental standard deviation (±0.55 g CO_2/L). The average of these measurements is reported in Figure 5.2. In the case of SB40, an absorption of 7.96 g CO_2/L was obtained, with no evidence of foaming or formation of brown solids affecting the undried carbonates. The results suggest a trade-off between reduced evaporation losses at higher alkalinity and the accumulation of impurities, which warrants further investigation in future optimization studies.

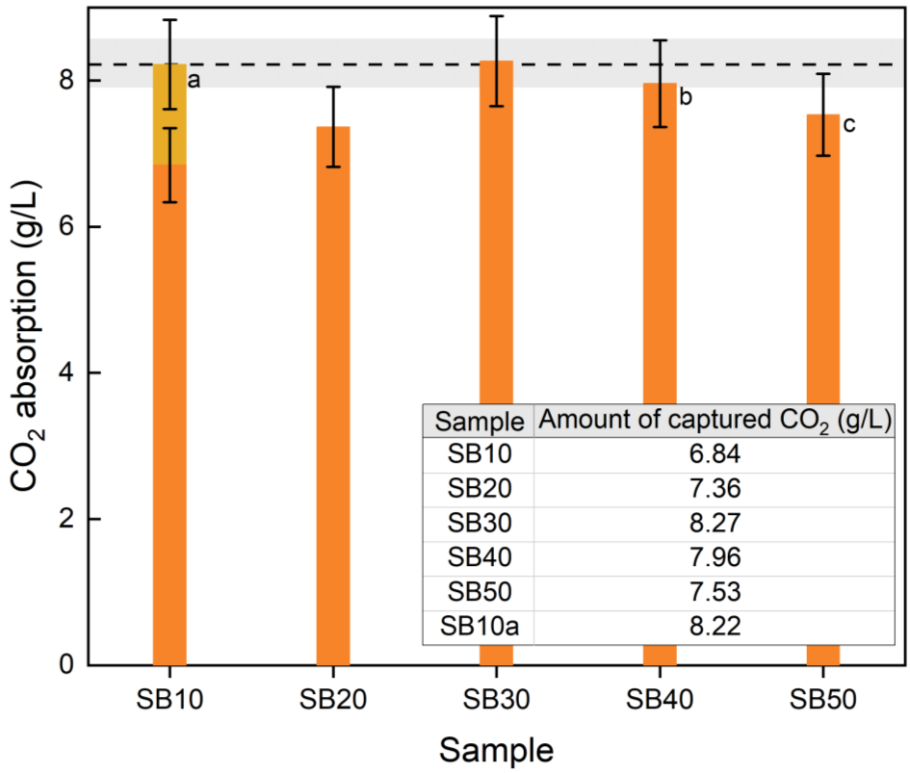

Figure 5.2. *CO_2 absorption in the stirred reactor for the different concentrations of NaOH. [a]SB10 was repeated, adding more ethanol to compensate for its faster evaporation. [b] SB40 was treated with HCl immediately after centrifugation to avoid the collection of impurities while drying. [c] SB50 was duplicated: one sample was titrated with HCl immediately after the experiment and one after oven drying. Their CO_2 absorption was almost the same.*

Effect of temperature

Considering that the objective of DAC is to remove atmospheric CO_2 with minimal energy input, it is important to evaluate absorbent performance across a broad temperature range. Figure 5.3 illustrates the CO_2 absorption of the SB10 system at – 0 °C, 45 °C, and room temperature. At the temperature extremes, CO_2 uptake decreased by 17% (–20 °C) and 23% (45 °C) relative to room temperature. Despite this reduction, performance remained comparatively high under both conditions. At –20 °C, CO_2 absorption exceeded that at 45 °C, while ethanol evaporation was negligible. This highlights a key advantage of alcohol-based absorbents over aqueous systems: effective operation in cold climates without the need for external temperature control. In contrast, the lowest absorption was observed at 45 °C (6.3 g CO_2/L of solution), although this value still surpasses the performance of the bubble column reactor. However, elevated temperature significantly increased ethanol evaporation, necessitating frequent solvent replenishment; at larger scales, this would imply a higher demand for ethanol recovery via condensation. Furthermore, the solution

developed a yellow coloration during the 8-hour experiment at 45 °C, indicating that higher temperatures may promote the formation of impurities.

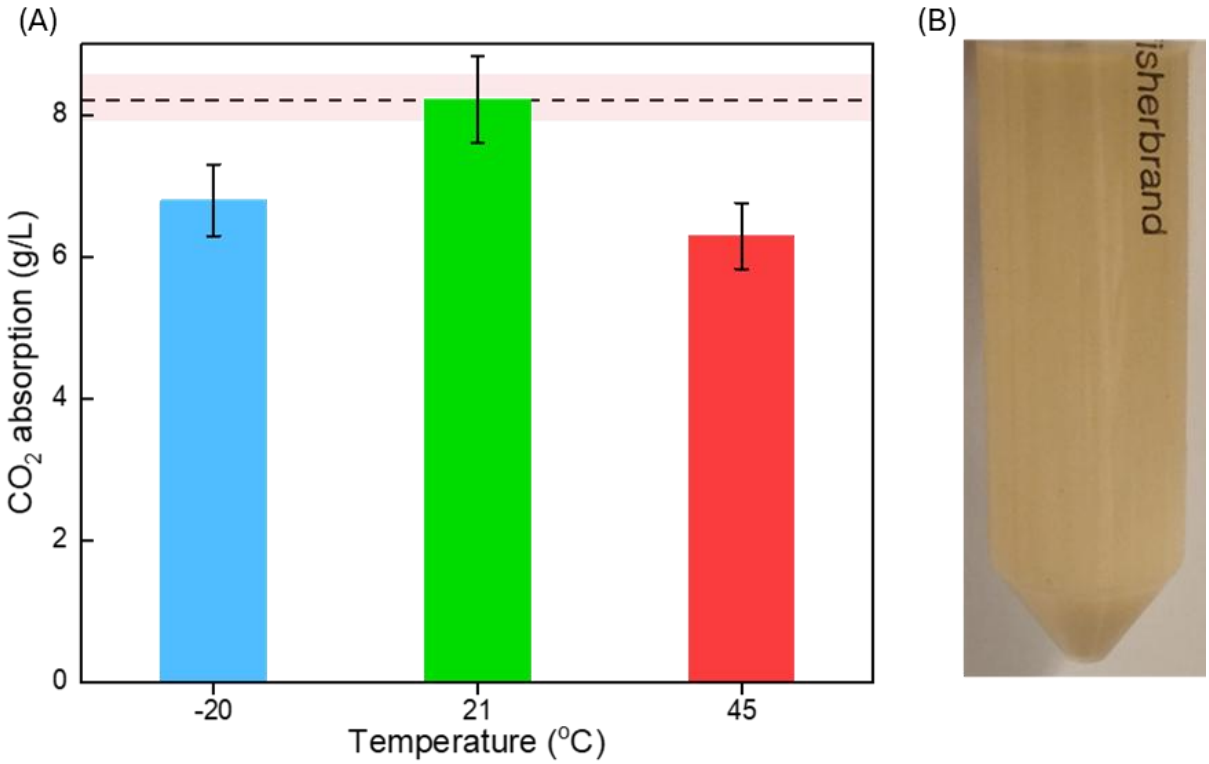

Figure 5.3. *(a) CO_2 absorbance in SB10 at three different temperatures within the range of Earth's surface temperature, (b) colour of the slurry of SB10 after the experiment at 45 °C.*

Impurities

The formation of impurities in the NaOH-ethanol solutions was prominent in the supernatant solutions after separating the solid precipitates. The supernatant solutions, containing spent ethanol, unreacted NaOH and dissolved carbonates were oven dried at 50 °C. In the oven, the remaining alkali in ethanol kept reacting with atmospheric CO_2. Table 5.2 shows the amount of CO_2 captured in BC10S and BC50S after oven drying. Apart from this the dried supernatants exhibited a change in colour, from white (at the lowest alkali concentration) to dark brown (at the highest alkali concentration). The progressive change of color of the supernatant across the NaOH concentration range is displayed in Figure 5.4.

Table 5.2. *Amount of CO_2 captured in BC10 and BC50 during the DAC experiment and in the respective supernatants while drying on the oven.*

Sample	CO_2 absorbed by solution during the DAC experiment	CO_2 absorbed by supernatant in the oven
BC10	0.111	0.125
BC50	0.119	0.857

A transition from a clear or white appearance to orange color has previously been reported in alkaline ethanol solutions and sodium ethoxide systems [133,134]. Tu et al. investigated this phenomenon and attributed it to the formation of carbon dots (CDs) in alkali-alcohol media. Their work indicates that, under highly alkaline conditions, ethanol can oxidize to aldehydes, which in the presence of a base (e.g., NaOH or sodium ethoxide) and a protic solvent undergo aldol condensation [135]. Both Tu et al. and Li et al. further demonstrated that these aldehydes participate in a series of base-catalyzed substitution and condensation reactions, yielding a wide range of carbonaceous intermediates that ultimately crosslink to form carbon dots [134,136]. These clusters of various chain lengths and functional groups crosslink to finally form carbon dots. Earlier, Yuan et al. had proposed a mechanism for NaOH-catalyzed aerobic oxidation of alcohols [137]. Under the experimental conditions of their study, acetaldehyde was not directly detected. It was discussed that, at high alkalinity, acetaldehyde is unstable and rapidly converts via a geminal diol intermediate to acetate. The formation of acetate has also been reported in a study on the decomposition of sodium methoxide and ethoxide[138]. In particular, sodium acetate (CH_3COONa) and sodium formate (HCOONa) were identified as major components in commercial sodium ethoxide, attributed to degradation during storage. To further elucidate the formation of carbonate products and associated impurities in this work, the samples were characterized using FTIR and ^{1}H, ^{13}C NMR.

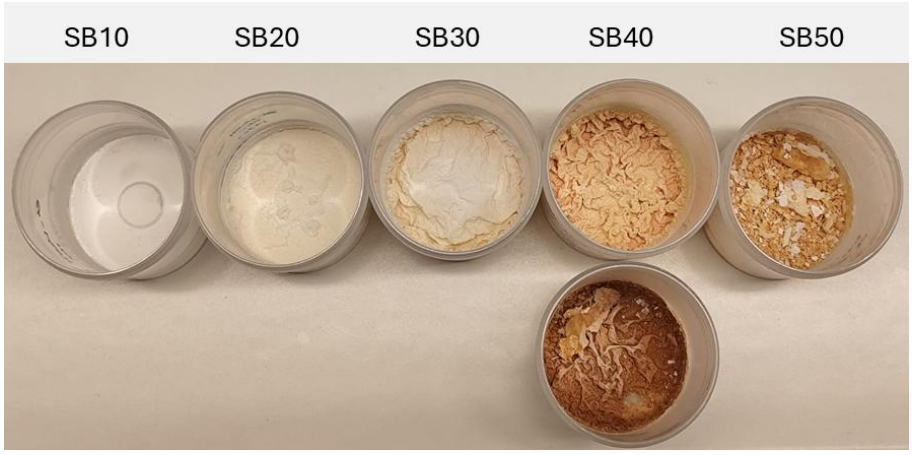

***Figure 5.4**. Colour of dried supernatants for all the concentrations.*

Physicochemical characterization of products and impurities

Figure 5.5 displays the FTIR spectra of four samples: BC40Sdried – which exhibited a dark orange color –, BC30S collected directly after centrifugation and stored in a falcon tube for a few days, BC50P and BC10P. All the samples exhibited bands at 1440 – 1420 and 880 cm^{-1} which are characteristic for the stretching and bending of the carbonate ion respectively [139]. The BC30S sample contained carbonates after reacting with atmospheric CO_2 during storage. These bands were most prominent for BC50P, which did not display other significant peaks. Bands at 3500 cm^{-1} (O–H stretching), 3000 – 2680 cm^{-1} (C–H stretching), 1374 cm^{-1}, 1090 cm^{-1} and 1050 cm^{-1} (C–O stretching) could be attributed to ethanol [140]. These were most prominent in BC30S as expected. The O–H stretching band can also originate from the NaOH. The BC40Sdried and BC10P also showed the 1374 cm^{-1}, 1090 cm^{-1} and 1050 cm^{-1} C–O stretching bands, suggesting that some ethanol could be retained in the samples after drying. BC40Sdried also displayed the ethanol C–H stretching band in the range of 3000–2680 cm^{-1}. A band at 1616 cm^{-1} was also present in all spectra, but most noticeable in BC10P and BC40Sdried. This could be attributed to the C=O stretching of HCOONa, but it could belong to another carboxylate [141,142]. The peaks that clearly distinguish the orange solids of BC40 from all other samples are at 790 and 534 cm^{-1}. Both are in the fingerprint area of IR, which is difficult to interpret, but according to literature they could be assigned to C=C bending and vibrations of aromatic compounds, respectively [141,143,144]. The presence of peaks in the fingerprint area, is alone proof that ethanol undergoes side reactions catalyzed by NaOH.

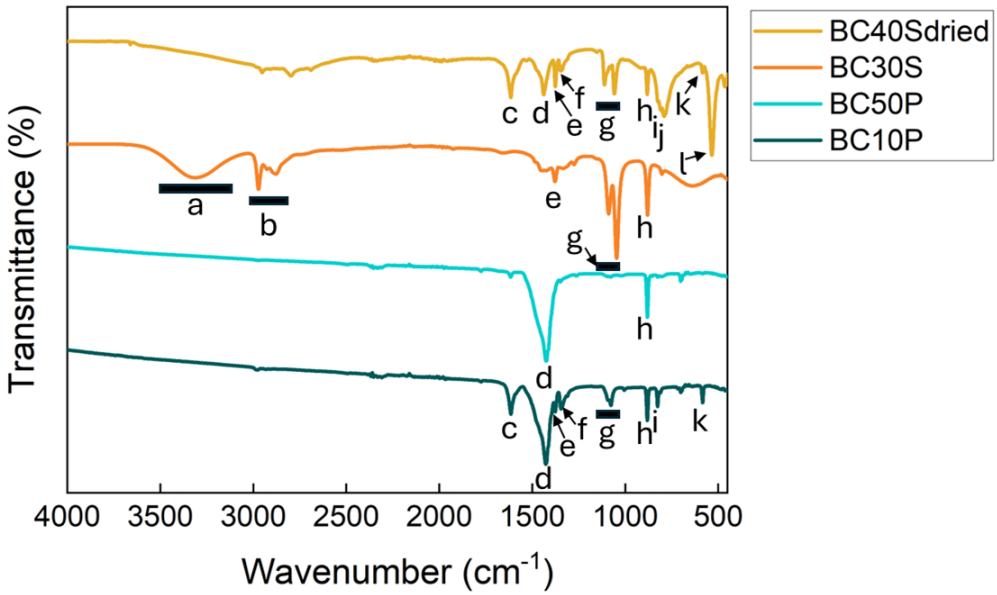

a (~3500)	ethanol O-H streching
b (3000-2680)	ethanol C-H stretching
c (1616)	formate C=O stretching
d (1420-1440)	carbonate ion streching
e (1374)	ethanol C-O stretch
f (1346)	O-H bending of alcohol or phenol

g (1090, 1050)	ethanol C-O stretch
h (880)	carbonate ion bending
i (825)	alkene or aromatic C=C bending
j (790)	C=C bending
k, l (585, 534)	vibrations of aromatic compounds

Figure 5.5. *Top: FTIR spectra of four samples, BC40Sdried, BC30S (after a few days kept in a falcon tube), BC50P and BC10P. Bottom: peak assignment based on literature [139–144].*

^{1}H NMR spectroscopy was performed to further investigate the formed products. Figure 5.6 presents the spectra of four representative samples. All spectra exhibited the characteristic signals of ethanol, although the intensity was lowest for BC50P, consistent with the corresponding FTIR results. The solid samples – BC10P, BC50P, and BC50Sdried – also showed signals near 0 ppm, which are attributed to silicone-based vacuum grease used to seal the glass components of the bubble column (Figure 2.4) [145]. Additional signals were identified at approximately 8.5 ppm and 1.9 ppm, corresponding to $HCOO^-$ and CH_3COO^-, respectively. Comparable observations have been reported by Wethman et al. in their analysis of impurities in commercial sodium ethoxide [34]. Furthermore, two small peaks near 7.4 ppm in the BC50P sample indicate the presence of aromatic species. However, these signals were absent in the NMR spectrum of BC50Sdried, which has a distinct brown color. This could suggest that the concentration of impurities in the samples was too low, thus not producing detectable signal.

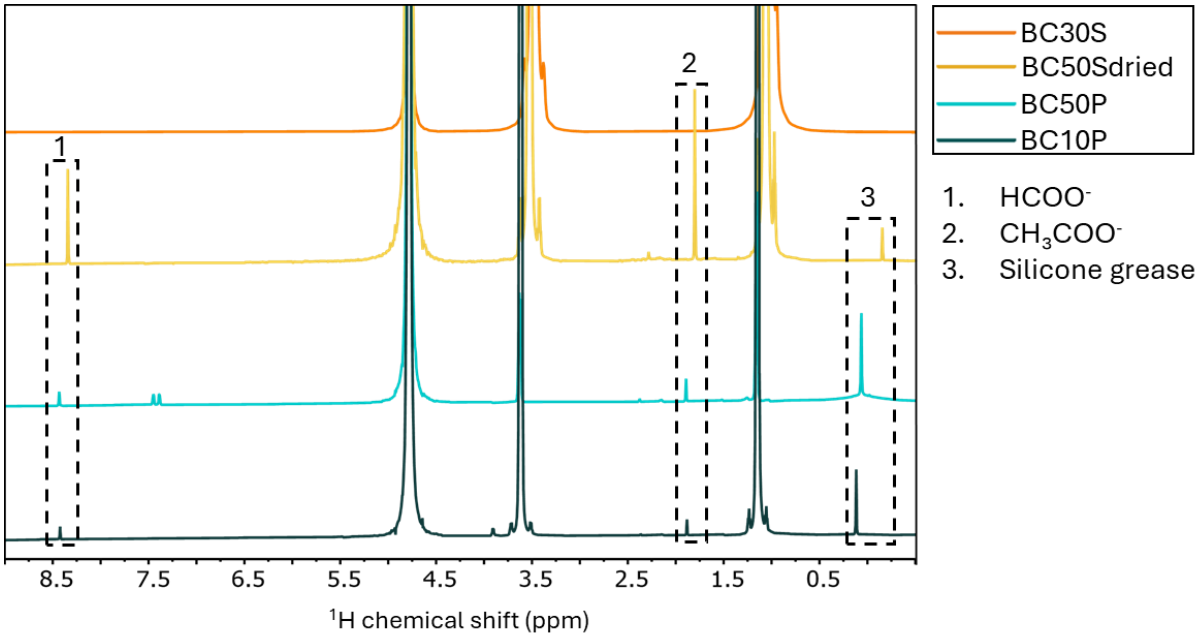

Figure 5.6. *^{1}H NMR of BC10P, BC50P, BC50Sdried and BC30S.*

^{13}C NMR revealed a carbonate peak near 168 ppm, which corresponds to Na_2CO_3. Figure 5.7 (left) shows the spectra of the four samples. No carbonate signal was observed in the liquid supernatant, indicating that no detectable carbonates remained in the liquid phase after centrifugation. In contrast, the FTIR analysis suggested the presence of carbonate peaks in BC30S. This could be attributed to the fact that the measurement was performed several weeks after the sample collection and despite storage in a sealed vial, partial carbonation likely occurred during this period. Signals corresponding to $HCOO^-$ and CH_3COO^- peaks were not clearly resolved in the ^{13}C. Nevertheless, both species were identified using HSQC analysis (Figure 5.7, right). The ^{1}H resonance assigned to CH_3COO^- showed a corresponding ^{13}C signal from its CH_3 group, while the ^{1}H signal of $HCOO^-$ also correlated with its respective carbon signal.

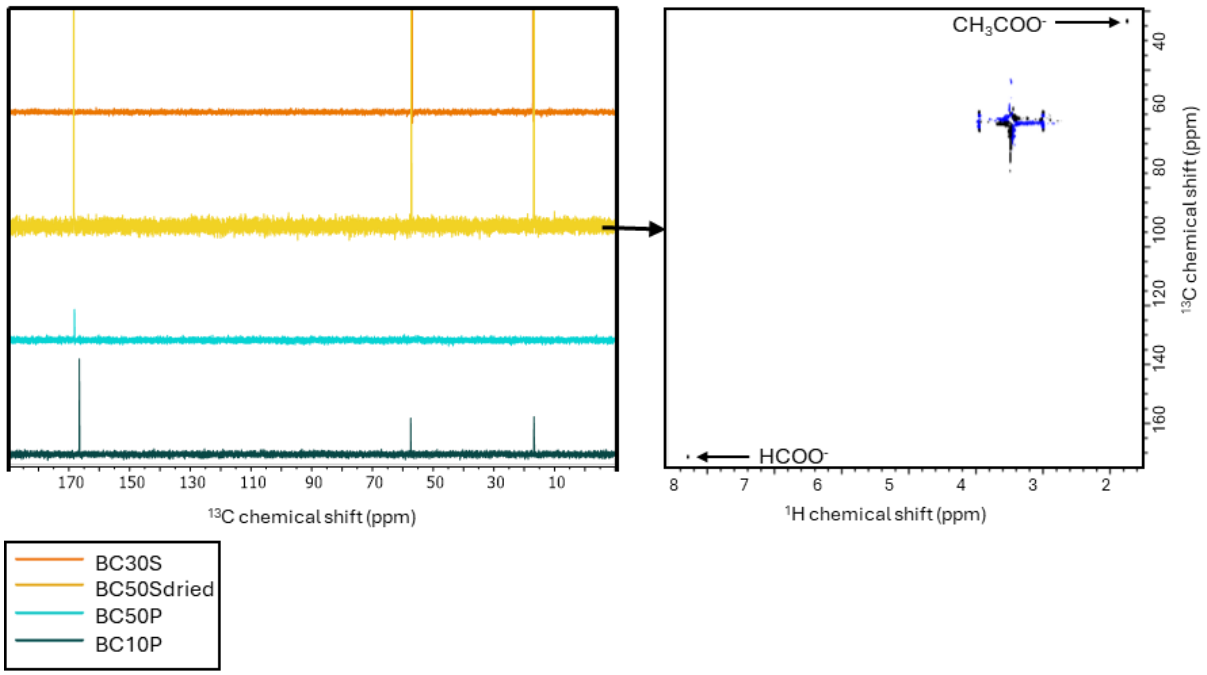

Figure 5.7. *Left: ^{13}C NMR of BC10P, BC50P, BC50Sdried and BC30S. Right: HSQC spectrum of BC50Sdried.*

Figure 5.8 displays the XRD diffractogram (A) and a SEM image (B) of a BC30P sample. The diffractogram indicates a dominant presence of monoclinic natrite, with no detectable reflections corresponding to nahcolite, in agreement with the NMR results. Mun et. al. have shown that the water content of the system influences the nature of the carbonate phases formed [90], suggesting that adjustment of water content could enable selective formation of $NaHCO_3$. In addition to the expected reflections, the diffractogram contains peaks that cannot be assigned to either Na_2CO_3 or $NaHCO_3$. These have previously been attributed to SEC by Mun et. al. [90]. However, there is no clear evidence for SEC formation under the present experimental conditions. FTIR and NMR analyses instead indicate the presence of ethanol within the solid carbonates, although not chemically bound, as also reported by Raktim Sen et. al. and Robert Wethman et. al. [93,133]. Accordingly, these additional reflections are more plausibly attributed to the crystallization of Na_2CO_3 in the presence of ethanol, resulting in solvent incorporation within the crystal lattice [146]. These features are labeled in Figure 5.8 as Na_2CO_3 solvate. The SEM image revealed unstructured particles, assembled in clusters. Plaque-like structures were observed, characterized by one smooth and one rough side. These features likely originate from the outer layer of the centrifuged and dried solids. It is plausible that the applied centrifugal force contributed to the formation of a smooth surface layer, highlighting the structural adaptability of the formed carbonate material.

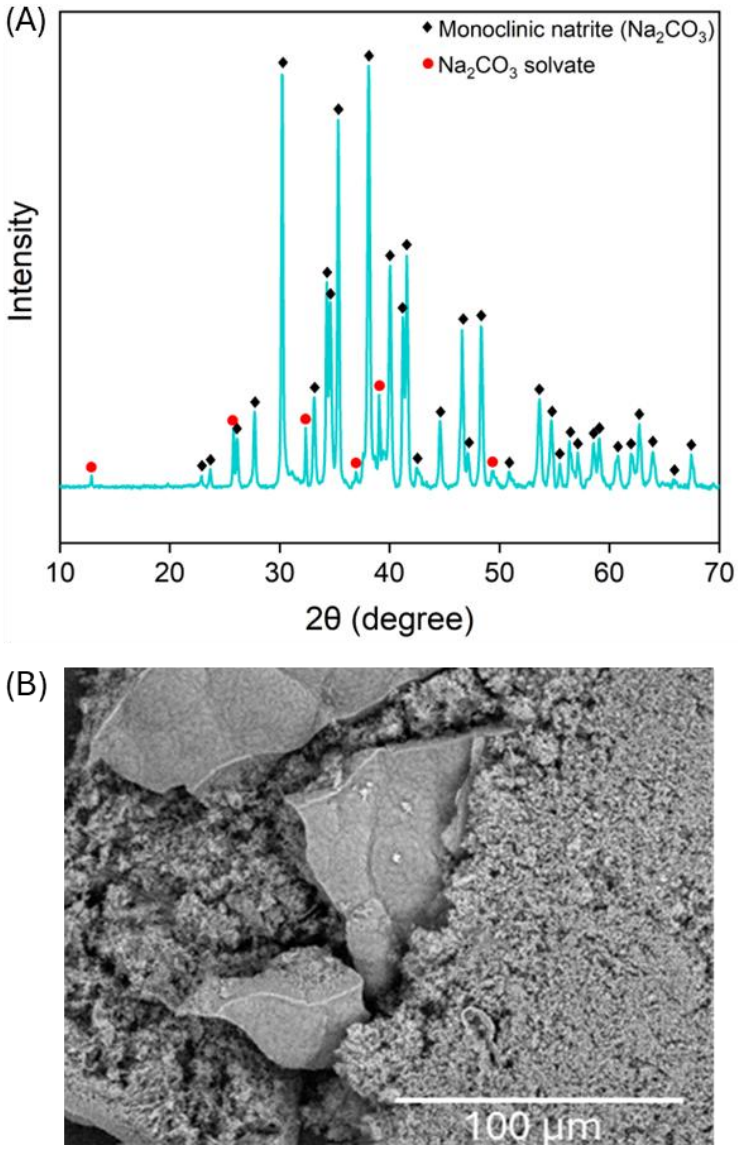

Figure 5.8. *(A) XRD diffractogram and (B) SEM image of a BC30 sample.*

Summary

The potential of NaOH-ethanol solutions and effective absorbents for DAC was evaluated across a wide range of conditions. Experiments with two types of reactors (a bubble column and a stirred reactor) showcased that the reactor design is critical. The bubble column suffered from clogging, whereas the stirred reactor provided more robust operation and achieved significantly higher absorption, removing more than 90% of CO_2 from the gas stream. CO_2 absorption was primarily limited by mass transfer rather than NaOH concentration, indicating that higher alkalinity does not necessarily improve performance within practical timescales. While increased NaOH reduced ethanol evaporation, it also promoted impurity formation.

The system also remained effective at both −20 °C and 45 °C, although ethanol evaporation was significantly accelerated at the higher temperature, which suggests that the energy demand of condensation might become critical if this technology is applied in warm climates. The formation of impurities was also found to be enhanced by the higher temperature.

Product characterization confirmed Na_2CO_3 as the main phase, predominantly in the form of natrite, with evidence of possible solvates due to crystallization in ethanol. SEM analysis showed irregular, agglomerated particle morphologies. The exact molecular composition of the impurities was not identified, and their concentration appeared to be too low to produce notable signal in NMR.

Overall, NaOH-ethanol systems offer promising features for DAC, including broad temperature operability and inherent solid separation. However, challenges related to impurity formation, reactor design, and especially carbonate regeneration remain.

Chapter 6: Conclusions and Future work

The present thesis has explored the potential of carbon capture via inorganic carbonation in various absorbent systems including both model systems and industrial side-streams. The focus has been on investigating the reactivity, absorption capacities, reaction mechanism and formation of products in each system, as well as identifying the benefits and constraints of each system. The work has been divided into chapters based on the three distinct types of absorbent systems. This section summarizes the key findings and outlines potentials for future research required to advance these processes toward industrial implementation.

The first system examined was aqueous NaOH. Solutions of NaOH in a range of concentrations were studied as reference to establish the experimental setup and subsequently black liquor was also investigated as an absorbent. Black liquor, a by-product of soda pulping, contains significant amounts of NaOH used in biomass delignification. Due to its high alkalinity, it readily absorbs CO_2, with mass transfer between the gas and liquid phases identified as the main rate-limiting step. The presence of surface-active compounds led to foaming, which could be mitigated through antifoam addition and agitation. As CO_2 absorption lowered the pH to around 8, lignin fractions and silica precipitated. This aligns with established approaches for lignin recovery via CO_2 acidification.

These findings suggest that black liquor carbonation could serve as part of an integrated valorization process, where controlled pH reduction enables sequential recovery of silica and lignin, followed by CO_2 release under further acidification under vacuum. Such a process could simultaneously capture CO_2 and generate multiple valuable streams. However, thorough technoeconomic analysis is required to bring this process to larger scale. It can be speculated that the amount of silica present in biomass is not significant and the market value of CO_2 and lignin are not yet sufficiently high to incentivize the implementation of this process outside of research scale. Nevertheless, the global economy seems to be on a pathway where CO_2 and biomolecules will be increasingly more valuable, thus processes such as these might become attractive in replacing the fossil-centered processes which are currently in place. Additionally, silica from agricultural by-products is progressively gaining more attention for its potential use in alkali activated concrete.

Following the evaluation of an alkaline side stream in carbon capture, four Ca and Mg-bearing industrial side streams were investigated in carbon capture. Three of those

were steel slags from Höganäs with commercial names Petrit T, E and L and the last was a pulp and paper waste from SCA called GLD. The effect of S/L ratio, temperature, particle size and stirring time prior to carbonation were investigated. GLD is a soft solid which primarily contains Ca in the form of $CaCO_3$, but $Ca(OH)_2$ is also present. It displayed the lowest absorption capacity of 74 – 114 kg / ton of feedstock. The steel slags presented sequestration capacities of up to 211 kg / ton of feedstock. Sequestration increased at lower S/L ratios, likely due to enhanced metal ion extraction and prolonged gas-liquid carbonation before surface passivation by $CaCO_3$. Smaller particle sizes improved performance significantly for Petrit E and L, but the effect was less prominent for GLD, likely because it is a soft material which easily breaks into smaller particles with mechanical agitation. Increasing the temperature from 25 to 60 °C reduced carbonation due to lower CO_2 and $Ca(OH)_2$ solubility. Although metal leaching equilibrated within 4 hours of stirring the mixtures, extended stirring up to 24 h further enhanced carbonation, likely through particle size reduction. Calcite was the dominant product across all conditions, with minor aragonite formation. Mg-containing samples also formed $MgCO_3$ (nasquehonite).

Aqueous carbonation proved effective under conditions that prolong gas-liquid interactions and delay surface passivation. The resulting carbonate products show promise for construction applications, enabling stable, long-term CO_2 storage. While direct aqueous carbonation of slags is well studied, large-scale implementation remains limited. In **Paper X**, Shavalieva et al. investigated the life cycle assessment of CO_2 sequestration in GLD based on results from our work [147]. This work identified post-carbonation drying as a major energy demand and emphasized that the viability of the process depends on the utilization of the carbonated products. Their incorporation into concrete, particularly as partial cement replacements, offers the greatest environmental benefit. Advancing this pathway requires further research into material performance to ensure compatibility with conventional construction standards.

The final system explored NaOH dissolved in ethanol for DAC. In contrast to the previous systems, where mixtures of CO_2 and N_2 were used to simulate flue gas compositions, this approach targeted atmospheric CO_2. The combination of high alkalinity and in situ carbonate precipitation could be advantageous for DAC. The reactor design was found to be critical. A bubble column reactor suffered from clogging

due to the formation of solid particles, whereas a stirred reactor achieved stable operation and over 90% CO_2 removal. Absorption was primarily limited by the low concentration of CO_2 in the gas, rather than NaOH concentration (10 – 50 g/L). While higher NaOH concentrations reduced ethanol evaporation, they also promoted impurity formation. Na_2CO_3, mainly as natrite, was identified as the primary product.

The main challenge for this system lies in regeneration. Na_2CO_3 has low economic value, and its thermal decomposition to release CO_2 requires temperatures above 1000 °C, making the process energy intensive. Therefore, the development of energy-efficient regeneration pathways for NaOH is critical for competitiveness with existing DAC technologies. Although preliminary studies have explored such approaches, further research is needed to establish viable regeneration strategies [148,149].

References

[1] P.M. Forster, C. Smith, T. Walsh, W.F. Lamb, R. Lamboll, C. Cassou, M. Hauser, Z. Hausfather, J.-Y. Lee, M.D. Palmer, K. von Schuckmann, A.B.A. Slangen, S. Szopa, B. Trewin, J. Yun, N.P. Gillett, S. Jenkins, H.D. Matthews, K. Raghavan, A. Ribes, J. Rogelj, D. Rosen, X. Zhang, M. Allen, L. Aleluia Reis, R.M. Andrew, R.A. Betts, A. Borger, J.A. Broersma, S.N. Burgess, L. Cheng, P. Friedlingstein, C.M. Domingues, M. Gambarini, T. Gasser, J. Gütschow, M. Ishii, C. Kadow, J. Kennedy, R.E. Killick, P.B. Krummel, A. Liné, D.P. Monselesan, C. Morice, J. Mühle, V. Naik, G.P. Peters, A. Pirani, J. Pongratz, J.C. Minx, M. Rigby, R. Rohde, A. Savita, S.I. Seneviratne, P. Thorne, C. Wells, L.M. Western, G.R. van der Werf, S.E. Wijffels, V. Masson-Delmotte, P. Zhai, Indicators of Global Climate Change 2024: annual update of key indicators of the state of the climate system and human influence, Earth Syst. Sci. Data 17 (2025) 2641–2680. https://doi.org/10.5194/essd-17-2641-2025.

[2] Global Energy Review 2025, Paris, n.d. https://www.iea.org/reports/global-energy-review-2025 (accessed February 24, 2026).

[3] R.K. Pachauri, L.A. Meyer, Climate Change 2014: Synthesis Report. Contribution of Working Groups I, II and III to the Fifth Assessment Report of the Intergovernmental Panel on Climate Change, 2014.

[4] K. Calvin, D. Dasgupta, G. Krinner, A. Mukherji, P.W. Thorne, C. Trisos, J. Romero, P. Aldunce, K. Barret, G. Blanco, W.W.L. Cheung, S.L. Connors, F. Denton, A. Diongue-Niang, D. Dodman, M. Garschagen, O. Geden, B. Hayward, C. Jones, F. Jotzo, T. Krug, R. Lasco, Y.-Y. Lee, V. Masson-Delmotte, M. Meinshausen, K. Mintenbeck, A. Mokssit, F.E.L. Otto, M. Pathak, A. Pirani, E. Poloczanska, H.-O. Pörtner, A. Revi, D.C. Roberts, J. Roy, A.C. Ruane, J. Skea, P.R. Shukla, R. Slade, A. Slangen, Y. Sokona, A.A. Sörensson, M. Tignor, D. van Vuuren, Y.-M. Wei, H. Winkler, P. Zhai, Z. Zommers, J.-C. Hourcade, F.X. Johnson, S. Pachauri, N.P. Simpson, C. Singh, A. Thomas, E. Totin, A. Alegría, K. Armour, B. Bednar-Friedl, K. Blok, G. Cissé, F. Dentener, S. Eriksen, E.

Fischer, G. Garner, C. Guivarch, M. Haasnoot, G. Hansen, M. Hauser, E. Hawkins, T. Hermans, R. Kopp, N. Leprince-Ringuet, J. Lewis, D. Ley, C. Ludden, L. Niamir, Z. Nicholls, S. Some, S. Szopa, B. Trewin, K.-I. van der Wijst, G. Winter, M. Witting, A. Birt, M. Ha, IPCC, 2023: Climate Change 2023: Synthesis Report, Summary for Policymakers. Contribution of Working Groups I, II and III to the Sixth Assessment Report of the Intergovernmental Panel on Climate Change [Core Writing Team, H. Lee and J. Romero (eds.)]. IPCC, Geneva, Switzerland., 2023. https://doi.org/10.59327/IPCC/AR6-9789291691647.001.

[5] A.I. Osman, L. Chen, M. Yang, G. Msigwa, M. Farghali, S. Fawzy, D.W. Rooney, P.-S. Yap, Cost, environmental impact, and resilience of renewable energy under a changing climate: a review, Environ. Chem. Lett. 21 (2023) 741–764. https://doi.org/10.1007/s10311-022-01532-8.

[6] H. Adun, J.D. Ampah, O. Bamisile, Y. Hu, I. Staffell, H.R. Gilani, Near-term carbon dioxide removal deployment can minimize disruptive pace of decarbonization and economic risks towards United States' net-zero goal, Commun. Earth Environ. 5 (2024) 770. https://doi.org/10.1038/s43247-024-01916-4.

[7] S. Afrane, J.D. Ampah, H. Adun, J.L. Chen, H. Zou, G. Mao, P. Yang, Targeted carbon dioxide removal measures are essential for the cost and energy transformation of the electricity sector by 2050, Commun. Earth Environ. 6 (2025) 227. https://doi.org/10.1038/s43247-025-02190-8.

[8] H. McLaughlin, A.A. Littlefield, M. Menefee, A. Kinzer, T. Hull, B.K. Sovacool, M.D. Bazilian, J. Kim, S. Griffiths, Carbon capture utilization and storage in review: Sociotechnical implications for a carbon reliant world, Renewable and Sustainable Energy Reviews 177 (2023) 113215. https://doi.org/10.1016/j.rser.2023.113215.

[9] A.I. Hadi, A. Yan, Y. Hu, B. Lin, T. Zhou, D. Ouyang, J. Tang, A comprehensive review of carbon capture: From conventional to emerging electrochemical technologies, Next Energy 9 (2025) 100415. https://doi.org/10.1016/j.nxener.2025.100415.

[10] S. Nagireddi, J.R. Agarwal, D. Vedapuri, Carbon Dioxide Capture, Utilization, and Sequestration: Current Status, Challenges, and Future Prospects for Global Decarbonization, ACS Engineering Au 4 (2024) 22–48. https://doi.org/10.1021/acsengineeringau.3c00049.

[11] C. Wu, Q. Huang, Z. Xu, A.T. Sipra, N. Gao, L.P. de S. Vandenberghe, S. Vieira, C.R. Soccol, R. Zhao, S. Deng, S.K.S. Boetcher, S. Lu, H. Shi, D. Zhao, Y. Xing, Y. Chen, J. Zhu, D. Feng, Y. Zhang, L. Deng, G. Hu, P.A. Webley, D. Liang, Z. Ba, A. Mlonka-Mędrala, A. Magdziarz, N. Miskolczi, S. Tomasek, S.S. Lam, S.Y. Foong, H.S. Ng, L. Jiang, X. Yan, Y. Liu, Y. Ji, H. Sun, Y. Zhang, H. Yang, X. Zhang, M. Sun, D.C.W. Tsang, J. Shang, C. Muller, M. Rekhtina, M. Krödel, A.H. Bork, F. Donat, L. Liu, X. Jin, W. Liu, S. Saqline, X. Wu, Y. Xu, A.L. Khan, Z. Ali, H. Lin, L. Hu, J. Huang, R. Singh, K. Wang, X. He, Z. Dai, S. Yi, A. Konist, M.H.S. Baqain, Y. Zhao, S. Sun, G. Chen, X. Tu, A. Weidenkaff, S. Kawi, K.H. Lim, C. Song, Q. Yang, Z. Zhao, X. Gao, X. Jiang, H. Ji, T.E. Akinola, A. Lawal, O.S. Otitoju, M. Wang, G. Zhang, L. Ma, B.C. Sempuga, X. Liu, E. Oko, M. Daramola, Z. Yu, S. Chen, G. Kang, Q. Li, L. Gao, L. Liu, H. Zhou, A comprehensive review of carbon capture science and technologies, Carbon Capture Science & Technology 11 (2024) 100178. https://doi.org/10.1016/j.ccst.2023.100178.

[12] K.Z. House, A.C. Baclig, M. Ranjan, E.A. van Nierop, J. Wilcox, H.J. Herzog, Economic and energetic analysis of capturing CO $_2$ from ambient air, Proceedings of the National Academy of Sciences 108 (2011) 20428–20433. https://doi.org/10.1073/pnas.1012253108.

[13] S. Kammerer, I. Borho, J. Jung, M.S. Schmidt, Review: CO2 capturing methods of the last two decades, International Journal of Environmental Science and Technology 20 (2023) 8087–8104. https://doi.org/10.1007/s13762-022-04680-0.

[14] H. Asgharian, D.L. Marques, F. Iov, V. Liso, M.P. Nielsen, J.Z. Thellufsen, H. Lund, The role of cryogenic carbon capture in future carbon-neutral societies, International Journal of Greenhouse Gas Control 135 (2024) 104161. https://doi.org/10.1016/j.ijggc.2024.104161.

[15] B. Wang, C.Q. Lan, Biofixation of carbon dioxide (CO2) by microorganisms, in: Developments and Innovation in Carbon Dioxide (CO2) Capture and Storage

Technology, Elsevier, 2010: pp. 411–432. https://doi.org/10.1533/9781845699581.4.411.

[16] P. Xu, C.T. Reinhard, Evaluating the carbon capture potential of industrial waste as a feedstock for enhanced weathering, Environmental Research Letters 20 (2025) 044013. https://doi.org/10.1088/1748-9326/adc020.

[17] P. Renforth, The negative emission potential of alkaline materials, Nat. Commun. 10 (2019) 1401. https://doi.org/10.1038/s41467-019-09475-5.

[18] I. Walker, R. Bell, K. Rippy, Mineralization of alkaline waste for CCUS, Npj Materials Sustainability 2 (2024) 28. https://doi.org/10.1038/s44296-024-00031-x.

[19] E.R. Bobicki, Q. Liu, Z. Xu, H. Zeng, Carbon capture and storage using alkaline industrial wastes, Prog. Energy Combust. Sci. 38 (2012) 302–320. https://doi.org/10.1016/j.pecs.2011.11.002.

[20] H.-M. Lo, Y.-L. Liao, The metal-leaching and acid-neutralizing capacity of MSW incinerator ash co-disposed with MSW in landfill sites, J. Hazard. Mater. 142 (2007) 512–519. https://doi.org/10.1016/j.jhazmat.2006.08.054.

[21] L. Schwich, T. Schubert, B. Friedrich, Early-Stage Recovery of Lithium from Tailored Thermal Conditioned Black Mass Part I: Mobilizing Lithium via Supercritical CO2-Carbonation, Metals (Basel). 11 (2021) 177. https://doi.org/10.3390/met11020177.

[22] M. Yoo, S.-J. Han, J.-H. Wee, Carbon dioxide capture capacity of sodium hydroxide aqueous solution, J. Environ. Manage. 114 (2013) 512–519. https://doi.org/10.1016/j.jenvman.2012.10.061.

[23] B.E. Poling, G.H. Thomson, D.G. Friend, R.L. Rowley, W.V. Wilding, Perry's Chemical Engineers Handbook, 8th ed., 2008. DOI: 10.1036/0071511253 (accessed February 24, 2026).

[24] S.-J. Han, M. Yoo, D.-W. Kim, J.-H. Wee, Carbon Dioxide Capture Using Calcium Hydroxide Aqueous Solution as the Absorbent, Energy & Fuels 25 (2011) 3825–3834. https://doi.org/10.1021/ef200415p.

[25] A.A. Olajire, A review of mineral carbonation technology in sequestration of CO2, J. Pet. Sci. Eng. 109 (2013) 364–392. https://doi.org/10.1016/j.petrol.2013.03.013.

[26] W.M. Haynes, ed., CRC Handbook of Chemistry and Physics, CRC Press, 2014. https://doi.org/10.1201/b17118.

[27] L. Nicoleau, A. Nonat, D. Perrey, The di- and tricalcium silicate dissolutions, Cem. Concr. Res. 47 (2013) 14–30. https://doi.org/10.1016/j.cemconres.2013.01.017.

[28] S. Ye, P. Feng, J. Lu, L. Zhao, Q. Liu, Q. Zhang, J. Liu, J.W. Bullard, Solubility of tricalcium aluminate from 10 °C to 40 °C, Cem. Concr. Res. 162 (2022) 106989. https://doi.org/10.1016/j.cemconres.2022.106989.

[29] A. Coppola, F. Scala, M. Azadi, Direct Dry Carbonation of Mining and Industrial Wastes in a Fluidized Bed for Offsetting Carbon Emissions, Processes 10 (2022) 582. https://doi.org/10.3390/pr10030582.

[30] M.S. Kothari, B.A. Mohamed, A. Aly Hassan, A. Eldieb, H. El-Hassan, Environmental impacts of low-temperature CO2 sequestration via carbide slag waste mineral carbonation and utilization of carbonated end-product, J. Environ. Chem. Eng. 13 (2025) 119767. https://doi.org/10.1016/j.jece.2025.119767.

[31] F. Bonfante, G. Ferrara, J.-M. Tulliani, P. Palmero, A comprehensive review of direct aqueous mineral carbonation of industrial wastes using principal component analysis, J. Sustain. Cem. Based. Mater. 15 (2026) 294–318. https://doi.org/10.1080/21650373.2025.2567002.

[32] Y.-Q. Niu, J.-H. Liu, C. Aymonier, S. Fermani, D. Kralj, G. Falini, C.-H. Zhou, Calcium carbonate: controlled synthesis, surface functionalization, and nanostructured materials, Chem. Soc. Rev. 51 (2022) 7883–7943. https://doi.org/10.1039/D1CS00519G.

[33] R.C. Ropp, Group 14 (C, Si, Ge, Sn, and Pb) Alkaline Earth Compounds, in: Encyclopedia of the Alkaline Earth Compounds, Elsevier, 2013: pp. 351–480. https://doi.org/10.1016/B978-0-444-59550-8.00005-3.

[34] B. Xie, X. Wang, Y. Sun, P. Zhang, J. Song, J. Li, C. Sun, W. Wang, Carbonation sequestration of CO2 using industrial solid wastes: Research progress, enhancement mechanisms, and applications in building materials, J. Environ. Chem. Eng. 13 (2025) 120029. https://doi.org/10.1016/j.jece.2025.120029.

[35] W. Liu, L. Teng, S. Rohani, Z. Qin, B. Zhao, C.C. Xu, S. Ren, Q. Liu, B. Liang, CO2 mineral carbonation using industrial solid wastes: A review of recent developments, Chemical Engineering Journal 416 (2021) 129093. https://doi.org/10.1016/j.cej.2021.129093.

[36] F.M. Baena-Moreno, E. Leventaki, A. Riddell, J. Wojtasz-Mucha, D. Bernin, Effluents and residues from industrial sites for carbon dioxide capture: a review, Environ. Chem. Lett. (2022). https://doi.org/10.1007/s10311-022-01513-x.

[37] K. Horii, Y. Kitano, N. Tsutsumi, T. Kato, Processing and reusing technologies for steelmaking slag, Tokyo, 2013.

[38] Mineral commodity summaries 2024, 2024. https://doi.org/10.3133/mcs2024.

[39] D. Gao, F.-P. Wang, Y.-T. Wang, Y.-N. Zeng, Sustainable Utilization of Steel Slag from Traditional Industry and Agriculture to Catalysis, Sustainability 12 (2020) 9295. https://doi.org/10.3390/su12219295.

[40] Z. Chen, Z. Cang, F. Yang, J. Zhang, L. Zhang, Carbonation of steelmaking slag presents an opportunity for carbon neutral: A review, Journal of CO2 Utilization 54 (2021) 101738. https://doi.org/10.1016/j.jcou.2021.101738.

[41] X. Huang, J. Zhang, L. Zhang, Accelerated carbonation of steel slag: A review of methods, mechanisms and influencing factors, Constr. Build. Mater. 411 (2024) 134603. https://doi.org/10.1016/j.conbuildmat.2023.134603.

[42] A. Said, H.-P. Mattila, M. Järvinen, R. Zevenhoven, Production of precipitated calcium carbonate (PCC) from steelmaking slag for fixation of CO2, Appl. Energy 112 (2013) 765–771. https://doi.org/10.1016/j.apenergy.2012.12.042.

[43] X. Zhang, J. Zhao, Y. Liu, J. Li, Use of steel slag as carbonation material: A review of carbonation methods and evaluation, environmental factors and carbon conversion process, Journal of CO2 Utilization 88 (2024) 102947. https://doi.org/10.1016/j.jcou.2024.102947.

[44] Y. Li, H. Pan, Z. Li, Unravelling the dissolution dynamics of silicate minerals by deep learning molecular dynamics simulation: A case of dicalcium silicate, Cem. Concr. Res. 165 (2023) 107092. https://doi.org/10.1016/j.cemconres.2023.107092.

[45] Q. Zhao, X. Chu, X. Mei, Q. Meng, J. Li, C. Liu, H. Saxén, R. Zevenhoven, Co-treatment of Waste From Steelmaking Processes: Steel Slag-Based Carbon Capture and Storage by Mineralization, Front. Chem. 8 (2020). https://doi.org/10.3389/fchem.2020.571504.

[46] Y. Luo, D. He, Research status and future challenge for CO2 sequestration by mineral carbonation strategy using iron and steel slag, Environmental Science and Pollution Research 28 (2021) 49383–49409. https://doi.org/10.1007/s11356-021-15254-x.

[47] M. Eugenia Eugenio, D. Ibarra, R. Martín-Sampedro, E. Espinosa, I. Bascón, A. Rodríguez, Alternative Raw Materials for Pulp and Paper Production in the Concept of a Lignocellulosic Biorefinery, in: Cellulose, IntechOpen, 2019. https://doi.org/10.5772/intechopen.90041.

[48] P. Bajpai, Pulping Fundamentals, in: Biermann's Handbook of Pulp and Paper, Elsevier, 2018: pp. 295–351.

[49] T. Kinnarinen, M. Golmaei, E. Jernström, A. Häkkinen, Separation, treatment and utilization of inorganic residues of chemical pulp mills, J. Clean. Prod. 133 (2016) 953–964. https://doi.org/10.1016/j.jclepro.2016.06.024.

[50] H. Kumar, R. Alén, Recovery of aliphatic low-molecular-mass carboxylic acids from hardwood kraft black liquor, Sep. Purif. Technol. 142 (2015) 293–298. https://doi.org/10.1016/j.seppur.2014.12.038.

[51] P. Tomani, The Lignoboost Process, 2010.

[52] J. Cramstedt, Carbon capture using white liquor in a Kraft pulping plant. Simulation and evaluation of a scrubber, Chalmers University of Technology, 2023. http://hdl.handle.net/20.500.12380/306471 (accessed February 24, 2026).

[53] L. Cid Gomes, A. da Rosa Garcia, F. Raeisi, L.C. de Oliveira Barbosa, D. Wasalabandara, A. Panakkal Manuel, N.L. Skovborg, E.T. Hostrup, J. Wojtasz, M. Gunnarsson, M. Ambye-Jensen, D. Bernin, Green Biorefinery Side Stream as a Source of Chlorophyll Pigments, Lignin, and Cellulose for Textile Fibers, ACS Sustain. Chem. Eng. 13 (2025) 16946–16957. https://doi.org/10.1021/acssuschemeng.5c06653.

[54] J. Wojtasz, N. Sjöstedt, B. Storm, M.M. Parayil, A. Ulefors, L. Nilsson, M.A. Hernández Leal, A. Michud, Å. Östlund, T. Rydberg, D. Bernin, Producing dissolving pulp from agricultural waste, RSC Sustainability 3 (2025) 2210–2220. https://doi.org/10.1039/D4SU00534A.

[55] A. Muñoz-Castillo, P.J. Sánchez-Soto, D. Eliche-Quesada, Valorisation of rice husk ash as an activator in the preparation of alkali-activated cements based on electric arc furnace slag, Archives of Civil and Mechanical Engineering 25 (2025) 155. https://doi.org/10.1007/s43452-025-01209-3.

[56] R.R. Zaky, M.M. Hessien, A.A. El-Midany, M.H. Khedr, E.A. Abdel-Aal, K.A. El-Barawy, Preparation of silica nanoparticles from semi-burned rice straw ash, Powder Technol. 185 (2008) 31–35. https://doi.org/10.1016/j.powtec.2007.09.012.

[57] N.H. Do, H.H. Pham, T.M. Le, J. Lauwaert, L. Diels, A. Verberckmoes, N.H.N. Do, V.T. Tran, P.K. Le, The novel method to reduce the silica content in lignin recovered from black liquor originating from rice straw, Sci. Rep. 10 (2020) 21263. https://doi.org/10.1038/s41598-020-77867-5.

[58] R. Pérez-López, G. Montes-Hernandez, J.M. Nieto, F. Renard, L. Charlet, Carbonation of alkaline paper mill waste to reduce CO2 greenhouse gas emissions into the atmosphere, Applied Geochemistry 23 (2008) 2292–2300. https://doi.org/10.1016/j.apgeochem.2008.04.016.

[59] A.C. Spínola, C.T. Pinheiro, A.G.M. Ferreira, L.M. Gando-Ferreira, Mineral carbonation of a pulp and paper industry waste for CO2 sequestration, Process Safety and Environmental Protection 148 (2021) 968–979. https://doi.org/10.1016/j.psep.2021.02.019.

[60] R. Sun, Y. Li, C. Liu, X. Xie, C. Lu, Utilization of lime mud from paper mill as CO2 sorbent in calcium looping process, Chemical Engineering Journal 221 (2013) 124–132. https://doi.org/10.1016/j.cej.2013.01.068.

[61] Y. Li, R. Sun, Studies on adsorption of carbon dioxide on alkaline paper mill waste using cyclic process, Energy Convers. Manag. 82 (2014) 46–53. https://doi.org/10.1016/j.enconman.2014.03.004.

[62] R. Pérez-López, J. Castillo, D. Quispe, J.M. Nieto, Neutralization of acid mine drainage using the final product from CO2 emissions capture with alkaline paper mill waste, J. Hazard. Mater. 177 (2010) 762–772. https://doi.org/10.1016/j.jhazmat.2009.12.097.

[63] D. Ragnvaldsson, M. Bergknut, J. Lewis, S. Drotz, A. Lundkvist, K. Abrahamsson, S. Fernerud, A novel method for reducing acid mine drainage using green liquor dregs, Environ. Chem. Lett. 12 (2014) 443–447. https://doi.org/10.1007/s10311-014-0469-z.

[64] R.M. Novais, J. Carvalheiras, L. Senff, J.A. Labrincha, Upcycling unexplored dregs and biomass fly ash from the paper and pulp industry in the production of eco-friendly geopolymer mortars: A preliminary assessment, Constr. Build. Mater. 184 (2018) 464–472. https://doi.org/10.1016/j.conbuildmat.2018.07.017.

[65] R.V. Silva, J. de Brito, R.K. Dhir, Properties and composition of recycled aggregates from construction and demolition waste suitable for concrete production, Constr. Build. Mater. 65 (2014) 201–217. https://doi.org/10.1016/j.conbuildmat.2014.04.117.

[66] R. Infante Gomes, D. Bastos, C. Brazão Farinha, R. Veiga, J. de Brito, P. Faria, A. Santos Silva, A. Bogas, Carbonation potential of recycled aggregates from construction and demolition waste Lab-Sustainable Construction Materials Association, Linda-a-Velha, Portugal 2 c 5 Lab-Sustainable Construction Materials Association, Linda-a-Velha, Portugal 3 c 5 Lab-Sustainable Construction Materials Association, Linda-a, in: n.d.

[67] D. Xuan, B. Zhan, C.S. Poon, Durability of recycled aggregate concrete prepared with carbonated recycled concrete aggregates, Cem. Concr. Compos. 84 (2017) 214–221. https://doi.org/10.1016/j.cemconcomp.2017.09.015.

[68] D. Xuan, B. Zhan, C.S. Poon, Assessment of mechanical properties of concrete incorporating carbonated recycled concrete aggregates, Cem. Concr. Compos. 65 (2016) 67–74. https://doi.org/10.1016/j.cemconcomp.2015.10.018.

[69] C.S. Poon, P. Shen, Y. Jiang, Z. Ma, D. Xuan, Total recycling of concrete waste using accelerated carbonation: A review, Cem. Concr. Res. 173 (2023) 107284. https://doi.org/10.1016/j.cemconres.2023.107284.

[70] L. Li, M. Wu, An overview of utilizing CO2 for accelerated carbonation treatment in the concrete industry, Journal of CO2 Utilization 60 (2022) 102000. https://doi.org/10.1016/j.jcou.2022.102000.

[71] G.A. Miller, S. Azad, Influence of soil type on stabilization with cement kiln dust, Constr. Build. Mater. 14 (2000) 89–97. https://doi.org/10.1016/S0950-0618(00)00007-6.

[72] E. Benhelal, G. Zahedi, E. Shamsaei, A. Bahadori, Global strategies and potentials to curb CO2 emissions in cement industry, J. Clean. Prod. 51 (2013) 142–161. https://doi.org/10.1016/j.jclepro.2012.10.049.

[73] S. Wu, Z. Shao, R.M. Andrew, L. Bing, J. Wang, L. Niu, Z. Liu, F. Xi, Global CO2 uptake by cement materials accounts 1930–2023, Sci. Data 11 (2024) 1409. https://doi.org/10.1038/s41597-024-04234-8.

[74] H. Stripple, C. Ljungkrantz, T. Gustafsson, Andersson Ronny, CO2 uptake in cement containing products, Stockholm, 2018.

[75] S.K. Adekunle, Carbon sequestration potential of cement kiln dust: Mechanisms, methodologies, and applications, J. Clean. Prod. 446 (2024) 141283. https://doi.org/10.1016/j.jclepro.2024.141283.

[76] J. Pedraza, A. Zimmermann, J. Tobon, R. Schomäcker, N. Rojas, On the road to net zero-emission cement: Integrated assessment of mineral carbonation of cement kiln dust, Chemical Engineering Journal 408 (2021) 127346. https://doi.org/10.1016/j.cej.2020.127346.

[77] D.N. Huntzinger, J.S. Gierke, S.K. Kawatra, T.C. Eisele, L.L. Sutter, Carbon Dioxide Sequestration in Cement Kiln Dust through Mineral Carbonation, Environ. Sci. Technol. 43 (2009) 1986–1992. https://doi.org/10.1021/es802910z.

[78] M.H. Youn, K.T. Park, Y.H. Lee, S.-P. Kang, S.M. Lee, S.S. Kim, Y.E. Kim, Y.N. Ko, S.K. Jeong, W. Lee, Carbon dioxide sequestration process for the cement industry, Journal of CO2 Utilization 34 (2019) 325–334. https://doi.org/10.1016/j.jcou.2019.07.023.

[79] K.A. Clavier, J.M. Paris, C.C. Ferraro, T.G. Townsend, Opportunities and challenges associated with using municipal waste incineration ash as a raw ingredient in cement production – a review, Resour. Conserv. Recycl. 160 (2020) 104888. https://doi.org/10.1016/j.resconrec.2020.104888.

[80] M. Šyc, F.G. Simon, J. Hykš, R. Braga, L. Biganzoli, G. Costa, V. Funari, M. Grosso, Metal recovery from incineration bottom ash: State-of-the-art and recent developments, J. Hazard. Mater. 393 (2020) 122433. https://doi.org/10.1016/j.jhazmat.2020.122433.

[81] Y. Zhang, L. Wang, L. Chen, B. Ma, Y. Zhang, W. Ni, D.C.W. Tsang, Treatment of municipal solid waste incineration fly ash: State-of-the-art technologies and future perspectives, J. Hazard. Mater. 411 (2021) 125132. https://doi.org/10.1016/j.jhazmat.2021.125132.

[82] J. Chen, Z. Chen, X. Lin, X. Li, J. Yan, A systematic review of accelerated carbonation technology for municipal solid waste incineration fly ash: Carbon sequestration, reuse and heavy metal risk assessment, Chemical Engineering Journal 508 (2025) 160926. https://doi.org/10.1016/j.cej.2025.160926.

[83] R.J. Yeo, A. Sng, C. Wang, L. Tao, Q. Zhu, J. Bu, Strategies for heavy metals immobilization in municipal solid waste incineration bottom ash: a critical review, Rev. Environ. Sci. Biotechnol. 23 (2024) 503–568. https://doi.org/10.1007/s11157-024-09694-3.

[84] N. Um, J.-W. Ahn, Effects of two different accelerated carbonation processes on MSWI bottom ash, Process Safety and Environmental Protection 111 (2017) 560–568. https://doi.org/10.1016/j.psep.2017.08.028.

[85] Kh.A. Suerbaev, E.G. Chepaikin, F.M. Kanapieva, G.Zh. Seitenova, Carboxylation of organic compounds with metal alkyl carbonates (review), Petroleum Chemistry 49 (2009) 265–273. https://doi.org/10.1134/S096554410904001X.

[86] I. Hirao, T. Kito, T. Funamoto, T. Murakami, K. Usami, Carboxylation of Phenol Derivatives. XXII. Formation of Alkali Alkyl Carbonate by the *O* -Carboxylation of Alcohol in the Presence of an Alkali Salt of a Weak Acid, Bull. Chem. Soc. Jpn. 49 (1976) 2775–2779. https://doi.org/10.1246/bcsj.49.2775.

[87] E.-J. Kim, S.-J. Han, J.-H. Wee, Carbon Dioxide Capture and Carbonate Synthesis via Carbonation of KOH-Dissolved Alcohol Solution, Journal of Korean Society of Environmental Engineers 37 (2015) 597–606. https://doi.org/10.4491/KSEE.2015.37.11.597.

[88] S.-J. Han, J.-H. Wee, Carbon Dioxide Fixation via the Synthesis of Sodium Ethyl Carbonate in NaOH-Dissolved Ethanol, Ind. Eng. Chem. Res. 55 (2016) 12111–12118. https://doi.org/10.1021/acs.iecr.6b03250.

[89] S.-J. Han, J.-H. Wee, Carbon Dioxide Fixation by Combined Method of Physical Absorption and Carbonation in NaOH-Dissolved Methanol, Energy & Fuels 31 (2017) 1747–1755. https://doi.org/10.1021/acs.energyfuels.6b02709.

[90] S.-J. Mun, S.-J. Han, J.-H. Wee, Carbon Dioxide Fixation by Precipitating $NaHCO_3$ via Carbonation of NaOH-Dissolved Ethanol Aqueous Solution, Energy & Fuels 32 (2018) 8614–8622. https://doi.org/10.1021/acs.energyfuels.8b01584.

[91] S. Han, D. Han, J. Wee, Re-carbonation by recycling NaOH-dissolved ethanol solution for carbon dioxide fixation, Environ. Prog. Sustain. Energy 39 (2020). https://doi.org/10.1002/ep.13300.

[92] J. Pak, S.-J. Han, J.-H. Wee, Precipitation of potassium-based carbonates for carbon dioxide fixation via the carbonation and re-carbonation of KOH dissolved aqueous ethanol solutions, Chemical Engineering Journal 427 (2022) 131669. https://doi.org/10.1016/j.cej.2021.131669.

[93] R. Sen, A. Goeppert, S. Kar, G.K.S. Prakash, Hydroxide Based Integrated CO_2 Capture from Air and Conversion to Methanol, J. Am. Chem. Soc. 142 (2020) 4544–4549. https://doi.org/10.1021/jacs.9b12711.

[94] P.C. De Carvalho Pinto, T. V. Batista, G. De Rezende Ferreira, G.P. Voga, L.C.A. Oliveira, H.S. Oliveira, L.A. De Souza, J.C. Belchior, Chemical Absorption of CO_2 Enhanced by Solutions of Alkali Hydroxides and Alkoxides at Room Temperature, ChemistrySelect 7 (2022). https://doi.org/10.1002/slct.202202731.

[95] G. Besagni, F. Inzoli, T. Ziegenhein, Two-Phase Bubble Columns: A Comprehensive Review, ChemEngineering 2 (2018) 13. https://doi.org/10.3390/chemengineering2020013.

[96] O. Rojas, J.-L. Salager, Surface activity of bagasse lignin derivatives found in spent-of soda pulping plants, (1994).

[97] D. Hala, A.-E. Sohair, Treatment of black liquor derived from non-woody feedstocks, Advances in Ecological Sciences (2003) 453–462.

[98] F.M. Baena-Moreno, E. Leventaki, P.H. Ho, A.R. Tajik, D. Brzic, G. Sardina, H. Ström, D. Bernin, Potential of organic carbonates production for efficient carbon dioxide capture, transport and storage: Reaction performance with sodium hydroxide–ethanol mixtures, Heliyon 9 (2023) e14140. https://doi.org/10.1016/j.heliyon.2023.e14140.

[99] A.A. Kulkarni, J.B. Joshi, Bubble Formation and Bubble Rise Velocity in Gas–Liquid Systems: A Review, Ind. Eng. Chem. Res. 44 (2005) 5873–5931. https://doi.org/10.1021/ie049131p.

[100] A.B. Tayler, Experimental characterisation of bubbly flow using MRI, University of Cambridge, 2011.

[101] The Engineering ToolBox (2018). Carbon dioxide - Density and Specific Weight vs. Temperature and Pressure, (n.d.). https://www.engineeringtoolbox.com/carbon-dioxide-density-specific-weight-temperature-pressure-d_2018.html (accessed February 24, 2026).

[102] J. Behin, M. Zeyghami, Dissolving pulp from corn stalk residue and waste water of Merox unit, Chemical Engineering Journal 152 (2009) 26–35. https://doi.org/10.1016/j.cej.2009.03.024.

[103] C. Heitner, D. Dimmel, J. Schmidt, Lignin and lignans: advances in chemistry, CRC Press, 2016.

[104] Y. Xia, S. Moran, E.P. Nikonowicz, X. Gao, Z-restored spin-echo ^{13}C 1D spectrum of straight baseline free of hump, dip and roll, Magnetic Resonance in Chemistry 46 (2008) 432–435. https://doi.org/10.1002/mrc.2195.

[105] A. Altomare, N. Corriero, C. Cuocci, A. Falcicchio, A. Moliterni, R. Rizzi, *QUALX2.0*: a qualitative phase analysis software using the freely available database POW_COD, J. Appl. Crystallogr. 48 (2015) 598–603. https://doi.org/10.1107/S1600576715002319.

[106] P. Paufler, R. A. Young (ed.). The Rietveld Method. International Union of Crystallography. Oxford University Press 1993. 298 p. Price £ 45.00. ISBN 0–19–855577–6, Crystal Research and Technology 30 (1995) 494–494. https://doi.org/10.1002/crat.2170300412.

[107] TOPAS-R, Version 4.2, General profile and Structure Analysis Software For Powder Diffraction Data, (2009).

[108] F. Milella, M. Mazzotti, Estimating speciation of aqueous ammonia solutions of ammonium bicarbonate: application of least squares methods to infrared spectra, React. Chem. Eng. 4 (2019) 1284–1302. https://doi.org/10.1039/C9RE00137A.

[109] B. Rijo, E. Fernando, M. Ramos, A.P.S. Dias, Biodiesel production over sodium carbonate and bicarbonate catalysts, Fuel 323 (2022) 124383. https://doi.org/10.1016/j.fuel.2022.124383.

[110] L. Rincón, C. Ruiz, R.R. Contreras, J. Almarza, Study of the NaOH(s)–CO_2 (g) reaction creating value for industry: green natrite production, energy, and its potential in different sustainable scenarios, Environmental Science: Advances 2 (2023) 957–966. https://doi.org/10.1039/D2VA00281G.

[111] M. Thommes, K. Kaneko, A. V. Neimark, J.P. Olivier, F. Rodriguez-Reinoso, J. Rouquerol, K.S.W. Sing, Physisorption of gases, with special reference to the evaluation of surface area and pore size distribution (IUPAC Technical Report), Pure and Applied Chemistry 87 (2015) 1051–1069. https://doi.org/10.1515/pac-2014-1117.

[112] S.-Y. Pan, T.-C. Ling, A.-H.A. Park, P.-C. Chiang, An Overview: Reaction Mechanisms and Modelling of CO2 Utilization via Mineralization, Aerosol Air Qual. Res. 18 (2018) 829–848. https://doi.org/10.4209/aaqr.2018.03.0093.

[113] S.N. Lekakh, C.H. Rawlins, D.G.C. Robertson, V.L. Richards, K.D. Peaslee, Kinetics of Aqueous Leaching and Carbonization of Steelmaking Slag, Metallurgical and Materials Transactions B 39 (2008) 125–134. https://doi.org/10.1007/s11663-007-9112-8.

[114] M. Tu, H. Zhao, Z. Lei, L. Wang, D. Chen, H. Yu, T. Qi, Aqueous Carbonation of Steel Slag: A Kinetics Study, ISIJ International 55 (2015) 2509–2514. https://doi.org/10.2355/isijinternational.ISIJINT-2015-142.

[115] E. Miao, X. Zheng, Z. Xiong, Y. Zhao, J. Zhang, Kinetic modeling of direct aqueous mineral carbonation using carbide slag in a stirred tank reactor, Fuel 315 (2022) 122837. https://doi.org/10.1016/j.fuel.2021.122837.

[116] F. Zhu, L. Cui, Y. Liu, L. Zou, J. Hou, C. Li, G. Wu, R. Xu, B. Jiang, Z. Wang, Experimental Investigation and Mechanism Analysis of Direct Aqueous Mineral Carbonation Using Steel Slag, Sustainability 16 (2023) 81. https://doi.org/10.3390/su16010081.

[117] S.-Y. Pan, T.-C. Chung, C.-C. Ho, C.-J. Hou, Y.-H. Chen, P.-C. Chiang, CO2 Mineralization and Utilization using Steel Slag for Establishing a Waste-to-Resource Supply Chain, Sci. Rep. 7 (2017) 17227. https://doi.org/10.1038/s41598-017-17648-9.

[118] F. Bonfante, G. Ferrara, P. Humbert, D. Garufi, J.-M. Tulliani, P. Palmero, Direct aqueous carbonation of electric arc furnace slag: process optimisation through experimental design, Mater. Struct. 58 (2025) 127. https://doi.org/10.1617/s11527-025-02661-6.

[119] O. Bereziuk, K. Gubina, V. Trush, V. Ovchynnikov, Crystal structure of the sodium salt of mesotrione: a triketone herbicide, Acta Crystallogr. E Crystallogr. Commun. 80 (2024) 296–299. https://doi.org/10.1107/S2056989024001439.

[120] J. Jiang, Q. Li, P. Yan, S. Xu, Y. Zhou, D. Zheng, Polymorph design of CaCO3 from stable calcite to metastable vaterite and amorphous CaCO3 via altering reaction system step by step, Advanced Powder Technology 36 (2025) 104758. https://doi.org/10.1016/j.apt.2024.104758.

[121] N. Negishi, T. Inaba, Y. Miyazaki, G. Ishii, Y. Yang, S. Koura, Aqueous mechano-bactericidal action of acicular aragonite crystals, Sci. Rep. 11 (2021) 19218. https://doi.org/10.1038/s41598-021-98797-w.

[122] M. Boon, W.D.A. Rickard, A.L. Rohl, F. Jones, Stabilization of Aragonite: Role of Mg^{2+} and Other Impurity Ions, Cryst. Growth Des. 20 (2020) 5006–5017. https://doi.org/10.1021/acs.cgd.0c00152.

[123] R.A. Boulos, F. Zhang, E.S. Tjandra, A.D. Martin, D. Spagnoli, C.L. Raston, Spinning up the polymorphs of calcium carbonate, Sci. Rep. 4 (2014) 3616. https://doi.org/10.1038/srep03616.

[124] A.W. Knight, J.A. Harvey, M. Shohel, P. Lu, D. Cummings, A.G. Ilgen, The combined effects of Mg2+ and Sr2+ incorporation during CaCO3 precipitation and crystal growth, Geochim. Cosmochim. Acta 345 (2023) 16–33. https://doi.org/10.1016/j.gca.2023.01.021.

[125] X. Xu, H. Guo, X. Cheng, M. Li, The promotion of magnesium ions on aragonite precipitation in MICP process, Constr. Build. Mater. 263 (2020) 120057. https://doi.org/10.1016/j.conbuildmat.2020.120057.

[126] C. Unluer, A. Al-Tabbaa, GREEN CONSTRUCTION WITH CARBONATING REACTIVE MAGNESIA POROUS BLOCKS: EFFECT OF CEMENT AND WATER CONTENTS, n.d.

[127] S. Teir, S. Eloneva, C.-J. Fogelholm, R. Zevenhoven, Fixation of carbon dioxide by producing hydromagnesite from serpentinite, Appl. Energy 86 (2009) 214–218. https://doi.org/10.1016/j.apenergy.2008.03.013.

[128] S.S. Ugapeva, O.B. Oleinikov, N. V. Zayakina, Rare Hydrated Magnesium Carbonate Minerals Nesquehonite and Dypingite of the Obnazhennaya Kimberlite Pipe, in the Yakutian Kimberlite Province, Minerals 13 (2023) 1363. https://doi.org/10.3390/min13111363.

[129] O. Kotova, New adsorbent materials on the base of minerals and industrial waste, IOP Conf. Ser. Mater. Sci. Eng. 613 (2019) 012001. https://doi.org/10.1088/1757-899X/613/1/012001.

[130] G. Gundiah, M. Eswaramoorthy, S. Neeraj, S. Natarajan, C.N.R. Rao, Synthesis and characterization of submicron-sized mesoporous aluminosilicate spheres, Journal of Chemical Sciences 113 (2001) 227–234. https://doi.org/10.1007/BF02704072.

[131] D. ĐORĐEVIĆ, M. STANKOVIĆ, N. KRSTIĆ, V. DIMITRIJEVIĆ, N. ANASTASIJEVIĆ, M. ĐORĐEVI Ć, M. NIKOLIĆ, GEOCHEMICAL ANALYSIS OF KOSTOLAC POWER PLANT FLY ASH: WORKING AND LIVING ENVIRONMENT INFLUENCE ASPECT, Safety Engineering 8 (2018) 15–20. https://doi.org/10.7562/SE2018.8.01.03.

[132] A.R. Tajik, E. Leventaki, F. Baena-Moreno, C. Kugge, D. Bernin, H. Ström, G. Sardina, The influence of the impeller on carbonation performances in carbon capture using industrial by-products, International Journal of Thermofluids 29 (2025) 101385. https://doi.org/10.1016/j.ijft.2025.101385.

[133] R. Wethman, J. Derosa, V.T. Tran, T. Kang, O. Apolinar, A. Abraham, R. Kleinmans, S.R. Wisniewski, J.R. Coombs, K.M. Engle, An Under-Appreciated Source of Reproducibility Issues in Cross-Coupling: Solid-State Decomposition of Primary Sodium Alkoxides in Air, ACS Catal. 11 (2021) 502–508. https://doi.org/10.1021/acscatal.0c04124.

[134] H. Tu, H. Liu, L. Xu, Z. Luo, L. Li, Y. Tian, W. Deng, G. Zou, H. Hou, X. Ji, Carbon dots from alcohol molecules: principles and the reaction mechanism, Chem. Sci. 14 (2023) 12194–12204. https://doi.org/10.1039/D3SC04606K.

[135] J. McMurry, Organic Chemistry: A Tenth Edition, in: OpenStax, Houston, Texas, 2023. https://openstax.org/books/organic-chemistry/pages/23-summary (accessed May 9, 2025).

[136] L. Li, Y. Li, Y. Ye, R. Guo, A. Wang, G. Zou, H. Hou, X. Ji, Kilogram-Scale Synthesis and Functionalization of Carbon Dots for Superior Electrochemical Potassium Storage, ACS Nano 15 (2021) 6872–6885. https://doi.org/10.1021/acsnano.0c10624.

[137] Z.-F. Yuan, W.-N. Zhao, Z.-P. Liu, B.-Q. Xu, NaOH alone can be a homogeneous catalyst for selective aerobic oxidation of alcohols in water, J. Catal. 353 (2017) 37–43. https://doi.org/10.1016/j.jcat.2017.05.006.

[138] R. Wethman, J. Derosa, V.T. Tran, T. Kang, O. Apolinar, A. Abraham, R. Kleinmans, S.R. Wisniewski, J.R. Coombs, K.M. Engle, An Under-Appreciated Source of Reproducibility Issues in Cross-Coupling: Solid-State Decomposition of Primary Sodium Alkoxides in Air, ACS Catal. 11 (2021) 502–508. https://doi.org/10.1021/acscatal.0c04124.

[139] S. Veerasingam, R. Venkatachalapathy, Estimation of carbonate concentration and characterization of marine sediments by Fourier Transform Infrared Spectroscopy, Infrared Phys. Technol. 66 (2014) 136–140. https://doi.org/10.1016/j.infrared.2014.06.005.

[140] S.K.A. Mudalip, Mohd.R.A. Bakar, F. Adam, P. Jamal, Structures and Hydrogen Bonding Recognition of Mefenamic Acid Form I Crystals in Mefenamic Acid/ Ethanol Solution, International Journal of Chemical Engineering and Applications (2013) 124–128. https://doi.org/10.7763/IJCEA.2013.V4.277.

[141] A.B.D. Nandiyanto, R. Oktiani, R. Ragadhita, How to read and interpret ftir spectroscope of organic material, Indonesian Journal of Science and Technology 4 (2019) 97–118. https://doi.org/10.17509/ijost.v4i1.15806.

[142] National Institute of Standards and Technology, Formic acid, sodium salt, (2018). https://webbook.nist.gov/cgi/cbook.cgi?ID=B6010183&Mask=80 (accessed May 8, 2025).

[143] D. Lin-Vien, N.B. Colthup, W.G. Fateley, J.G. Grasselli, A Summary of Characteristic Raman and Infrared Frequencies, in: The Handbook of Infrared and Raman Characteristic Frequencies of Organic Molecules, Elsevier, 1991: pp. 477–490. https://doi.org/10.1016/B978-0-08-057116-4.50027-4.

[144] A.K. Khan, Facile Synthesis, Characterization of New Quinazolinones with Different Azo Compounds, 1,2,3-Triazole Moieties and Evaluation Their Anti-bacterial Activity., Al-Mustansiriyah Journal of Science 28 (2018) 122–133. https://doi.org/10.23851/mjs.v28i3.180.

[145] M. Daryanavard, D. Armstrong, A.J. Lough, U. Fekl, The first palladium(<scp>iv</scp>) aryldiazenido complex: relevance for C–C coupling, Dalton Transactions 46 (2017) 4004–4008. https://doi.org/10.1039/C7DT00078B.

[146] A. Bhatia, S. Chopra, K. Nagpal, P.K. Deb, M. Tekade, R.K. Tekade, Polymorphism and its Implications in Pharmaceutical Product Development, in: Dosage Form Design Parameters, Elsevier, 2018: pp. 31–65. https://doi.org/10.1016/B978-0-12-814421-3.00002-6.

[147] G. Shavalieva, H. Olivegren, H. Baumann, E. Leventaki, E. Couto Queiroz, D. Bernin, Green liquor dregs for carbon capture, utilization, and storage: initial LCA and economic analysis, Nord. Pulp Paper Res. J. 41 (2026) 201–214. https://doi.org/10.1515/npprj-2024-0013.

[148] P.C. De Carvalho Pinto, T. V. Batista, G. De Rezende Ferreira, G.P. Voga, L.C.A. Oliveira, H.S. Oliveira, L.A. De Souza, J.C. Belchior, Chemical Absorption of CO_2 Enhanced by Solutions of Alkali Hydroxides and Alkoxides at Room Temperature, ChemistrySelect 7 (2022). https://doi.org/10.1002/slct.202202731.

[149] M. Mahmoudkhani, D.W. Keith, Low-energy sodium hydroxide recovery for CO2 capture from atmospheric air—Thermodynamic analysis, International Journal of Greenhouse Gas Control 3 (2009) 376–384. https://doi.org/10.1016/j.ijggc.2009.02.003.